NOTE TO USERS

PROPERTIES OF MAGNETIC TRANSITION METAL-BROMIDE GRAPHITE INTERCALATION COMPOUNDS

By

PAUL A. DUBE, B.Sc.

A Thesis

Submitted to the School of Graduate Studies

in Partial Fulfillment of the Requirements

for the Degree

Doctor of Philosophy.

McMaster University

PROPERTIES OF MAGNETIC TRANSITION METAL-BROMIDE GICs

DOCTOR OF PHILOSOPHY (2002)
(Physics)

McMaster University
Hamilton, Ontario

TITLE: Properties of Magnetic Transition Metal-Bromide Graphite Intercalation Compounds

AUTHOR: Paul A. Dube, B.Sc. (University of Waterloo)

SUPERVISOR: Dr. W.R. Datars

NUMBER OF PAGES: ix, 163

Abstract

The graphite intercalation compounds (GICs) of $CoBr_2$, $FeBr_2$ and $NiBr_2$ have been prepared by intercalation into highly oriented pyrolytic graphite (HOPG). Stages 1 and 2 $CoBr_2$-GIC, stage-2 $FeBr_2$-GIC and stages 2, 3 and 5 $NiBr_2$-GIC have been studied by measuring the dc magnetization, ac susceptibility and heat capacity. A single-crystal sample of stage-3 $CoBr_2$-GIC was studied using neutron diffraction. The $CoBr_2$-GICs do not order at any observed temperature (down to 2 K for stages 1 and 2, 5.5K for stage-3). Stage-2 $FeBr_2$-GIC orders in three stages on cooling, with a transition from a paramagnetic phase to a phase with short-range two-dimensional ordering at 14.5 K, another to a phase with longer-range ordering within individual intercalant domains at 8.5 K and a third to a cluster-glass phase at 3 K. From dc magnetization measurements, stages 2, and 3 $NiBr_2$-GIC order two-dimensionally at 6 K and 7 K, respectively. Stage-5 $NiBr_2$-GIC is superparamagnetic below 5 K. The Curie-Weiss law, modified to include a temperature-independent Van Vleck paramagnetism, is fit to the high-temperature dc susceptibility data. The need to include the temperature-independent term is also shown in magnetization curves. Simulations using Green's function calculations show that the absence of three-dimensional ordering down to 2 K in the $CoBr_2$ and $NiBr_2$ compounds is reasonable, but somewhat unexpected.

Acknowledgements

I would like to express my gratitude to my supervisor, Dr. W.R. Datars, for his guidance throughout this project. I would also like to thank Dr. Pash Ummat for sharing his knowledge in sample preparation. Many thanks to Dr. Graeme Luke for the use of his equipment and to Gord Hewittson for his assistance in helium transfers and equipment failures.

I thank Mike, Zac, Jeff and all the other grad students roaming the halls for the many useful (and some less useful) discussions on life, the universe and everything.

Most importantly, I would like to thank my wife, Kim. You are everything to me and I would not have been able to do this without your help. Thank you for standing by me and putting up with me for the last five years.

This work was supported by the Natural Sciences and Engineering Research Council of Canada and by the Government of Ontario and McMaster University.

Contents

List of Figures

List of Tables

Chapter 1
Introduction

The first report of intercalation into graphite was by Schaffäutl in 1841. Systematic studies of intercalation compounds began in the 1930's with the advent of x-ray diffraction techniques allowing for the determination of structural properties. To date, there are hundreds of chemical species that have been intercalated into graphite.

The interest in graphite intercalation compounds (GICs) is associated with several different properties. Electrical studies have shown that the conductivity of the compounds ranges from nearly insulating to superconducting. Structural studies are used to determine lattice parameters and structural phase transitions such as commensurate-incommensurate phase transitions. Magnetic studies, such as this one, focus on determining magnetic properties of reduced-dimensional magnetism.

There are several practical applications that have been considered for various GICs. They have been used as catalysts for chemical reactions including organic reactions and polymerization reactions. Several metal halide GICs have been studied for their potential use as the cathode material in lithium rechargeable batteries. Their high energy storage and low relative mass make them attractive candidates for this

purpose. Intercalated graphite fibres produce strong, flexible, highly conductive wires.

Many metal chloride-GICs have been prepared and studied extensively. In pristine form, the dichlorides of iron, nickel and cobalt are layered, with nearly two-dimensional magnetic characteristics. When intercalated into graphite, the effective dimensionality is lowered and several interesting phenomena exist.

This is the first time that the magnetic properties of the graphite intercalation compounds of the dibromides of cobalt, iron and nickel have been studied. Previous attempts to intercalate the materials achieved varying degrees of success, but no one has intercalated the dibromides into highly oriented pyrolytic graphite. These materials have now been intercalated with the aim of determining the location and nature of magnetic phase transitions and to determine the ordering present. To this end, several experimental techniques have been employed, including dc magnetization, ac susceptibility and specific heat measurements.

The samples studied include stages 1 and 2 $CoBr_2$-GIC, stage-2 $FeBr_2$-GIC and stages 2, 3 and 5 $NiBr_2$-GIC. A single-crystal sample of stage-3 $CoBr_2$-GIC was also studied using neutron diffraction.

1.1 Magnetism

A brief introduction to the concepts of magnetism necessary to enjoy this thesis is given presently. It is by no means intended to be a comprehensive description of the field. The equations presented here are derived from molecular field theory, which is exact only in dimensions greater than three. Hence, these relations are used as useful approximations and for comparative purposes.

There are three basic types of magnetic ordering; paramagnetism, ferromagnetism and antiferromagnetism. A paramagnetic substance is one in which the magnetic moments have no tendency to align with each other. In the absence of an external applied magnetic field, the net magnetization of a paramagnetic substance is zero. When a field is applied, the magnetic moments in the material tend to align with the field, creating a finite magnetization. If the field is then turned off, the moments go back to a random orientation with zero magnetization.

A ferromagnetic substance is one whose magnetic moments have a tendency to align parallel to each other. At finite temperatures, the thermal energy of the system keeps the moments from aligning all in one direction, but rather the moments tend to create smaller domains in which many moments are aligned parallel. Neighbouring domains, however, do not necessarily align perfectly, but do have a preferred orientation. In zero field, then, the ferromagnetic substance can have finite magnetization. If a field is applied, the moments tend to align along the field and the magnetization

increases. If the field is then removed, a finite magnetization, called the remanence, remains.

1.1.1 Antiferromagnetism

In an antiferromagnetic substance[1, 2], neighbouring magnetic moments have a tendency to align antiparallel. In this state, in zero applied field, the net magnetization is zero. When a field is applied, however, there is a tendency for the moments to align along the field direction. This creates a competition between the tendency to align parallel to the field and antiparallel to each other. Some substances enter a 'spin-flop' phase, in which the moments align at a different angle with respect to each other and at an angle to the field in order to minimize the energy of the system. The energy of a moment is decreased by aligning with the field but opposite to other moments. The angles formed by the moments and the field depend on the geometry and interactions within the system.

Both ferromagnetic and antiferromagnetic materials have a transition temperature above which the thermal fluctuations of the system outweigh the magnetic interactions and the system exhibits paramagnetic characteristics. For antiferromagnets, this is called the Néel temperature. At temperatures well above this transition, the magnetic susceptibility of antiferromagnetic substances obey the Curie-Weiss law,

$$\chi = \frac{C}{T - \theta_{CW}} \tag{1.1}$$

Here, χ is the susceptibility, C the Curie constant, T the temperature and θ_{CW} is the Curie-Weiss temperature. The sign of θ_{CW} indicates the dominant type of magnetic interaction, with positive corresponding to ferromagnetic and negative to antiferromagnetic. The Curie constant, C, is related to the number density of moments, N, in the system and the size of the magnetic moment by

$$C = \frac{N\mu_0(p_{eff}\mu_B)^2}{3k_B} \tag{1.2}$$

$p_{eff}\mu_B = g\sqrt{J(J+1)}\mu_B$ is the effective moment of the material, μ_B is the Bohr magneton, $\mu_0 = 4\pi \times 10^{-7}$ is the permeability of free space and k_B is Boltzmann's constant. g is the usual Landé g-factor,

$$g = 1 + \frac{J(J+1) + S(S+1) - L(L+1)}{2J(J+1)} \tag{1.3}$$

with J, S and L being the total, spin and orbital angular momenta, respectively.

In the antiferromagnetic phase, application of a sufficiently strong field will cause all of the moments to align parallel to the field, resulting in a saturated paramagnetic phase. With the moments saturated, the magnetization of the sample cannot increase with increasing field. The magnetization at this point is given by

$$M_{sat} = N\mu \tag{1.4}$$

where N is the number density of the moments and $\mu = gJ\mu_B$ is the saturation moment. This is not to be confused with the effective moment found from the Curie-Weiss law.

Strictly speaking, absolute saturation only occurs for very large fields and low temperatures. For a paramagnetic material, the approach to saturation follows the relation

$$M_{sat} = N\mu B_J(y) \tag{1.5}$$

where B_J(y), the Brillouin function, is defined by

$$B_J(y) = \left[\frac{2J+1}{2J}\coth\left(\frac{2J+1}{2J}y\right) - \frac{1}{2J}\coth\left(\frac{y}{2J}\right)\right]$$

and

$$y = \frac{\mu\mu_0 H}{k_B T}$$

In the limit y$\gg$1, equation (1.5) of course reduces to equation (1.4).

At temperatures where a material orders antiferromagnetically in zero field, equation (1.5) will not be followed because the applied field must first overcome the ordering in the material and then the moments can align along the field direction. The result is that the low-field region of the magnetization curve will have an increase in slope where the field overcomes the ordering, entering either a spin-flop or paramagnetic phase. From this phase, saturation is reached, with a saturation magnetization given by equation (1.4).

The field required to saturate the moments, the saturation field, is dependent upon the strength of the interactions in the system. In the molecular field theory the inter-plane interaction strength, J', for the systems considered in this study can be

estimated using the relation

$$J' = \frac{g\mu_B\mu_0 H_{sat}}{2z'S} \tag{1.6}$$

where H_{sat} is the saturation field at T=0, z' is the number of nearest inter-plane neighbours and S is the total angular momentum of the magnetic ion. To avoid confusion with exchange constants, the total angular momentum is often assigned the label S. This practice will be adopted at this point and for the remainder of the thesis J will be used for exchange constants and S for the total angular momentum.

1.1.2 van Vleck Paramagnetism

van Vleck paramagnetism[2, 3] is a quantum mechanical effect arising from non-zero off-diagonal elements of the magnetic moment tensor. These elements result in part of the orbital moment being admixed into the ground state through the orbital Zeeman effect. This is a second order correction term and, as such, is usually small and important only in the case where S=0 and the ground state is non-degenerate, as is the case for shells that are one electron short of being half-filled. However, when the lower order terms are reduced, as by saturation or at high temperatures, the van Vleck term becomes important. This is a field-induced effect so that at zero field it is not present, but at high fields can become the dominant contribution to the susceptibility. The result is that the high-field region of a plot of M *vs* H has a positive slope due to the van Vleck contribution rather than saturating to a constant value. The

van Vleck contribution can be removed and the saturation magnetization estimated by extrapolating the high-field slope back to H=0.

The van Vleck term is independent of temperature as long as the energy difference between higher-lying orbital states and the ground state is less than k_BT, which should be the case for the temperature range being studied here. It is for this reason that the Curie-Weiss law can be modified by simply adding a constant as in equation (6.24).

For the metal ions in the materials studied in this thesis, this contribution is known to exhibit itself. For example, for the Fe^{2+} ion in the crystal field appropriate to $FeBr_2$, the contribution of the van Vleck term to the molar susceptibility is calculated[4] to be of the order 10^{-7} m^3/mol.

1.1.3 Spin Glasses

A spin glass[5] is a material whose moments are frozen in random directions when the temperature is decreased below a certain point known as the freezing temperature, T_F. These materials are characterized by having relaxation effects. Below T_F, the relaxation is extremely slow, characterized by large relaxation times.

This can be caused by competing interactions among the moments. When there is a competition between two or more types of interactions, for example, ferro-

magnetic and antiferromagnetic, each interaction energy is minimized by a different ground state. This results in frustration in the system and many states can minimize the energy of the system without satisfying all of the interactions. For this reason, no conventional long-range order is generally present in a spin-glass system.

Many of the measured properties of spin-glasses are similar to those of superparamagnets. A superparamagnet is a material which contains non-interacting particles which behave like paramagnets, but with much larger magnetic moments. These particles may be large clusters of individual moments aligned together to form large moments. These large moments have large relaxation times, comparable to those of spin-glasses, at low temperatures. In fact, spin-glasses are similar to superparamagnets except that, in the spin-glasses, there are competing interactions among magnetic moments. A system may also be a cluster-glass, where, instead of individual moments, larger clusters of moments exist with competing interactions among clusters.

Above T_F, spin glasses often behave like paramagnets. Below T_F, the magnetization of the sample is highly dependent on its history. If the material is cooled in the absence of a magnetic field, it will have no net ordering as it passes through the freezing transition and the magnetization will be zero. This is known as zero-field cooling (ZFC). If the sample is cooled in a field, the moments will tend to align along the field as the temperature decreases until the freezing point is reached. At

this point, the moments are frozen and the sample maintains a finite magnetization. This is field cooling (FC). Even if the field is turned off, there will still be a magnetization. If a magnetic field is turned on after the ZFC, the magnetization will gradually increase as the moments very slowly relax into alignment with the field.

The property of history dependence can easily be seen in dc magnetization measurements. If the sample is cooled in zero field (ZFC) down to a base temperature below T_F, and then the magnetic field is applied to take measurements as the sample is warmed, the magnetization will grow as the moments slowly align with the field. As the temperature approaches T_F, it becomes easier for the moments to move and the magnetization increases more quickly. Once the temperature reaches T_F, however, the magnetization peaks and begins to decrease as random thermal motion of the moments decreases the net magnetization. If the same measurements are taken as the sample is cooled back down in the presence of a field, the magnetization will trace the same path backwards until T_F is reached. At this point, the moments begin to freeze and the rate of increase in magnetization seen above T_F is reduced. Some increase may still be present near T_F, but well below the magnetization will remain constant while the moments are frozen into position.

Ac susceptibility measurements show a slightly different result. Above T_F, since the material tends to behave as a paramagnet, the real part of susceptibility, or the dispersion, χ', will drop off roughly as 1/T. Near the freezing temperature, as

the motion of the moments becomes stiffer, χ' decreases and drops to zero slightly below T_F. The imaginary component, or absorption, χ'' behaves differently. Above the peak temperature for χ', the absorption is constant at zero. At the peak temperature, with the sudden increase in relaxation time of the system, χ'' increases sharply to a peak and then decreases back to zero as the temperature decreases further. The result is that the peak in χ' is seen at a slightly higher temperature than that in χ'', corresponding to a maximum in $\frac{d\chi'}{dT}$.

Another peculiarity about the ac susceptibility of a spin glass is its dependence on the measurement frequency. Because of the relaxation time involved in this transition, χ' is very sensitive to the frequency of the oscillating field used to measure it. As the frequency is increased, the peak temperature increases and the magnitude of the peak decreases.

The frequency dependence of the peak temperature, like that in a superparamagnet, can be fit to an Arrhenius law

$$f = f_0 \exp(\frac{E_a}{k_B T}) \tag{1.7}$$

in which E_a is the activation energy for a thermally excited process. Such a fit for spin glasses tends to give unphysically high values for f_0 and E_a. Much better fit, except at low frequencies, can be obtained by using a Vogel-Fulcher law[5, 6], originally used

to describe the viscosity of supercooled liquids,

$$f = f_0 \exp(\frac{E_a}{k_B(T - T_0)}) \tag{1.8}$$

where T_0 is a temperature lower than the freezing temperature. Clearly, the fit must be better with the addition of the extra parameter, although this is not always the case at low frequencies. More importantly, however, the values of E_a and f_0 have more physically reasonable values. The physical interpretation of the parameters, however, is not obvious.

Superparamagnets tend to have a much higher dependence on frequency than do spin-glasses. The change in peak temperature caused by changing the frequency by a factor of 10 is typically two orders of magnitude higher in a superparamagnet than in a metallic spin-glass or one order of magnitude for an insulating spin glass[6].

Specific heat measurements show no anomaly at a spin glass transition, as there would be in an antiferromagnetic transition. Often, however, there is a broad peak that appears at a temperature above the transition. Well below the freezing temperature, the specific heat varies as $C \propto T$, compared to the usual form of $C = \alpha T + \beta T^3$ for a three-dimensional lattice.

Chapter 2
Materials

The materials studied in this thesis are the graphite intercalation compounds of $CoBr_2$, $FeBr_2$ and $NiBr_2$. In this chapter, we describe the materials before intercalation as well as the intercalation process and the characterization of the compounds by x-ray analysis. As a means of comparison, the analogous chloride compounds are also described.

2.1 Bromides

The dibromides of cobalt, iron and nickel are layered magnetic materials with planes of metallic atoms separated by two layers of bromine atoms. In all cases, the atoms within a layer are arranged trigonally, with the stacking arrangement of the layers varying among the materials. The interactions among magnetic atoms are ferromagnetic between nearest neighbour atoms within the same plane and antiferromagnetic between out-of-plane neighbours. The result is an antiferromagnetic ground state in which the magnetic moments within a given sheet of metallic atoms are parallel to each other while adjacent sheets are anti-parallel. These bromides belong to the class of materials known as metamagnets, which undergo a transition

from an antiferromagnetic to a ferromagnetic (saturated paramagnetic) state with the application of a sufficient magnetic field.

All three materials are hygroscopic and react with moisture in air to form hydrated compounds. To ensure purity, the materials must be handled only in an inert, dry atmosphere. The materials used in this study were in powder form and of high purity (99% by metals basis). The purity of the powders was confirmed by us with powder x-ray diffraction.

2.1.1 Cobalt Bromide

$CoBr_2$ is a green crystalline material which melts at 678°C[7]. The layers of cobalt are stacked in an A-A-A arrangement as seen in Fig. 2.1a, such that out-of-plane neighbour cobalt atoms are aligned directly above each other in the c-direction. Bromine layers follow a B-C...B-C arrangement. This gives the compound a hexagonal symmetry, space group $D^3_{3d}(P\bar{3}M)$. The Co-Co distance is 3.278 Å in-plane and 6.169 Å[8] between neighbouring planes.

The Co^{2+} ion has a $(3d)^7$ electron configuration. The Br^- ions surrounding the Co^{2+} ion form a slightly distorted octahedron, giving rise to a crystal field with cubic symmetry, which has a ground state that is triply degenerate[1]. The neighbouring Co^{2+} ions create a trigonal symmetry in the crystal field. This creates a strong

anisotropy that tends to constrain the spins to lie in the plane. A slight distortion of the crystal field tends to align the spins preferentially in one direction. The effective spin of the Co^{2+} ion in this crystal field is 1/2.

The Hamiltonian used for $CoBr_2$ is[9]

$$\mathcal{H} = -\sum_{(i,j)}(J_{ij}\vec{S}_i \cdot \vec{S}_j - D_{ij}S_{ix}S_{jx}) - J'\sum_{(i,k)}\vec{S}_i \cdot \vec{S}_k \qquad (2.1)$$

Here, the first sum is over first, second and third nearest in-plane neighbours with associated isotropic exchange constant J_1, J_2, J_3 and anisotropic exchange constants D_1, D_2 and D_3. The second term is the sum over inter-plane nearest neighbours with exchange constant J'. The x-direction is taken to be along the c-axis.

As early as 1939, de Haas and Schultz[10] measured the susceptibility of $CoBr_2$. Their results had poor reproducibility, but they determined that the high temperature phase was paramagnetic and fit a Curie-Weiss law with C=3.41 emu·K·mol^{-1} and θ_{CW}=-6 K. They were unable to determine a transition from their data. Bizette *et al.*[11, 12] later measured the Néel temperature to be 19 K from their susceptibility data. They also fit to a Curie-Weiss law, but with C=3.34 emu·K·mol^{-1}, p_{eff}=5.2 and θ_{CW}=-20 K.

Wilkinson *et al.*[8], using neutron diffraction on powder samples, were able to determine the magnetic structure and verify the Néel temperature. The magnetic moments of the cobalt atoms lie in the a-b plane. They were also able to determine

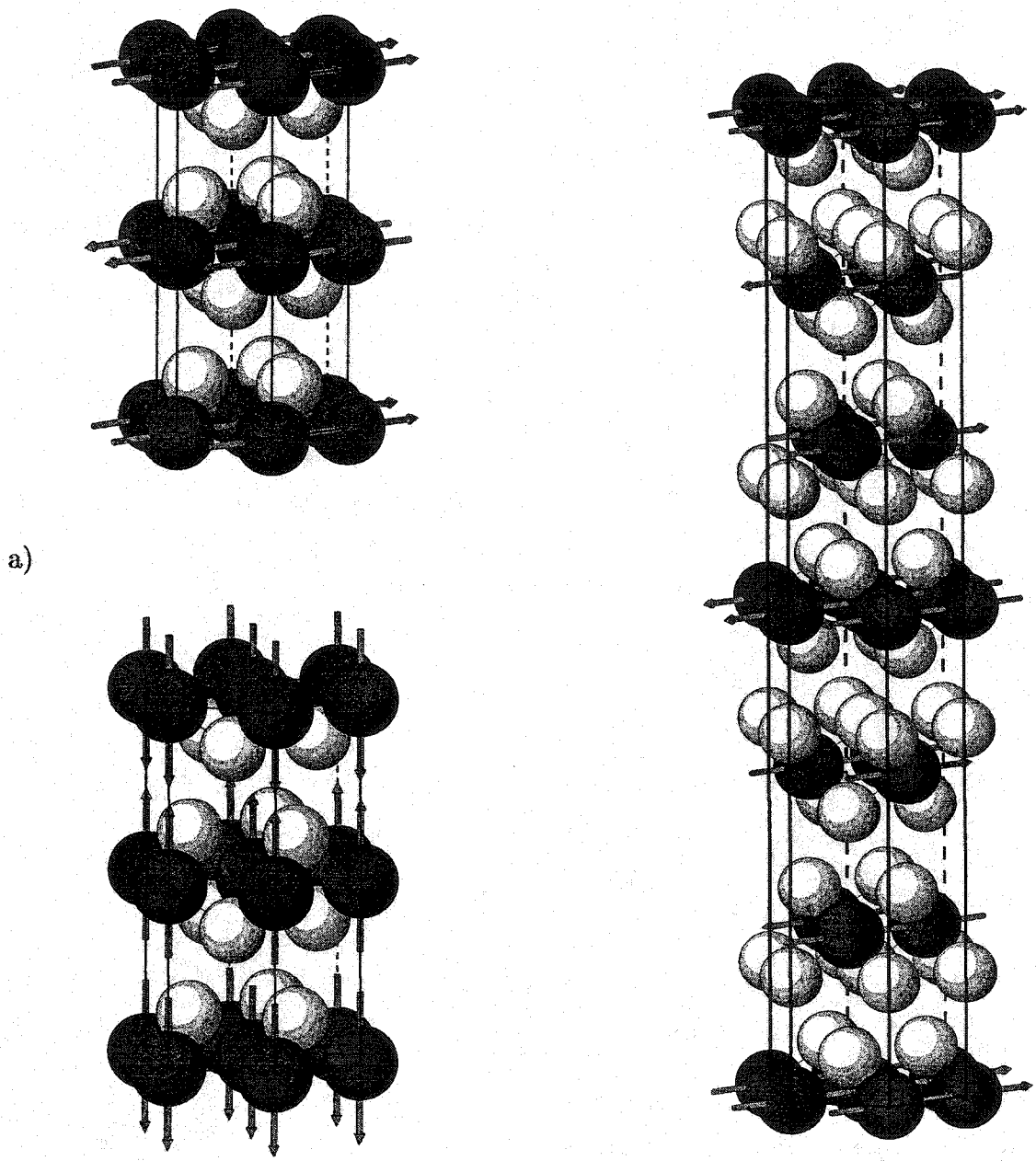

a)

b)

c)

Figure 2.1: Crystal and magnetic structure of a) $CoBr_2$, b) $FeBr_2$ and c) $NiBr_2$. The dark atoms are the metallic atoms and the bromine atoms are white. Arrows schematically show the preferred orientation of magnetic moments.

the saturation moment to be $3.0\pm0.6\mu_B$ per ion, consistent with the effective spin-1/2 Co^{2+} ion.

It was found that, at low temperature, with the application of a small in-plane magnetic field, the material enters a spin-flop phase[13, 14], where the magnetic moments move away from the preferred $\langle 210 \rangle$ direction[15] and align perpendicular to the field. This phase saturates at H=80 kOe, where the material becomes a saturated paramagnet.

Yoshizawa *et al.*[9] studied the two-dimensionality and the XY-characteristics of $CoBr_2$ using inelastic neutron scattering from a single crystal. They were able to determine the exchange parameters for the material and found $-J'/J_1=0.483$, indicating some three-dimensional behaviour, and $D_1/J_1=0.567$, indicating XY characteristics. This was later confirmed by Schmidt *et al.*[15]. Both report that interactions up to third near in-plane neighbours are required to fit their data.

The research done has shown that $CoBr_2$ is an antiferromagnet with $T_N=19$ K. The ordering in the antiferromagnetic phase consists of planes of magnetic atoms whose moments are aligned ferromagnetically along the $\langle 210 \rangle$ direction with neighbouring planes aligned antiferromagnetically. At low temperatures, the application of a small magnetic field induces a spin-flop, which is saturated at 80 kOe.

2.1.2 Iron Bromide

$FeBr_2$ is green-yellow in colour, decomposes at 684°C[7] and has the same stacking arrangement and symmetry as $CoBr_2$ (see Fig. 2.1b). The in-plane and out-of-plane Fe-Fe distances are 3.772 Å and 6.223 Å, respectively.

Since the lattice has the same symmetry as in $CoBr_2$, so too does the crystal field. In this case, however, since the Fe^{2+} electronic configuration is $(3d)^6$, the magnetic moments of the iron atoms align preferentially along the c-axis.

The Hamiltonian used for $FeBr_2$ is[16, 17, 18]

$$\mathcal{H} = -\sum_{(i,j)} J_{ij} S_i S_j - J' \sum_{(i,k)} S_i S_k \tag{2.2}$$

where the first sum is over nearest and next-nearest in-plane neighbour pairs and the second sum is over inter-plane near neighbour pairs. The dot products are not necessary since the moments are assumed to be ± 1 along the c-direction only.

Bizette *et al.*[19], with a Curie-Weiss fit to the magnetic susceptibility, found C=3.92 emu·K·mol^{-1}, θ_{CW}=6 K and p_{eff}=5.62. In 1959, Wilkinson *et al.*[8] used neutron diffraction to study powder samples of $FeBr_2$ and determined the magnetic structure in the antiferromagnetic phase. They found the transition temperature to be T_N=11 K and the saturation moment to be 4.4±0.7 μ_B per ion. Jacobs and Lawrence[4] studied the metamagnetic transition by measuring the magnetization as a function of applied field. They found this transition to occur at 31.5 kOe at T=4.2K

and determined the saturation moment to be $4.05\pm0.2\mu_B$ per ion. Above the metamagnetic transition, they saw a linear increase in magnetization which they attributed to a van Vleck "temperature-independent" paramagnetism.

Heat capacity measurements in 1971 by Brade and Yates[20] showed a peak at 11.4±0.1 K. Their analysis indicated that 58% of the change in entropy occurred slightly above T_N. This was taken to indicate significant short-ranged ordering just above the transition. Lanusse *et al.*[21] studied single crystals with heat capacity measurements and found T_N=14.2 K, significantly higher than previous measurements. The peak was also much sharper and had less entropy change on the high-temperature side. This seems to indicate that single crystals have a higher transition temperature and that, perhaps, the entropy change on the high-temperature side in [20] was caused by larger crystallites in the powder sample.

Magnetization isotherms measured by Fert *et al.*[22] in 1973 showed a first order field-induced transition below T=4.6 K with a saturation field H_S=28.5±0.2 kOe and a saturation moment of $3.9\pm0.1\mu_B$ per ion, independent of temperature within this range. A second order transition was observed in the temperature range from T=4.85 K to T_N=14.2 K. It was also seen that the first and second order lines do not meet smoothly, but rather at an angle with respect to each other at the tricritical point, TCP. A schematic of this phase diagram is presented in figure 2.2a. The solid line represents the first order transition and the dashed line the second order

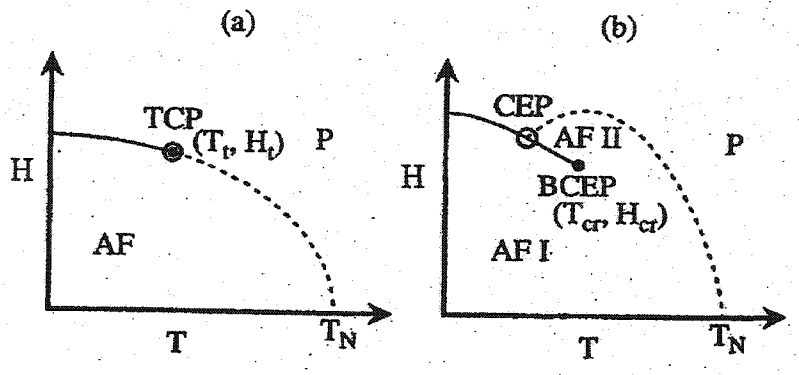

Figure 2.2: Phase-space diagram for a) a material with a tricritical point (TCP) and b) a material in which the tricritical point has decomposed into a bicritical endpoint (BCEP) and a critical endpoint (CEP). Taken from ref. [23]

transition. The figure shows them meeting smoothly at TCP rather than at an angle as found in [22]. The antiferromagnetic (AF) and paramagnetic (P) regions are indicated.

Vettier *et al.*[24] made similar measurements with the application of pressure to locate the tricritical line in (H,T,P) space, where the first and second order lines meet in the (H,T) phase diagram. The tricritical point at zero pressure was identified as $(T_{3c},H_{3c}) = (4.6\ K, 28.5\ kOe)$, but they indicated some difficulty in defining the order of the transition within 0.5 K of T_{3c}.

More recently, anomalies have been seen in the magnetic properties of $FeBr_2$ near the transition. de Azevedo *et al.*[25] studied the magnetization and ac susceptibility as a function of field and found peaks in both dM/dH and χ' at H_c in the second order transition region as expected. χ'', however, showed peaks above and below the

critical field with a minimum near the critical field, H_c. The results were confirmed with temperature dependent measurements. This indicates strong non-critical fluctuations above and below the critical point with the critical fluctuations being partially suppressed. They proposed that fluctuations occur because of transient spin structures within the sublattice whose magnetization is opposite to the direction of the applied field. These fluctuations are caused by intraplanar frustration. The results were qualitatively confirmed by Monte Carlo(MC) simulations which showed transient spin structures under conditions similar to the $FeBr_2$ lattice.

Further MC simulations by Selke and Dasgupta[16] showed that broad features on the low temperature side of the peaks in dM/dT and heat capacity measurements could be qualitatively reproduced if ten near interplanar neighbours with equivalent exchange paths are included rather than the single geometric nearest neighbour. Selke[17] showed that the tricritical point could be decomposed into a critical endpoint (CEP) and a bicritical endpoint (BCEP), as shown in figure 2.2b. In the region between these points above the first order (solid) line and below the second order (dashed) line, there exists a second antiferromagnetic phase (AFII) where both sublattices are oriented along the field direction, but with one sublattice having a larger net magnetization than the other. In the low temperature regime, a combined antiferromagnetic and paramagnetic phase is seen, indicating the field-induced metamagnetic transition.

Specific heat measurements by Aruga Katori *et al.*[18] showed the presence of anomalous peaks. In zero-field, only one peak is seen at T_N=14.2 K. From H=1.4 to 2.9 T, a second peak is present at a temperature below the antiferromagnetic transition. The second peak disappears and above 3.3 T, a broad peak appears above the antiferromagnetic peak. This confirms the existence of a region of non-critical fluctuations above and below the antiferromagnetic transition. Neutron scattering results from Katsumata *et al.*[23] are consistent with the existence of an AFII phase in the region between the CEP and the BCEP. Measurements of magnetization parallel and perpendicular to the plane[26] showed that the non-critical fluctuations are induced in the axial spin component, not in the transverse components. The endpoints are located at CEP=(10.8 K, 1.1 MA/m) and BCEP=(4.6 K,2.4 MA/m)[23, 26].

$FeBr_2$ is shown to be an antiferromagnet with ferromagnetic layers coupled antiferromagnetically, as in $CoBr_2$. Unlike $CoBr_2$, however, the moments are aligned along the c-axis, making it an Ising-like system. The first and second order transition lines in the (H,T) phase diagram meet at an angle at a critical endpoint. The first order line extends past the CEP and ends at a bicritical endpoint (BCEP). The region between the first and second order lines is antiferromagnetic with both sublattices aligned along the field but with different magnetizations.

2.1.3 Nickel Bromide

$NiBr_2$ is yellow-brown and melts at 963°C[7], significantly higher than those of the other two materials. The stacking arrangement of the magnetic layers in $NiBr_2$, shown in Fig. 2.1c, is an A-B-C arrangement such that each nickel atom has three nearest neighbours above and below in neighbouring planes. The bromine layers then follow a CB-AC-BA arrangement. The unit cell for this structure is rhombohedral and the space group is $D^5_{3d}(R\bar{3}M)$. It is often more convenient to consider a larger hexagonal cell which contains three molecules, for which the cell parameters are a = 3.65 Å and c = 18.23 Å. However, since the hexagonal cell spans three layers, the interplanar distance between Ni planes is c/3 = 6.08 Å.

The Hamiltonian used for $NiBr_2$ is[27, 28]

$$\mathcal{H} = -\sum_{(i,j)} J_{ij}\vec{S}_i \cdot \vec{S}_j - J' \sum_{(i,k)} \vec{S}_i \cdot \vec{S}_k + D\sum_i (S_{iz})^2 \tag{2.3}$$

The first sum is over in-plane pairs of first, second and third nearest neighbours. The exchange constant J_{ij} ranges over J_1, J_2 and J_3, respectively, for these cases. The second sum is over inter-plane nearest neighbour pairs with J′ the exchange constant. The last sum is the single-ion anisotropy term, with the z-axis being along the direction of preferred orientation.

Early measurements of the magnetic susceptibility by Tsubokawa in 1960[29] indicate a Néel temperature close to 60 K, an effective moment of $3.0\mu_B$ and an es-

timated Curie temperature of -20 K. Measurement of the magnetization *vs* field by Morimota and Date in 1970[30] exhibited a step at 27 kOe for T=4.2 K. Magnetic resonance data also indicated a transition at this field. This was associated with an intrinsic spin orientation below 20 K, but the exact nature was unknown at the time. In 1976, Day *et al.*[31] studied powdered samples of $NiBr_2$ using neutron diffraction and optical absorption spectra and determined T_N to be 52 K. Furthermore they found a lower transition temperature of 22.5 K at which point they believed the spins canted out of the basal plane by 54^o.

In 1980, Adam *et al.*[32] argued that the rearrangement of spins at the lower temperature must be within the basal plane. C-axis magnetization measurements showed no anomaly at this temperature, whereas in-plane measurements showed a discontinuity at T=22 K. They studied both single crystal and powdered samples with neutron diffraction. The powder sample also showed T_N=52 K with a saturation moment of 2.0 $\pm$0.15 μ_B per Ni ion, consistent with the S=1 ground state of the Ni^{2+} ion. They also noticed a slight shift in the position of the [0 0 3/2] peak between 30 K and 4.2 K, which was not seen in the [0 0 3] peak. This is consistent with a change in propagation wavevector. Single crystal neutron diffraction showed that the low-temperature phase is in fact an incommensurate helical structure with a wavevector (0.027,0.027,3/2) at 4.2 K. This changes continuously to (0.09,0.09,3/2) at 22.8 K, where it undergoes a discontinuous transition to (0,0,3/2), associated with the antiferromagnetic state. Furthermore, the Néel temperature for the single crystal sample

was determined to be 44 K, significantly lower than the powder samples. At all temperatures, the magnetic moments lie in-plane. The existence of the incommensurate (helical) phase at lower temperatures than the commensurate (antiferromagnetic) one is explained by considering interactions within the plane up to third near neighbours and an ordering temperature very near to a Lifshitz point, where a commensurate phase, an incommensurate phase and a disordered phase meet. In two dimensional systems, this can lead to a first order transition. Further measurements by Adam *et al.*[33] show that the application of pressure decreases the field required to go from the helical to the antiferromagnetic phase and moves the system away from the Lifshitz point.

Régnault *et al.*[27] reported that molecular field theory (MFT) predicts a second order transition from the helical to antiferromagnetic phase, whereas a first order transition is seen experimentally. This may be the result of thermally induced fluctuations which are ignored in MFT. Their neutron scattering data determine the interaction constants in plane to be J_1=1.56±0.02 meV, J_2=-0.018±0.02 meV and J_3=-0.41±0.02 meV for the nearest, next nearest and third near neighbour interactions, respectively. The inter-plane interaction, J′, is determined to be -0.182 ±0.005 meV. They further found the critical field to be H_C=27 kOe and the saturation field H_S=380 kOe with a saturation moment of $2.27\mu_B$ per ion.

Heat capacity measurements by White and Staveley[34] determined that T_N=45.5

± 0.5 K, in good agreement with neutron data, but T_{ic}=19.5 K, slightly lower than expected. They did, however, observe a broad feature with a maximum at 23 K. They conjectured that the different types of measurements are sensitive to changes in different properties and that the observations are, in fact, consistent with each other.

Yoshiyama *et al.*[28] predicted, using MFT calculations, that, as the applied field is decreased from the saturated paramagnetic state, the system should go through a fan phase before entering the AF phase. They predicted that the transitions would occur at 331 kOe and 325 kOe, respectively. Nearly simultaneously, Katsumata *et al.*[35] observed these transitions at 329 ± 2 and 321 ± 2 kOe, in remarkable agreement. They also determined the saturation moment to be $2.1 \pm 0.1 \mu_B$ from the saturation magnetization.

Nickel bromide is seen to have a similar structure to the other two compounds, but with a slightly different stacking arrangement. The magnetic ordering is similar to that of $CoBr_2$ in that the ferromagnetic layers are coupled antiferromagnetically with moments lying in the plane. The Neél temperature is much higher at 44 K, and below 22.8 K, a helical phase is entered. At low temperatures a high field-induced fan phase can be seen between the antiferromagnetic and paramagnetic phases.

2.2 Chlorides

The analogous metal chlorides, $CoCl_2$, $FeCl_2$ and $NiCl_2$, are structurally very similar to the bromides. In all cases, the chlorides have the rhombohedral symmetry of $NiBr_2$. As in the case of $NiBr_2$, it is often easier to refer to the lattice in terms of a hexagonal cell which contains three molecules and spans three layers. Because of their similarity, these materials will serve as a useful comparison for the bromides and their GICs.

All of the materials are antiferromagnetic, with ferromagnetic layers coupled antiferromagnetically along the c-direction.

2.2.1 Cobalt Chloride

$CoCl_2$ is blue in colour, melts at 724°C and boils at 1049°C[7]. It is hygroscopic and absorbs water to form hydrated compounds. The lattice dimensions, a=3.553 Å and c=17.359 Å(Co-Co interplane distance 5.79Å)[8] are slightly smaller than those of $CoBr_2$.

Early susceptibility measurements by de Haas and Schultz[10] showed that a Curie-Weiss law was obeyed at high temperatures, with the parameters C=3.54 emu·K·mol^{-1} and θ_{CW}=19 K. Starr *et al.*[36] obtained values of C=3.46 emu·K·mol^{-1} and θ_{CW}=38.1 K with an effective moment of 5.29μ_B, while Bizette *et al.*[12] found

C=3.33 emu·K·mol^{-1}, θ_{CW}=20 K and p_{eff}=5.18. The source of the discrepancies in the Curie-Weiss temperature is not clear, but the most often cited value is 38.1 K.

Wilkinson *et al.*[8] determined that the moments of the magnetic ions lie within the plane and at low temperature align preferentially along the ⟨210⟩ directions. They further found that the saturation moment was 3.1μ_B. Moses *et al.*[37] found a spin-flop phase at 4.2 K with the application of an in-plane field as small as 2 kG, which saturates at 33 kG.

2.2.2 Iron Chloride

$FeCl_2$ is green to yellow and melts between 670-674°C[7]. This compound is deliquescent, i.e., it absorbs moisture from the air and becomes liquid. The lattice parameters are a=3.603 Å and c=17.536 Å[8].

Starr *et al.*[36] measured the susceptibility and fit a Curie-Weiss law with C=3.59 emu·K·mol^{-1}, θ_{CW}=48.0 K and p_{eff}=5.38. The Néel temperature is 23.5 K from specific heat measurements, 24 K from the maximum in susceptibility measurements. Wilkinson *et al.* found that, as in $FeBr_2$, the moments align along the c-axis, with a saturation moment of 4.4μ_B.

Jacobs and Lawrence[38] studied the metamagnetic transition and determined the saturation moment from the saturation magnetization to be 4.3μ_B. The phase

transition is of first order below T=20.4 K and second order above that temperature. Below the tricritical point, the transition involves going through a mixed antiferromagnetic and paramagnetic phase as in $FeBr_2$[39]. Unlike $FeBr_2$, the tricritical point does not seem to split into two critical end points.

2.2.3 Nickel Chloride

$NiCl_2$ is a yellow material that melts at 1001°C, but sublimes at 973°C. Like $FeCl_2$, it is a deliquescent material. Its lattice parameters are a=3.465 Å and c=17.30 Å.

Starr *et al.*[36] found the susceptibility fit a Curie-Weiss law with C=1.36 emu·K·mol^{-1}, θ_{CW}=68.2 K and p_{eff}=3.32. The Néel temperature was seen to be near 50 K. Busey and Giauque[40] reported a specific heat anomaly near 52 K, attributed to the Néel temperature.

Using neutron diffraction Billerey *et al.*[41] were able to determine the saturation moment to be 2.0±0.15 μ_B.

Unlike the case of $NiBr_2$, there is no low temperature incommensurate phase that has been seen in $NiCl_2$.

2.2.4 Comparison to Bromides

While being very similar to the bromides, the above chlorides are different in several ways. For both the iron and cobalt compounds, the stacking arrangement is different between the bromide and the chloride. In the bromides, the metal atoms in successive planes lie one on top of the other whereas in the chlorides, the metal atom in one plane lies on top of a hole in the plane beneath it, in an ABC stacking arrangement. This means that there is a slight difference in the number of and distance to geometric near neighbours out-of-plane. This difference may not be as important in the magnetic interactions since the inter-plane interactions are achieved through a superexchange path through the halides. In this sense, the change in halide is probably more important than the change in distance.

The lattice spacings are smaller for the chlorides than for the bromides. This again is because of the different halide. Bromine ions have larger radii than chlorine ions(1.95 Å for Br, 1.81 Å for Cl[42]). This inherently leads to larger molecules and larger lattice spacings.

In all cases, the Néel temperature is higher for the chloride than for the bromide of the same metal.

The chlorides all have positive values for the Curie-Weiss temperature, whereas these values for the bromides are negative, except for $FeBr_2$, which is positive but

Table 2.1: Comparison of bromides and chlorides.

Material	a (Å)	I_c (Å)	T_N (K)	θ_{CW} (K)	p_{eff}	μ (μ_B)
$CoBr_2$	3.278	6.169	19	-20	5.2	3.0
$FeBr_2$	3.772	6.223	14.2	6	5.62	4.0
$NiBr_2$	3.65	6.08	44.6*	-20		2.0
$CoCl_2$	3.553	5.79	25	38.1	5.2	3.1
$FeCl_2$	3.603	5.85	23.5	48	5.4	4.3
$NiCl_2$	3.465	5.77	52	68.2	3.3	2.0

*$NiBr_2$ also has a helical phase below 22.8 K.

still much less than that of $FeCl_2$. This implies that the bromides have a stronger antiferromagnetic interaction relative to the ferromagnetic interaction than do the chlorides. This may, at first, seem rather counterintuitive. Given that the bromides order at lower temperatures than do the chlorides, one might expect that the chlorides must have stronger antiferromagnetic interactions. However, if we consider that some of the antiferromagnetic interactions are next-nearest and third near neighbour interactions within the plane, it can be seen that these would serve to weaken the ferromagnetic ordering within the plane without increasing the inter-plane ordering and, hence, retard the overall ordering in the crystal.

A summary of the comparison between the metal bromides and metal chlorides is given in table 2.1. I_c is the inter-planar distance, equal to c in the cases of $CoBr_2$ and $FeBr_2$, but c/3 for the others.

2.3 Graphite

Graphite is the most common allotrope of elemental carbon. In this layered material, each carbon atom is bonded covalently to three other atoms with σ bonds within the plane. In this fashion, the graphite atoms form six-member rings in flat planes. Adjacent planes are held together weakly by van der Waals forces. The formation of rings gives rise to delocalized π electrons above and below each plane. These π electrons allow for conduction of electricity with the conductivity parallel to the planes being much greater than that perpendicular to the planes.

The host compound for the materials in this study is highly-oriented pyrolytic graphite (HOPG) generously given to us by Dr. Moore. HOPG is a synthetic form of graphite created by cracking hydrocarbons at high temperatures, followed by heat treatment under pressure[43]. The resulting graphite compound consists of many crystallites with a high degree of alignment in the c-direction, perpendicular to the planes, but randomly oriented in the a-b plane. The size of the crystallites is typically $\sim$1 μm in diameter. The inter-plane spacing is 3.35 Å, while the in-plane C-C bond length is 1.42 Å as in natural graphite.

Natural graphite flakes can be found in mineral deposits. The graphite can be removed by dissolving the rock in acid. Single crystal flakes found in this manner are usually very small, making them more difficult to use for measurement purposes. Larger crystals can be obtained from kish graphite. Kish graphite is the crystalliza-

tion of carbon from molten steel in the steel-making process. These crystals are less ordered than natural graphite, but more so than HOPG. Because of its synthetic production, HOPG offers the largest sample size. The single crystals used in this project were extracted from calcite deposits found in New York state.

2.4 Intercalation

Graphite intercalation compounds (GICs) are formed by the insertion of chemical species into the inter-layer spacing of graphite. In general, intercalation leaves the in-plane properties (e.g., lattice spacing) of both the intercalant and graphite nearly the same as before intercalation[43]. Graphite, itself is diamagnetic, but loses this property with the intercalation of another chemical species.

There are two general classifications of GICs, based on the type of charge transfer that takes place between the graphite layers and the intercalant. Donor compounds have a decrease in the electron density in the intercalant material from charge transfer to graphite, whereas acceptor compounds, such as those formed in the intercalation of metal-halides, have a transfer of charge from the delocalized π bonds of the graphite layers to the intercalant. The type of compound formed depends on the intercalant material's ability to oxidize or reduce graphite. Lewis acids, on intercalation, tend to oxidize the graphite layers and form acceptor compounds. Lewis bases reduce the graphite and form donor compounds.

An important phenomenon in the intercalation process is that of staging[43]. The intercalation process is controlled by the lattice strains induced by introducing the intercalant molecules into the graphite lattice. These strains are minimized by packing intercalant molecules into clusters within a layer, while separating intercalated layers as far as possible in the c-direction. The result is a series of evenly-spaced intercalant layers. The number of carbon layers between consecutive intercalant layers is called the stage index, n, and the distance between these intercalant layers is the repeat distance, I_c. Thus, a stage-n compound has n carbon layers between successive intercalant layers and a repeat distance approximately equal to (n-1) times the carbon interplane separation plus the intercalant size.

As intercalant is added to the system, the clusters grow in size and eventually meet each other. In the ideal model, the clusters meet in the same layer and merge. Eventually, the layer would be filled with intercalant and to add any more, the stage would have to be decreased. In order for the staging to be homogenous, this would have to involve either diffusion across the graphite layer or complete withdrawal of the intercalant and re-insertion into a different inter-layer space. This is obviously an unlikely model.

A likely model is that of Daumas and Hérold[44]. When enough intercalant has been added to the system, the intercalant clusters meet, but not necessarily within

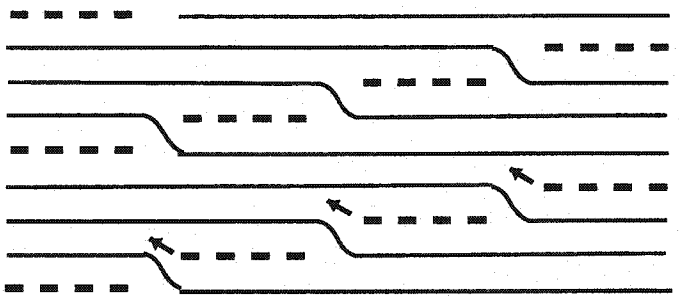

Figure 2.3: Schematic of the Daumas-Hérold domain model. A third stage compound is shown. The solid lines represent graphite layers and the dashed lines the intercalant. Arrows indicate possible movement of intercalant domains to decrease the staging.

the same plane. That is, they are separated both horizontally and vertically by a pleat in the layer of graphite. When this happens, the intercalant domains can slide on top of one another and the stage index is reduced. A simple schematic diagram of the domain model and the staging effect is shown in figure 2.3. If the domains (dashed lines) move relative to the graphite layers (solid lines) as shown by the arrows, the stage index is reduced from three to two. The figure is a schematic only and the actual horizontal distance between domains is generally larger than the repeat distance. Once the intercalation process is halted, the domains remain fixed in size and position.

The resulting domain structure has been seen in many intercalated materials, in particular the metal halides. Flandrois *et al.*[45], using x-ray diffraction with the $NiCl_2$-GIC determined the in-plane coherence length of Ni to be of order 100 Å, implying that this was the domain dimension. This was supported by the amount of charge transfer and the stoichiometry of the material. Later, small angle neutron scattering was used to determine a domain diameter of ~150 Å in the same material[46].

Hwang *et al.*[47] studied $SbCl_5$-GIC with secondary ion mass spectroscopy and scanning transmission electron microscopy and found domains with diameters of ~200 Å. Matsuura *et al.*[48] used electron diffraction to see domains in $CoCl_2$-GIC approximately 150-170 Å in size. Wiesler *et al.*[49] reported neutron and x-ray diffraction results for $NiCl_2$-GIC which are consistent with much larger domains, of diameter 650±150 Å.

For many intercalant materials, including most transition metal halides, it has been shown that it is necessary to intercalate in an atmosphere of halide gas[43]. The bromides studied here are no exceptions to this. It was found that intercalation does not occur without a bromine atmosphere and that a threshold pressure of nearly 1 atm at room temperature (~2 atm at reaction temperature) was required. Additional bromine was not seen to increase the reaction rate, but this was not studied extensively.

It is believed that the domain boundaries provide a location for the excess bromine from the atmosphere[50]. Since most of the metal halides are layered materials, they have no dangling bonds at the edge of an intercalant domain. However, the metal atoms at the edge are not bonded to the same number of halogen atoms as those inside the cluster. The bromine is able to attach to the periphery of the cluster to complete the coordination of the outer metal atoms. This leaves a hole in the valence band, which acts as an acceptor site for electrons from the π orbitals of

the graphite planes.

2.5 Metal-Chloride-GICs

Over the past few decades, many metal chlorides have been intercalated into graphite. Because of the similarities between the bromides and chlorides, it is useful to describe the properties of the metal chloride-GICs, which will serve as a comparison for the bromide-GICs.

2.5.1 $CoCl_2$-GIC

Karimov[51, 52], using magnetization and specific heat measurements, was able to determine two transition temperatures in $CoCl_2$-GIC. The susceptibility had a cusp at T_{cu}=9.05 K. The sample possessed a remanent field below T_{cl}=8.2 K. The specific heat showed a maximum at 8.8 K, and an irregularity at 8.2 K.

Several other authors have observed the existence of two phase transitions in $CoCl_2$-GIC[53, 54, 55, 56]. The higher temperature, T_{cu} was believed to be a two-dimensional ordering transition, and the lower temperature, T_{cl} a three-dimensional ordering transition. A remanent field, seen as a difference between zero field cooled and field cooled measurements, was seen to appear just above T_{cu}. Neutron diffraction has shown that the lower temperature is associated with the onset of antiferro-

magnetic ordering[55], although this ordering appears to be short-ranged[49]. In the region between the two transitions, only two-dimensional ordering is seen.

The magnetic susceptibility shows peaks at both transitions, but for lower stages, the transition temperatures are too close to resolve two distinct peaks. Rather, a large peak is seen at T_{cl} with a shoulder at T_{cu}. As the stage increases, so does the separation of the peaks, but there is little change in the lower transition temperature[56]. It was also seen that the application of a magnetic field quickly decreases the peak height.

It has been suggested that T_{cu} is associated with a Kosterlitz-Thouless phase transition[57], modified by the six-fold symmetry of the graphite lattice as shown by José *et al.*[58]. Attempts to fit to the high-temperature side of the susceptibility peak showed a good fit, but over a limited range. It is noted that the expected range for the fit is only about 1 K above the transition, so that the results are inconclusive. A high temperature Curie-Weiss fit gives θ_{CW}=31 K[55].

Nichols and Dresselhaus[59] studied the ac susceptibility of stages-1, 2 and 3 of $CoCl_2$-GIC. The second and third stage compounds both showed a peak in χ' and two peaks in χ''. The upper peak in χ'', which appears to match a shoulder in χ', is denoted T_{cu} and the lower peak, which is slightly lower in temperature than the peak in χ', is denoted T_{cl}. It is likely that the lower temperature peak in χ'' is actually

associated with the peak in χ'. In the stage-1 compound, χ' has two peaks but χ'' has only a single peak at T_{c2}, which matches the upper peak in χ'. This temperature is shown to be close to T_N, as determined through neutron scattering. The lower peak in χ' is attributed to lower sample quality.

Suzuki has shown[60] that there is a strong frequency dependence of the ac susceptibility peaks in the second stage compound. He interprets this as showing that the phase below T_{cl} has cluster-glass properties with three dimensional antiferromagnetic ordering. Between T_{cl} and T_{cu}, it is believed that long-range two dimensional ordering is established within each domain. Based on the peak structure of higher stage compounds, it is likely that this situation applies to stages n>2 as well. The first stage compound, however, does not appear to undergo this same two stage transition.

Electron diffraction[54, 55] has shown that the $CoCl_2$ maintains its in-plane structure, but that its lattice is incommensurate with that of the graphite host.

2.5.2 $NiCl_2$-GIC

The $NiCl_2$-GICs have properties very similar to those of the $CoCl_2$-GICs. Again, two transitions are seen, T_{cu} and T_{cl}. The transition temperatures are much higher than those for $CoCl_2$-GIC. Karimov[52] reported values of 18.1 K and 20.3 K. Suzuki[61] found values of 17.3 K and 19.4 K for the stage-2 compound. A Curie-

Weiss fit[62] gives θ_{CW}=75 K, compared to 68 K for the pristine material. A similar fit for stage-1 $NiCl_2$-GIC by Flandrois *et al.*[63] yields θ_{CW}=60 K and p_{eff}=3.3. Several studies have been done with the stage-1 compound[63, 64, 65, 66]. They indicated the presence of a transition at T_N=22K, based on the appearance of a remanent magnetization. The results are questionable as to the existence of a second transition. El Hafidi *et al.*[66] found a peak in χ_{dc} at T=17.5±0.5 K with a remanent magnetization that appears above 20 K. They also found p_{eff}=3.7, θ_{CW}=41.5 K and μ=1.53μ_B. Their results, however, were based on powder samples, whereas other results were for HOPG and single-crystal based samples.

Suzuki[67] also found a strong frequency dependence of the susceptibility peak structure in stage-2 $NiCl_2$-GIC, implying a similar ordering as for the stage-2 $CoCl_2$-GIC.

2.5.3 $FeCl_2$-GIC

Much less work has been done with $FeCl_2$-GIC than the other two compounds mentioned. This is because $FeCl_2$ cannot be intercalated directly, but rather $FeCl_2$-GIC is obtained by the thermal decomposition or reduction of $FeCl_3$-GIC[68, 69]. This can obviously lead to questions of sample purity and whether any Fe^{3+} remains in the sample. The presence of Fe^{3+} ions or $FeCl_3$ is important since the in-plane interactions in $FeCl_3$ are antiferromagnetic in contrast to those of $FeCl_2$. The anisotropy

of $FeCl_3$ is of the XY type compared to the Ising type for $FeCl_2$. This adds extra frustration to the system and changes the properties[70].

Karimov *et al.*[71] measured the magnetic susceptibility and saturation of stages-1 and 2 of $FeCl_2$-GIC. For both compounds, they found a peak in the susceptibility at 13 K and θ_{CW}=16.5 K for stage-1 and 16.7 K for stage-2. Magnetization measurements showed a spontaneous magnetization of 30% of the saturation moment after removing the field. The saturation moment was about half of the value from theoretical calculations (equation (1.4)). From the positive value of θ_{CW} and the spontaneous magnetization, they infer that the ordering is ferromagnetic. This may be flawed since θ_{CW} is even more positive for the pristine compound, which is confirmed to undergo antiferromagnetic ordering.

Further studies by Ohhashi and Tsujikawa[68] showed the in-plane structure of $FeCl_2$ is nearly maintained with a repeat distance of I_c=9.51 Å for stage-1 and 12.86 Å for stage-2. Mossbauer measurements showed that there were actually two types of Fe^{2+} sites, one of which corresponds to that found in pristine $FeCl_2$. This type, however is roughly half as populous as the second type of site. They also found θ_{CW}=14±1 K and p_{eff}=5.4±0.1 for both stages. For stage-1, μ was determined to be 2.6μ_B from the saturation magnetization, but no metamagnetic transition was seen. The measurements of susceptibility were made in a field of 6 kOe, roughly the saturation field, so that no determination of the type of low temperature ordering

could reasonably be made.

It is seen that the intercalation of the first two metal chlorides has yielded at least qualitatively similar results. The low temperature ordering of higher stage compounds (n>1) proceeds in two steps with decreasing temperature. The first is a two dimensional ordering within individual domains, the second a three dimensional antiferromagnetic ordering with cluster-glass characteristics. $FeCl_2$-GIC has been studied relatively little, so that it is impossible to determine whether there is, in fact, a two step ordering.

The transition temperatures have been lowered considerably from the Néel temperatures of the pristine chlorides as would be expected. By separating the magnetic layers further with graphite layers, the inter-plane interaction is weakened, making it more difficult to maintain ordering. It has been seen that the interplane interaction is reduced by two to three orders of magnitude by intercalating into graphite[61, 59].

The in-plane characteristics of the intercalant appear to remain nearly the same on intercalation. This was seen structurally by electron microscopy and demonstrated by the fact that the Curie-Weiss temperature, which depends strongly upon the magnetic moment and hence the in-plane structure, remains nearly the same. A comparison of the chlorides and their intercalation compounds is found in table 2.2.

Table 2.2: Comparison of chlorides and their GICs. Where a large range of values has been reported in literature, the range is shown. Where no value for T_{cl} is presented, only one transition was reported.

Chloride	Pristine				GIC					
	I_c (Å)	T_N (K)	θ_{CW} (K)	p_{eff}	Stage	I_c (Å)	T_{cl} (K)	T_{cu} (K)	θ_{CW} (K)	p_{eff}
$CoCl_2$	5.79	25	20	5.2	1	9.38		9.7		
					2	12.70	7.8-8.8	9.1-9.4	31	
					3	16.02	7.7	9.5		
					4	19.68	7.6	8.7		
					5	23.0	7.5	8.8		
$NiCl_2$	5.77	52	68.2	3.3	1	9.36		22	60	3.3
					2	12.78	17-19	20-22	58-70	3.3
$FeCl_2$	5.85	23.5	48	5.4	1	9.51		13	14-17	5.4
					2	12.86		13	14-17	

In the cases of the intercalation compounds, there are ranges of transition temperatures which have been reported. This is partly due to the different properties studied to determine the transition points.

2.6 Metal-Bromide-GICs

Despite the large number of studies that have been conducted on the magnetic metal-chloride GICs, there has been very little done with the bromides. This is because of the greater difficulty in preparing samples.

Balestri *et al.*[72] reported in 1974 their attempts to intercalate many metal-bromides, including $CoBr_2$, into natural graphite flakes and pyrolytic graphite using the two zone method. While they succeeded in a few cases, they found that most could not be intercalated. $CoBr_2$ was among the unsuccessful attempts. Their con-

clusion was that the bromides do not intercalate as readily as the analogous chlorides. They also noted that, in the bromides that they were able to intercalate, the repeat distance, I_c, was smaller than the chloride of the same metal. This is because of the smaller size of the bromides.

In 1977, Stahl[73] was able to intercalate $FeBr_2$ into powdered graphite with limited success. He obtained a stage-5 sample and a mixed stage-1 and 2 sample. The values of I_c were 22.8 Å for stage-5, 13.3 Å for stage-2 and 9.9 Å for stage-1. Although the x-ray diffraction patterns are not presented in graphic form, he did remark that the diffraction peaks at low angle were broad. Only 00ℓ peaks were observed, indicating a lack of in-plane ordering. The breadth of the diffraction peaks and the mixing of stages that was obtained are indicative of the difficulties in obtaining well-staged samples.

In 1977, Stumpp[74] summarized the metal-halide GICs that had been synthesized to that point. He noted relatively few (9) metal-bromides had been intercalated compared to the vast number of chlorides. Neither $CoBr_2$ nor $NiBr_2$ had been intercalated.

In 1989, Stumpp *et al.*[75] reported the synthesis of $NiBr_2$- and $CoBr_2$-GICs by an intercalant exchange method. They first intercalated $CdBr_2$ into natural flake graphite and then replaced the $CdBr_2$ with $NiBr_2$ and $CoBr_2$. This was done by

heating the $CdBr_2$-GIC in the presence of one of the magnetic metal-bromides in an atmosphere of bromine. They were able to obtain stage-3 compounds of each, starting with stage-3 $CdBr_2$-GIC. However, due to the nature of the process, not all of the $CdBr_2$ was displaced, leaving impurities of ~8% in the case of $NiBr_2$-GIC and ~2% in the $CoBr_2$-GIC. X-ray diffraction showed broad peaks in the spectrum of $NiBr_2$-GIC except for the 005 and 0010 peaks, which were much stronger and sharper because of their closeness to the graphite peaks. The values of I_c were determined to be 16.65 Å for $NiBr_2$-GIC and 16.53 Å for $CoBr_2$-GIC.

Kaiser *et al.*[76], in 1994, studied a stage-3 sample of $CoBr_2$ intercalated into flake graphite, which was prepared using the intercalant exchange method described above. They stated that the material is "only obtainable by exchange of $CdBr_2$ with $CoBr_2$". They crushed the flakes into a powder and studied the structural properties by x-ray diffraction. The powder diffraction pattern shows very sharp, intense peaks from the graphite and small, broad intercalant peaks. Although crushing the flakes would have reduced the quality of the sample somewhat, the presence of strong graphite peaks indicates that the intercalation was far from complete, due to the poor quality of the precursor, $CdBr_2$-GIC, which also showed the graphite peak in its diffraction pattern. I_c for the compound was determined to be 16.49 Å. They also found that the intercalant lattice was incommensurate and twisted by 30° with the graphite lattice.

In summary, very few groups have reported any success in intercalating the metal-bromides studied here. None were able to intercalate into HOPG and only minimal structural studies were done on the few samples created. There have been no reports on the magnetic properties of these materials in contrast to the numerous publications on the metal-chloride-GICs.

It was the intent of this study to prepare several stages of each compound in order to compare them to both the pristine bromides and the intercalated chlorides. A variety of stages was planned to determine whether there is a large effect due to the increasing separation between the magnetic layers. First-stage compounds would allow for the best comparison between intercalated and pristine compounds since the interactions should be more similar than in higher stages.

It was expected that some of the same changes that occurred in the chlorides on intercalation would occur in the bromides. For example, one would expect the transition temperature to decrease relative to that in the pristine compound due to a weakening of the inter-plane interaction. A two-stage phase transition was also considered possible since the magnetic interactions in the bromides are similar to those in the chlorides. Because the bromides have lower transition temperatures in pristine form, it was expected that the transitions would occur at lower temperatures than those in the chloride-GICs. Because the bromides have a stronger dependence on second and third neighbours, the existence of more interesting ordering such as

the helical phase in pristine $NiBr_2$ was also considered possible.

Chapter 3
Sample Preparation

3.1 Methods of Intercalation

There are several different techniques that can be used in the intercalation of chemical species into graphite. The method that is used depends upon the species to be intercalated.

The most common technique is the two-zone method. This is essentially a vapour-phase diffusion method. The basic apparatus is a reaction tube with two bulbs or zones. In one of these bulbs is placed the graphite and in the other is the intercalant. The two zones are heated so that a temperature difference between the graphite and the intercalant can be set up. The temperature of the intercalant must be high enough to produce a sufficient vapour pressure of intercalant in the graphite bulb.

The intercalation process can be controlled by modifying the temperatures both with respect to each other and with respect to room temperature. Lower stage samples are produced with smaller temperature differences between the intercalant

and the host. In general, the host is held at a temperature higher than the intercalant to prevent condensation of the intercalant onto the host material.

The staging of the sample can also be controlled by adjusting the length of time over which intercalation is allowed to occur. Finally, one can modify the pressure inside the reaction tube by introducing either an inert atmosphere such as helium or another gas found to aid the intercalation. An example of this is the inclusion of a halogen gas in the intercalation of the metal halides.

Liquid phase intercalation involves immersion of the host material into a melt or a solution of intercalant. Lithium, for example, can be intercalated by immersing graphite into molten lithium. Other materials can be intercalated by first dissolving the material in a solvent, such as CCl_4, $SOCl_2$ or acetone. Intercalation from solution can be convenient, but it is more difficult to produce well-staged samples using this method.

The final method, and the one used for this study, is the solid phase technique. This is similar to the two-zone vapour technique, except that the host and intercalant are contained within the same zone. The intercalation is controlled by the temperature of the reaction tube, the pressure of gas inside the tube and the length of time of the intercalation. While this technique does not allow for a temperature difference between the host and intercalant, it does not rely so heavily on a high in-

tercalant vapour pressure. This, in fact, is a key reason for the success of this method in preparing the materials studied here.

Other factors which play a role in the intercalation process are the size, shape and type of host. For example, larger samples are more difficult to intercalate than small, thin samples. Also, powder graphite is much easier to intercalate than single crystals because of its larger surface area.

3.2 Sample Preparation

The samples used in this study are made by intercalation of $FeBr_2$, $CoBr_2$ and $NiBr_2$ into HOPG. Pieces of the host material, HOPG, are cut from a larger slab by using a sharp scalpel. The edges are smoothed and damaged surface layers are peeled off by using transparent tape. The pieces are cleaned ultrasonically in an acetone bath then dried and heated under vacuum to remove any contaminants. The size of the sample is limited by the inner diameter of the sample tube. The tube is made from 1/4 inch diameter Pyrex tubing with a one inch diameter bulb at the bottom. Other considerations are also included in the sample size such as the ease of intercalation and the size required for various experiments. For example, heat capacity measurements require thin samples, which have uniform thermal conductivity, whereas magnetization measurements require larger samples to obtain a large enough magnetic signal.

Sample preparation begins in a dry box with a positive pressure of Ar gas. Three or four HOPG pieces are placed in a reaction tube with an excess of intercalant powder such that the HOPG is completely covered by the powder. The tube is then capped with a stopcock to allow for transferal from the dry box without moisture contamination. Once out of the dry box, the tube is attached to a specially designed vacuum line and evacuated to <5 mtorr. The vacuum line has four 1/4 inch ports, each of which has a stopcock so that each port can be closed. Three of the four ports are used for sample tubes and the fourth for bromine gas. Another port is connected to a mercury manometer to measure the pressure inside the line. Finally, the pumping port, attached to a rotary pump also contains a stopcock so that the port can be closed, isolating the line from the pump. A cold trap between the line and the vacuum pump allows for a lower base pressure and protects the pump from the chemicals introduced into the line.

Once the pressure in the line reaches the base pressure of the system, the pumping port is closed. The bromine port is opened and the line is back-filled with bromine gas to a predetermined pressure(typically 2 cm Hg). The bromine port is then closed and the sample tube is immersed in liquid nitrogen. This condenses the bromine from the line into the sample tube. Once the bromine is condensed, the pumping port is opened to remove any excess gas and the tube is sealed using a propane-oxygen torch. The sample tube is inspected to ensure that there is a good

seal and that the host material is embedded in the intercalant powder. If the host material is not completely covered by the intercalant, the intercalation will not be as complete. The samples are then placed in a small box furnace for intercalation. The furnaces are controlled by P.I.D. controllers and can be regulated to $\pm 1^{o}$C. Up to three furnaces were in use at any one time.

After the intercalation period, the samples are removed from the reaction tube and cleaned with acetone and the surface layers are peeled off to remove any intercalant powder adhering to the surface. The cleaned samples are then analyzed to determine staging and purity.

Initially, a reaction temperature of 500^{o}C was used, based on temperatures used in other authors' attempts to intercalate bromides and chlorides. This was also the limit set by the fact that Pyrex begins to soften at 512^{o}C. In order to go to higher temperatures, sample tubes would need to be made of quartz, which is somewhat more expensive and more difficult to work with. It was found that many of the early samples were exfoliated during the intercalation process. Badly exfoliated samples are not useful in experiments, so the temperature was reduced in an attempt to minimize exfoliation. The reduced temperature resulted in longer intercalation times to achieve the same stage of intercalation. It also means that there was a reduced likelihood of achieving stage-1 compounds.

Since exfoliation was still occurring, the furnaces were set so that the temperature increased slowly to the set point, over a period of five to seven days. This, again, increased the total time taken for intercalation, but drastically reduced the amount of exfoliation. When the samples were cooled, the temperature was also allowed to decrease slowly.

The time used for intercalation was determined by trial and error. Reproduction of the pressure, temperature and time conditions, unfortunately, does not guarantee identical results. There is a strong dependence on the size of the pieces of the host material and the degree to which it is embedded in the intercalant powder. For this reason, many of the samples that were produced were unsuitable either due to lack of intercalation or mixing of stages.

An x-ray diffractogram from stage-2 $CoBr_2$-GIC is shown in figure 3.1, and one from a mixed-stage 2 and 3 sample is shown in figure 3.2 for comparison. Note that, while the peaks from the stage-2 sample are also seen in the mixed-stage sample, an extra set of peaks from the stage-3 regions is present.

From the many attempts, the following high quality samples were produced for this study. With HOPG host material, stages 1 and 2 $CoBr_2$-GIC were prepared as well as stage-2 $FeBr_2$-GIC and stages 2, 3 and 5 $NiBr_2$-GIC. A sample of stage-3 $CoBr_2$-GIC based on single-crystal natural graphite was also prepared.

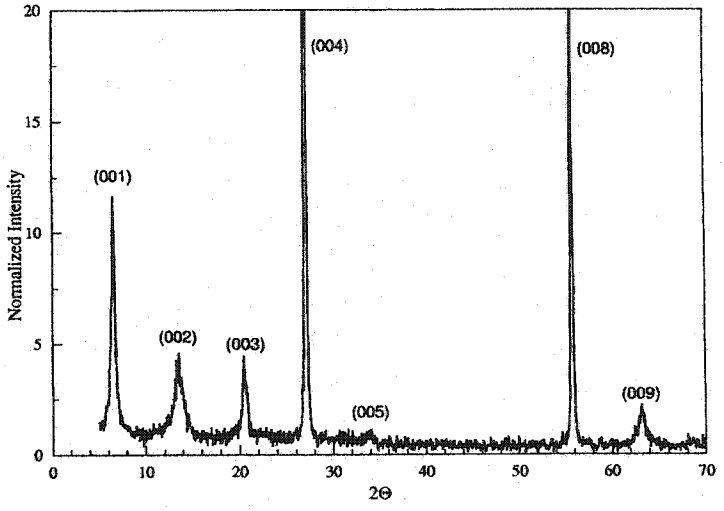

Figure 3.1: 00ℓ diffractogram of stage-2 $CoBr_2$-GIC sample.

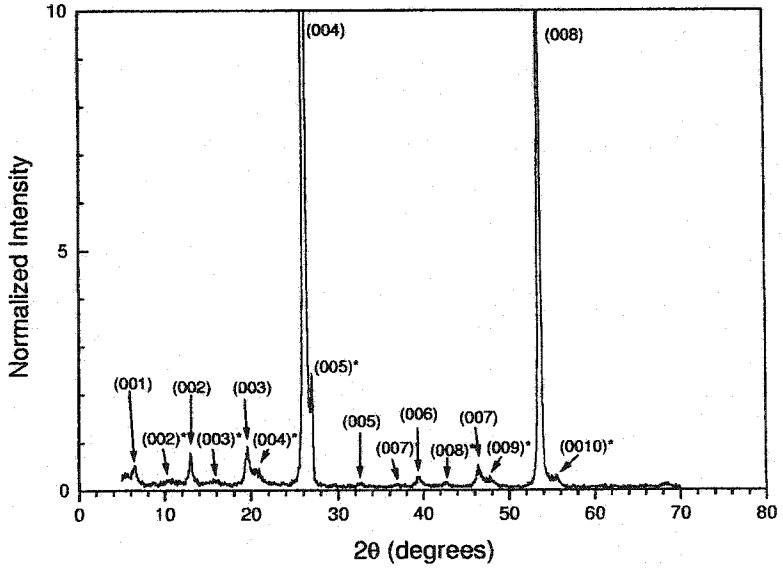

Figure 3.2: 00ℓ diffractogram of mixed-stage sample. The sample is a mixture of stage-2 and stage-3 $CoBr_2$-GIC. Peaks due to stage-3 are marked with *.

Table 3.1: A summary of the conditions used for GICs prepared. The repeat distance determined using x-ray diffraction is compared to the theoretical one.

Intercalant	Stage	Temperature (°C)	Time (wks.)	I_c (Å)	$(n-1)c_{gr}+c_{int}$ (Å)
$CoBr_2$	1	450	16	10.37±0.01	9.47
	2	400	9	13.74±0.02	12.82
	3*	400	8	16.99±0.04	16.17
$NiBr_2$	2	375	14	13.28±0.07	12.78
	3	500	4	16.97±0.03	16.13
	5	350	7	23.74±0.02	22.83
$FeBr_2$	2	500	40	13.14±0.03	12.92

*Single-crystal sample used in neutron scattering experiment.

Table 3.1 specifies the intercalation conditions for the samples used in this study. It should be stressed that these conditions are not necessarily the only set of conditions that can be used to obtain these samples. Rather, one should notice the trends that reduced stages are obtained by increasing the temperature and length of time for intercalation. The last two columns in the table are the measured and theoretical values for the intercalant repeat distance. The theoretical estimate is determined by adding the c-spacings of the carbon layers and the intercalant layers.

Attempts were made to create other stages of the compounds, in particular, stage-1 compounds, but were not successful. Reaction times as long as ten months were used, but the resulting compounds were, for the most part unsuitable for use. This emphasizes the difficulty in preparing these materials.

A mass uptake measurement was performed on the single crystal sample used

for neutron scattering. The initial mass of the crystal was 1.2±0.1 mg and the final mass was 2.0±0.1 mg. Thus, the mass uptake was 0.8±0.1 mg $CoBr_2$. This translates to $2.2\pm0.3\times10^{18}$ $CoBr_2$ molecules and $6.0\pm0.5\times10^{19}$ C atoms. This is a C:$CoBr_2$ ratio of 27±6. If we divide the in-plane area taken up by the unit cell of $CoBr_2$ by the area taken up by the carbon atom (1/2 unit cell), we get an approximate minimum ratio (maximum packing) of 10.8 C per $CoBr_2$. This gives a filling factor of 40%. Typical metal halide filling factors can be as high as 60-80%[77]. Analyses using both x-ray and neutron diffraction show that the staging fidelity of this sample was quite good.

It was not practical to perform similar measurements for all samples. Because three or four pieces were used in each reaction tube and all of the pieces were of roughly the same size and shape, they would not be distinguished easily after intercalation. This means that in order to be sure of the mass uptake, only one piece of HOPG can be intercalated in each tube. Since good samples are quite difficult to make, it was not practical to use fewer pieces because the preparations took a long time and were not always successful.

3.3 Sample Analysis

After intercalation, the samples are characterized by using a θ-2θ x-ray diffractometer, operated by Mr. W. Gong, to obtain a 00ℓ diffractogram. The 00ℓ diffraction shows the staging purity of the sample and can be used to measure the repeat dis-

tance, I_c. Staging impurities result in one of two effects noticeable in the diffraction pattern. If there is an admixture of two or three stages in the sample, the diffraction pattern shows satellite peaks corresponding to each of the stages. A broadening of the diffraction peaks at larger angles implies that there is an average over a distribution of stages present.

A sample diffractogram for $FeBr_2$-GIC is shown in figure 3.3 with the Miller indices for a stage-2 compound. The intensity pattern of the peaks is enveloped by the structure factor for graphite. Peaks in the GIC diffraction pattern which lie closer to graphite peaks are stronger than those that are further away. For this reason, the strongest peak in the GIC pattern will be the one closest to $\ell = n+(c_{int}/c_{gr})$, where c_{int} is the intercalant c-spacing and c_{gr} is the graphite c-spacing, 3.35 Å. For near-integer values of (c_{int}/c_{gr}), the intensity of the peaks drops sharply away from the graphite peaks. For the bromides studied here, (c_{int}/c_{gr}) is very nearly two. Therefore, the most intense peak is ℓ=n+2 and the intensity drops very quickly on either side of this peak.

Using this information, the diffraction peaks in figure 3.3 are easily indexed. The interplane distance associated with each peak is calculated from Bragg's equation, $\lambda=2d_\ell \sin\theta$. In a plot of ℓ *vs* $1/d_\ell$, the repeat distance, I_c is equal to the slope. This plot is shown in figure 3.4 for the peaks in figure 3.3. The values obtained in this fashion are shown for each compound in table 3.1.

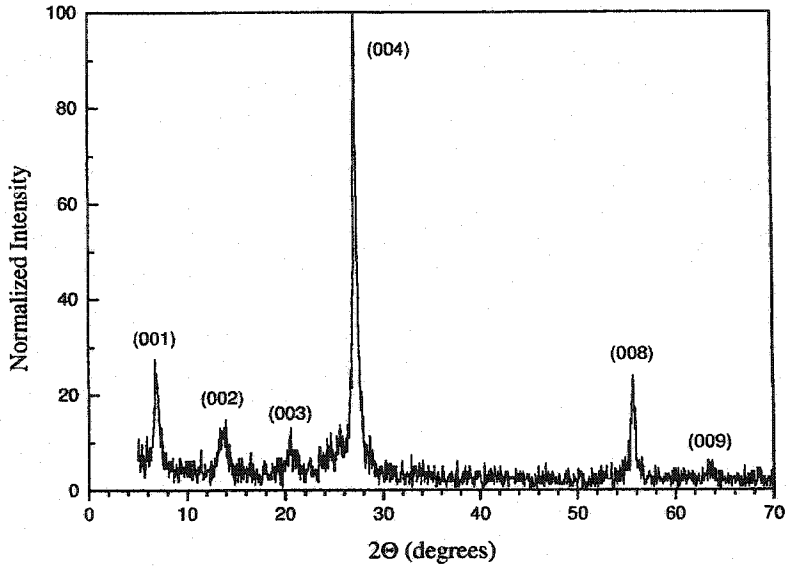

Figure 3.3: 00ℓ x-ray diffractogram of stage-2 $FeBr_2$ sample

Figure 3.5 shows the plot of ℓ *vs* $1/d_\ell$ for the mixed stage sample whose x-ray pattern is seen in figure 3.2. The plot clearly shows the presence of two distinct stages. While I_c can be determined for each stage from this plot, the results are considered unreliable since the presence of multiple stages changes the lattice strains compared to a well-staged sample. This results in small changes in the lattice parameter for both stages. The best fit line for the weaker stage 3 peaks shows deviations due to larger uncertainties in peak locations.

Domains were observed in our samples by using scanning electron microscopy as shown in figure 3.6. The sample was prepared by peeling away the top layer just prior to putting the sample in the microscope. By peeling off the top layer, we can

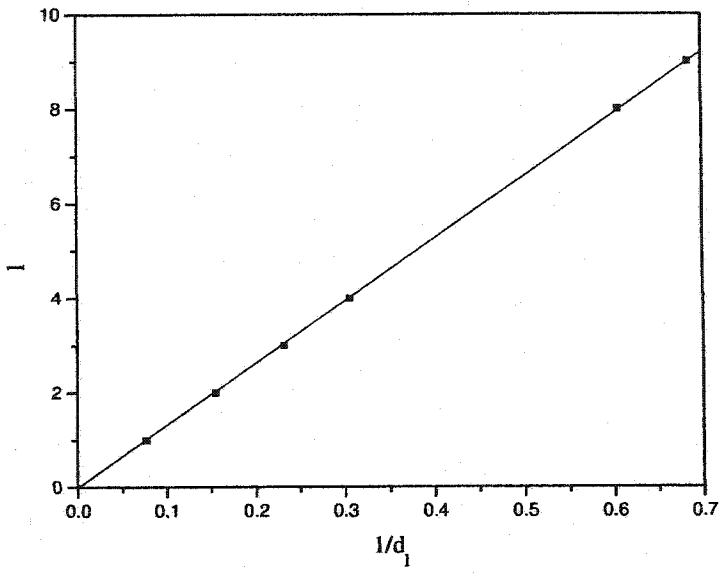

Figure 3.4: Determination of I_c for stage-2 $FeBr_2$ sample.

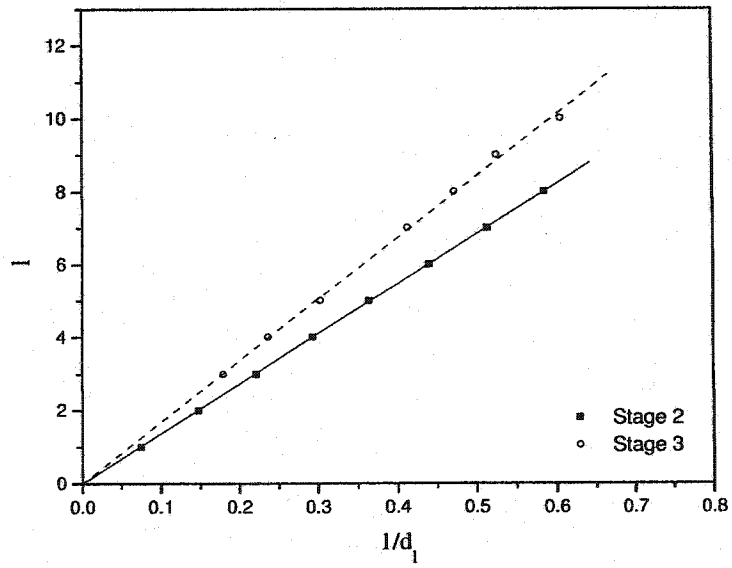

Figure 3.5: Determination of I_c for mixed-stage sample.

expect that roughly half of the exposed intercalant domains will remain attached to the removed layer. Further material will be removed in handling the sample. Finally, only the domains with intercalant above the new top graphite layer will be seen by the SEM. Domains with intercalant lying below this layer are not seen. This reduces the number of domains visible in the SEM by a further 1/2, meaning that fewer than 1/4 of the domains should be seen in the SEM picture. As such, this is seen as a technique to see domain size only and not intercalant packing density. The light spots in figure 3.6 are the domains in which the intercalant is at the surface of the sample. The domain size is near the resolution limit of the SEM, but the maximum domain size is estimated to be 40 nm. This is in reasonable agreement with other observations of domains in intercalated compounds.

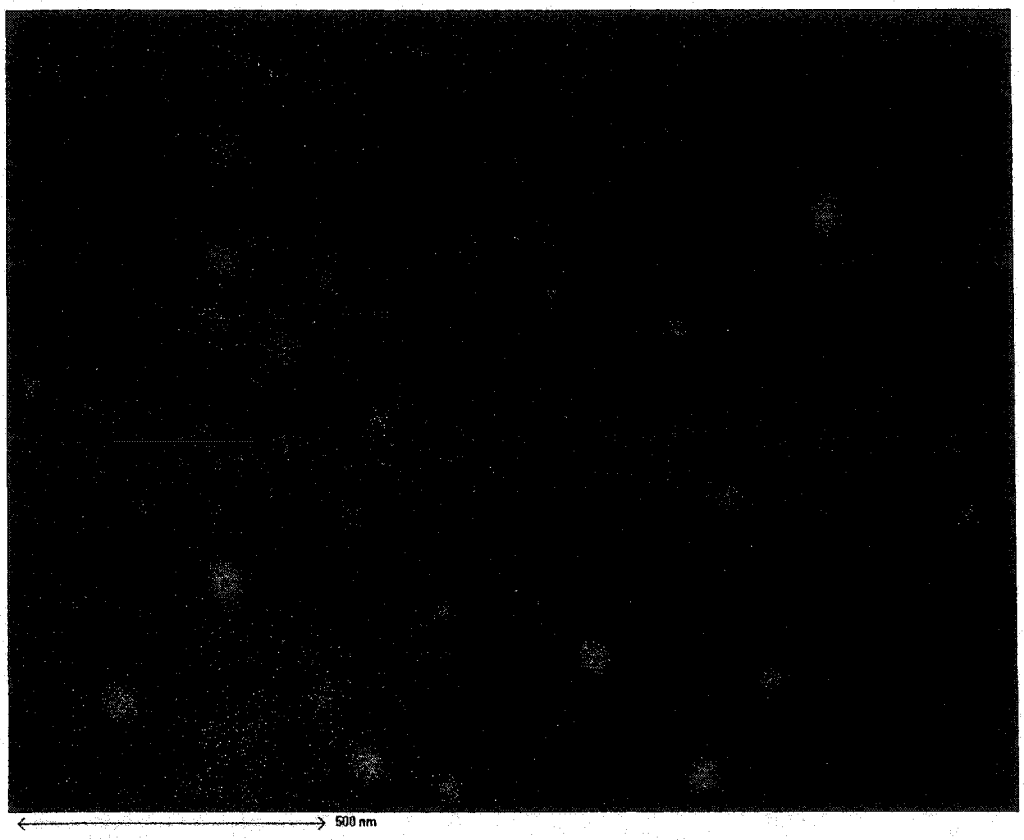

Figure 3.6: SEM image of $CoBr_2$-GIC surface. Light spots are intercalant domains at the surface.

Chapter 4
Experimental Techniques

The magnetic properties of the GICs were measured by using three techniques: dc magnetization, ac susceptibility and heat capacity. This chapter describes the techniques and equipment used to make these measurements.

4.1 dc Magnetization

DC magnetization experiments were performed with a Quantum Design MPMS SQUID Magnetometer[78]. It is comprised of components for temperature control, gas handling, liquid helium, sample handling, the SQUID detector and the superconducting magnet, all of which are computer controlled.

Figure 4.1 shows the temperature control system for the MPMS. The sample chamber is surrounded by a cooling annulus, insulated from the surrounding liquid helium bath by a vacuum jacket. Liquid or gaseous helium enters the cooling annulus via the impedance assembly at the bottom of the annulus.

The system is cooled by drawing cold gas into the cooling annulus from the

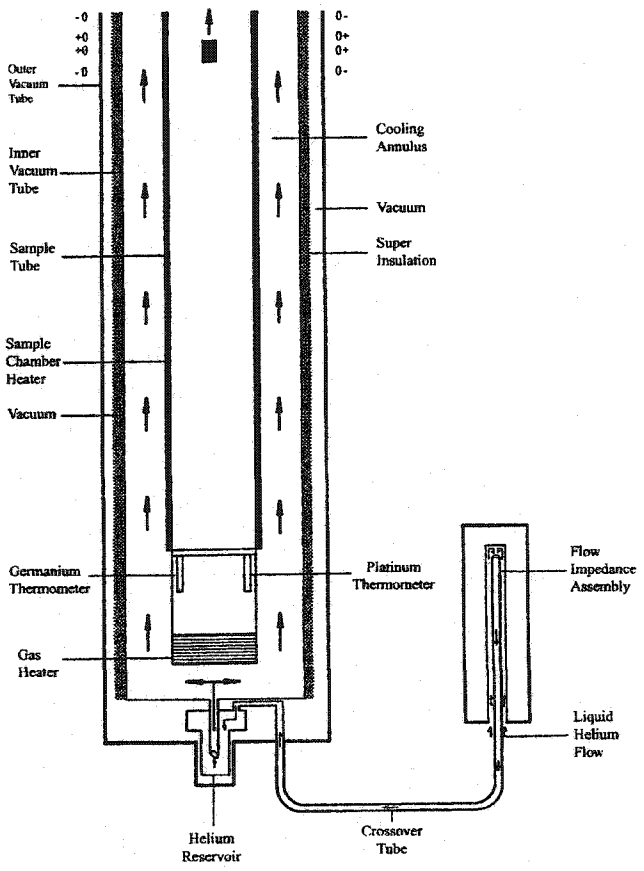

Figure 4.1: Cooling system diagram for Quantum Design MPMS. From ref. [78].

helium bath. The sample chamber can be heated using the chamber heater or the gas heater. When a new temperature is set, the system uses high-power heating or cooling until the temperature nears the set point, at which point the temperature is stabilized. High-power heating is accomplished by using the chamber heater, which heats the chamber at a rate of approximately 10 K per minute. Fast cooling is done by drawing cold helium gas through the cooling annulus at a high rate that can exceed 20 K per minute.

The gas flow into and out of the cooling annulus is controlled by the impedance assembly and by pumping gas out of the annulus through a series of control valves (see figure 4.2). Heating the impedance restricts the flow of helium into the cooling annulus. When the impedance heater is off, helium may flow into the annulus freely. For normal cooling, the impedance heater is set on low to restrict the flow of gas into the annulus. When the impedance heater is on high, helium cannot flow into the annulus. Fine control of the cooling rate is done with the cooling valve. As this valve is opened, cold helium gas flows more quickly through the annulus, increasing the cooling power.

Temperature stability is maintained by using the gas heater to warm the incoming helium gas to the sample temperature. The temperature can be slowly raised or lowered by changing the temperature of the gas flowing through the annulus.

To reach temperatures below the predefined crossover temperature, 4.4 K, the

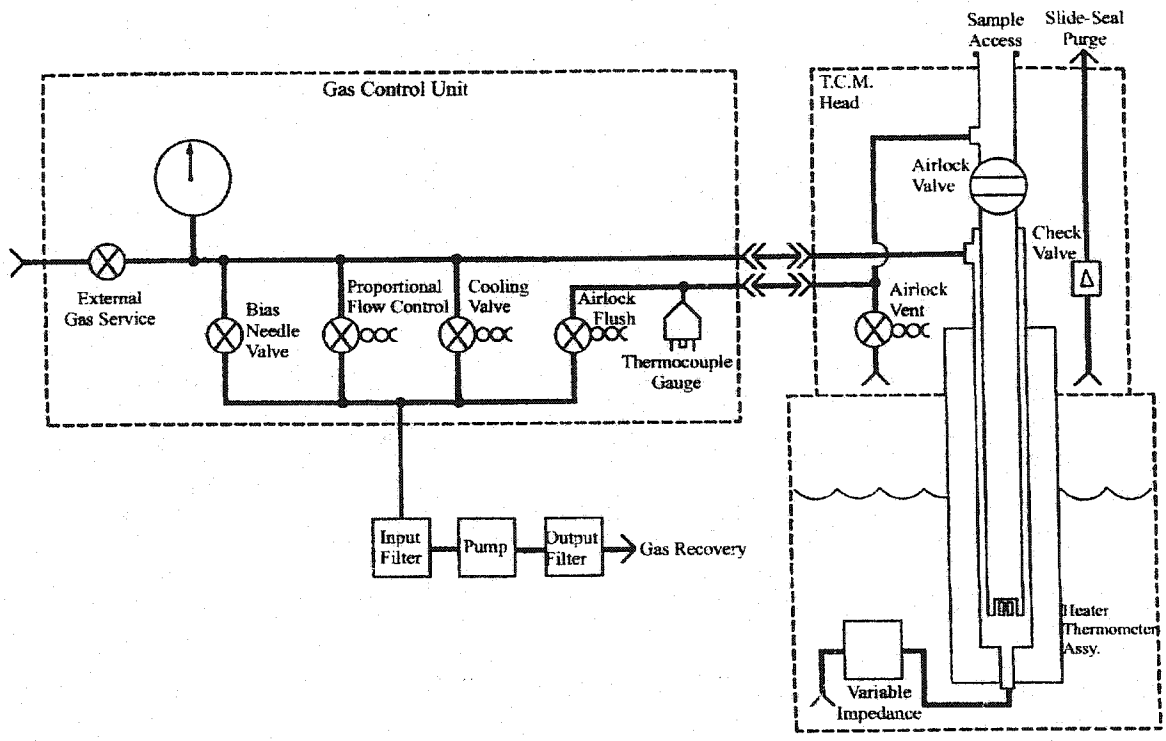

Figure 4.2: Gas flow control for Quantum Design MPMS. From ref. [78].

annulus is filled with liquid helium. The heaters are turned off and the proportional valve is opened to allow liquid to flow into the reservoir. After a predefined time, sufficient to nearly fill the annulus, the impedance heater is turned on, closing the impedance and preventing more liquid from flowing in. The temperature is then controlled by adjusting the pumping rate via the proportional valve. Pumping on the helium in the annulus reduces the vapour pressure above the liquid and decreasing its temperature. The temperature remains below the crossover point until the helium in the annulus is spent, at which point the annulus is re-filled.

When heating through the crossover temperature, there is a delay during which the excess helium in the annulus is boiled off by the heater. When the liquid is gone, there is typically an overshoot in the temperature and the system must recover temperature stability. This overshoot can raise the temperature to as much as 10 K, depending on the amount of liquid boiled off and the heater power used to do this. This overshoot can cause a discontinuity in data if the sample has a history dependence.

The temperature is sensed with two different thermometers. For temperatures below 40 K, a germanium resistance thermometer is used. Its exponential dependence of resistance upon temperature gives it high sensitivity to temperature changes at lower temperature. Above 40 K, a platinum resistance thermometer is used. It has a useful range that goes well above room temperature.

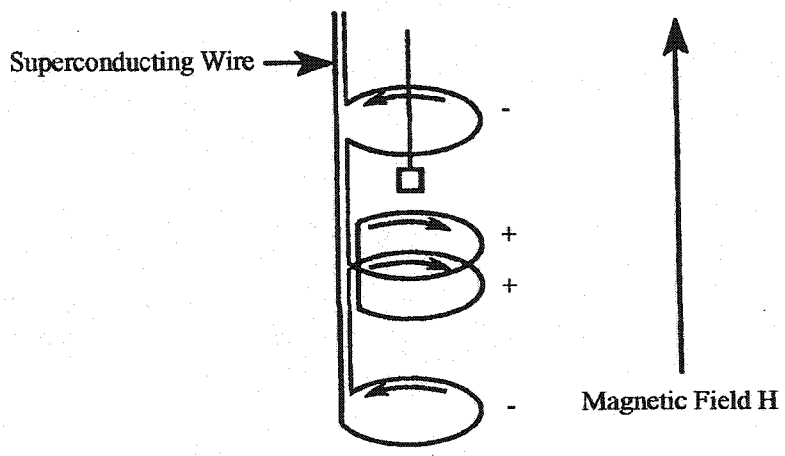

Figure 4.3: Second derivative coil design for Quantum Design MPMS. From ref. [78].

The detection system uses a second derivative coil configuration (see figure 4.3) consisting of four equal-sized coils. The total length of the coils is 3 cm, with the upper and lower coils wound in the direction opposite to that of the central coils. This configuration strongly rejects interference caused by nearby magnetic sources. The sample is mounted on a long, thin quartz rod, providing a small but constant background.

The sample is positioned at the bottom of the travel region, just out of the sensing range of the coils (figure 4.4). The sample is then brought upwards through the coils, inducing a current as the flux changes. The induced current is measured at several (32) points along the length of travel (6cm). Because the central coils are wound counter to the outer coils, the resulting signal consists of a central peak larger in magnitude and opposite in sign to the two outer lobes. Multiple (3) scans are aver-

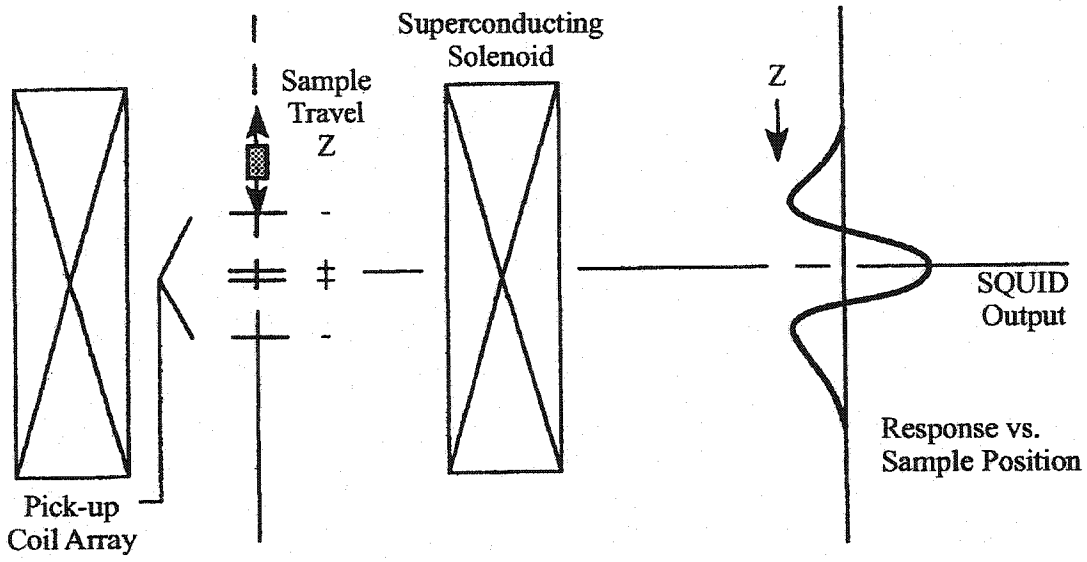

Figure 4.4: SQUID response to dipole sample moving through detection coils. From ref. [78].

aged and a response curve is fit using either an iterative or linear regression method. The resulting fit is compared to a point source calibration curve to determine the magnetic moment of the sample. The mass magnetization (cgs) is calculated by dividing the moment by the sample mass in g. This is converted to SI units ($A \cdot m^2/kg$) by multiplying by $4\pi/1000$. The static or dc susceptibility, χ_{dc} is calculated by dividing by the applied field.

The signal from the coils is coupled to the SQUID sensor through a superconducting transformer with an RFI shield. The shield has a -3 dB rolloff frequency of about 20 kHz, which allows operation in a noisy RFI environment without flux jumps. During a field change, the transformer is heated into a normal state, which

eliminates persistent currents in the SQUID input circuit. This ensures that there is no offset in the SQUID signal caused by the changing field.

The magnetic field is supplied by trapping a persistent current inside a superconducting magnet immersed in the helium bath. The magnet is capable of supplying ± 5.5 T with a maximum resolution of 0.1 Gauss. Trapped flux in the magnet can be accounted for by using a lead sphere as a calibration sample. Below its transition temperature of 7.2 K, the sample acts as a perfect diamagnet for small fields. By ramping the field from negative to positive, the magnetization of the sample will go from positive to negative, with the zero magnetization point showing the zero applied field position. Any difference between this and the zero current condition for the magnet is due to trapped flux and can be accounted for by adding the appropriate offset to the field.

It should be noted that, late in the period of this study, the MPMS apparatus was upgraded with a reciprocating sample option (RSO) and a new cooling system. The RSO allows for the sample to be moved continuously up and down through the detection coils, with the signal being sampled at many places along the path. This gives more precise values, allowing for measurements one to two orders of magnitude lower than previously possible with this equipment. The new cooling system allows for continuous measurement at 2 K without having to refill the cooling annulus. This also eliminates the delay at the crossover temperature.

4.2 MagLab EXA

Both the ac susceptibility and specific heat measurements were done with the Oxford Instruments MagLab EXA[79]. This system is capable of measuring magnetic and transport properties as well as specific heat using of removable measurement probes.

The cooling system for the MagLab consists of an outer liquid nitrogen jacket, a liquid helium reservoir and a variable temperature insert (VTI). At the centre of the VTI is the sample space, into which measurement probes are inserted. The sample space can be evacuated to a low pressure of helium exchange gas. Cooling is done by pumping on the VTI through a needle valve. This brings cold helium gas from the reservoir through the VTI. Cooling below liquid helium temperature is accomplished by allowing liquid helium to flow into the VTI and pumping through the needle valve to reduce the vapour pressure above the liquid. The sample space is warmed by using a heater in the VTI. By adjusting the heater and the needle valve, the temperature is controlled from a base temperature of 1.7 K up to 400 K.

VTI Temperature is measured with a Cernox thermometer. The Cernox is a thin film metal-oxide resistor deposited on a sapphire substrate. The resistance of the film is extremely sensitive to temperature at low temperatures and relatively insen-

sitive to magnetic field, enabling accurate temperature measurement well below the base temperature of the system. The thermometer is calibrated for measurements up to 400 K, making it useful for the entire temperature range available to the system. A second thermometer is located in each of the measurement probes for accurate measurement of the sample temperature.

The magnetic field is produced with a superconducting magnet located in the helium reservoir. The magnet is capable of reaching ± 9 T and can be used either in the persistent or non-persistent mode. The magnet system consists of a power supply, a superconducting coil and a superconducting switch. When the switch is in a superconducting state, the coil becomes a closed superconducting loop such that electrical currents may neither enter nor exit. When the heater is in a normal state, it becomes resistive and the coil may be charged or discharged as needed. To create a magnetic field, the switch heater is turned on, and the power supply ramped to the necessary level. In persistent mode, a current is established within the superconducting coil producing a magnetic field. When the desired field is reached, the switch heater is turned off, allowing a persistent current to flow within the coil. The voltage across the leads is then reduced to zero and no further power is supplied to the magnet. In the non-persistent mode, the switch heater is left on and power is continuously supplied to the magnet. The persistent mode is useful in applications where the field remains constant for extended periods of time, whereas the non-persistent mode is more useful when the field is ramped.

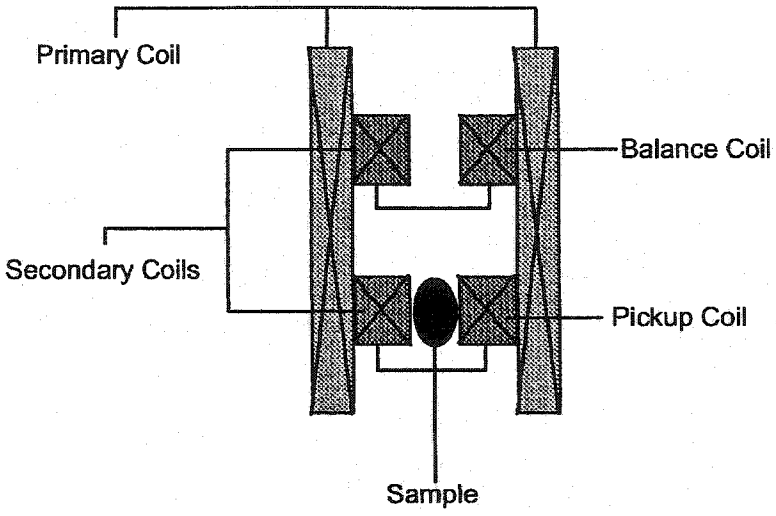

Figure 4.5: Coil configuration for ac Susceptibility measurements. From ref. [79].

4.3 ac Susceptibility

Ac susceptibility measurements use a conventional method and provides a direct measurement of $\chi_{ac} = \frac{dM}{dH}$. The Magnetic Properties Probe (MPP) consists of a primary coil outside of a double secondary coil system (see figure 4.5). The secondary coils are identical, displaced vertically from each other. When an ac current is passed through the primary coil, a sinusoidally varying field is produced inside. This induces an ac current in the secondary coils. Since the coils are identical, the currents produced are identical and, when subtracted one from the other, exactly balance.

If a sample is positioned inside one of the secondary coils, the inductance of the coil is changed due to the magnetic properties of the sample. This changes the

impedance of the coil so that the induced voltage in the coils is no longer balanced. The resultant voltage difference is related directly to the ac susceptibility of the sample. The signal from the coils is processed through a lock-in amplifier, which detects at the frequency of the primary coil input (or higher harmonics if desired). Real and imaginary components of the susceptibility can be detected as the in-phase and out-of-phase components of the detected signal respectively. In order to exclude extraneous signals due to an imbalance in the secondary coils, a double-point measurement can be taken. The signal is measured with the sample in the upper and lower coils in turn. Any coil imbalance cancels out when the two responses are averaged.

4.4 Heat Capacity

Heat capacity measurements were done with the MagLab EXA using the Heat Capacity Relaxation (HCR) probe. The system uses a relaxation method to determine the heat capacity of small samples.

The measurement chip, shown in figure 4.6, located on the probe head is a sapphire substrate with a metallic heater deposited on the front surface. Attached to the chip via four 50μm gold leads is a Cernox thermometer. The chip is suspended by four 20μm gold plated tungsten leads, which give electrical contact to the probe head with a very weak thermal link. The thermal link between the chip and the thermometer is large compared to that with the probe head so that the thermal response of the

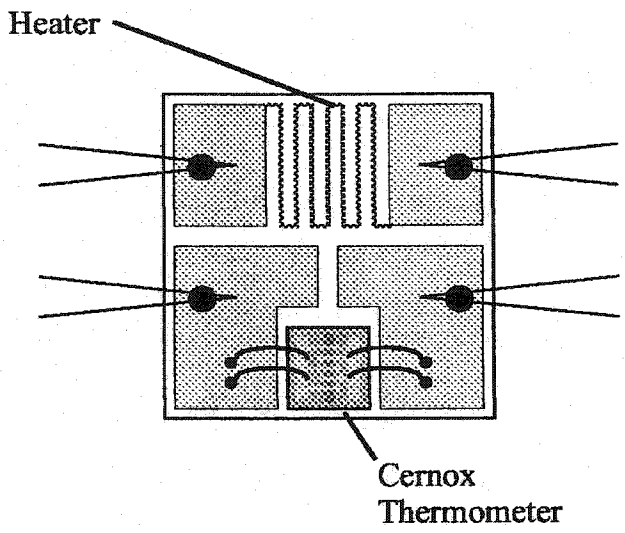

Figure 4.6: Heat capacity sample platform. From ref. [79].

thermometer is relatively fast. This means that the chip-thermometer assembly can be treated as a single thermal unit.

To measure the heat capacity, a step-wise change in power is supplied to the platform, creating a new equilibrium temperature. The platform temperature decays exponentially to this temperature according to

$$T = T_1 + \Delta T_0(1 - e^{-1/\tau})$$

where T_1 is the initial temperature and ΔT_0 is the equilibrium temperature change. The time constant, $\tau = R_{TH}C$ is the product of the heat capacity of the sample plus platform and the effective thermal resistance between the sample and surroundings, $R_{TH} = \frac{\Delta T_0}{\Delta P}$. The heat capacity of the sample is then calculated using $C = \frac{\tau}{R_{TH}}$.

The sample is mounted on the back of the chip, opposite the heater. It is

held in place by a small amount of Wakefield thermal compound, the mass of which is measured and whose thermal properties are calibrated. This compound provides good thermal contact between the chip and the sample. Care is taken to ensure that the surface of the sample is flat and the layer of thermal compound is thin and evenly distributed. The amount of thermal compound is typically less than one percent of the sample mass.

Once the sample is mounted, the HCR probe is inserted into a stainless steel shroud. The shroud is then evacuated to $\sim 10^{-5}$ torr before being inserted into the VTI. The temperature of the VTI must be stabilized at a temperature at least 0.5 K below the lowest desired measurement temperature. The temperature of the chip is controlled by the heater on the chip. This gives a practical limit to the maximum chip temperature for a given VTI temperature. For the present work, the VTI was set to 1.8 K, allowing for measurements down to $\sim$2.5 K.

Chapter 5
Experimental Results

This chapter summarizes the experimental results obtained from the equipment described in the previous chapter. Zero field cooled and field cooled results for dc susceptibility are obtained by cooling the sample in zero field, turning the field on, taking measurements with increasing temperature and then again with decreasing temperature. All ac susceptibility measurements, unless otherwise noted, are performed at a frequency of 500 Hz with an amplitude of 1 Oe.

All results have been corrected for the demagnetizing factor from the sample geometry. This was done, following the method used by Elahy and Dresselhaus[56], by approximating the samples as ellipsoids with axial dimensions the same as the sample dimensions. The demagnetizing factor for each sample was then determined using the results of Osborn[80].

The values plotted in all figures are in SI units, but several references are made in Gaussian units (i.e., Oe). This is because the equipment predominantly uses Gaussian units. The MPMS operating system is entirely in Gaussian units and the parameters for ac field on the MagLab EXA are also in Gaussian units. While con-

version to SI units was done before the data was analyzed, some field strengths are still reported in Oersteds for convenience.

The magnetization and susceptibility reported are the mass magnetization and mass susceptibility, with units $A\cdot$ m^2/kg (=emu/g) and m^3/kg (=1000/4π emu/g), respectively. The applied magnetic field is shown in the SI unit of A/m. It is perhaps more commmon, although less correct, to use units of Tesla, the unit for induction. The conversion is 1 T = $\frac{10^7}{4\pi}$ A/m.

5.1 $CoBr_2$

Figure 5.1 shows the low temperature dc susceptibility for stage-1 $CoBr_2$-GIC. There is no transition down to 2 K. There is also no effect of field on the susceptibility in this region. This is what is expected for a paramagnetic sample. Since the magnetization varies linearly with field, the susceptibility does not change with field.

Figure 5.2 shows the low temperature dc susceptibility with an in-plane applied field of 20 Oe. While there is no clear transition, there is a slight difference between the zero-field cooled(ZFC) and the field-cooled(FC) data. The FC data has a slightly higher susceptibility below T$\approx$9.5 K. The larger difference below 4.4 K is systematic. This is caused by warming the sample through the crossover point as discussed in Section 4.1. This is indicative of a slight history dependence in the material.

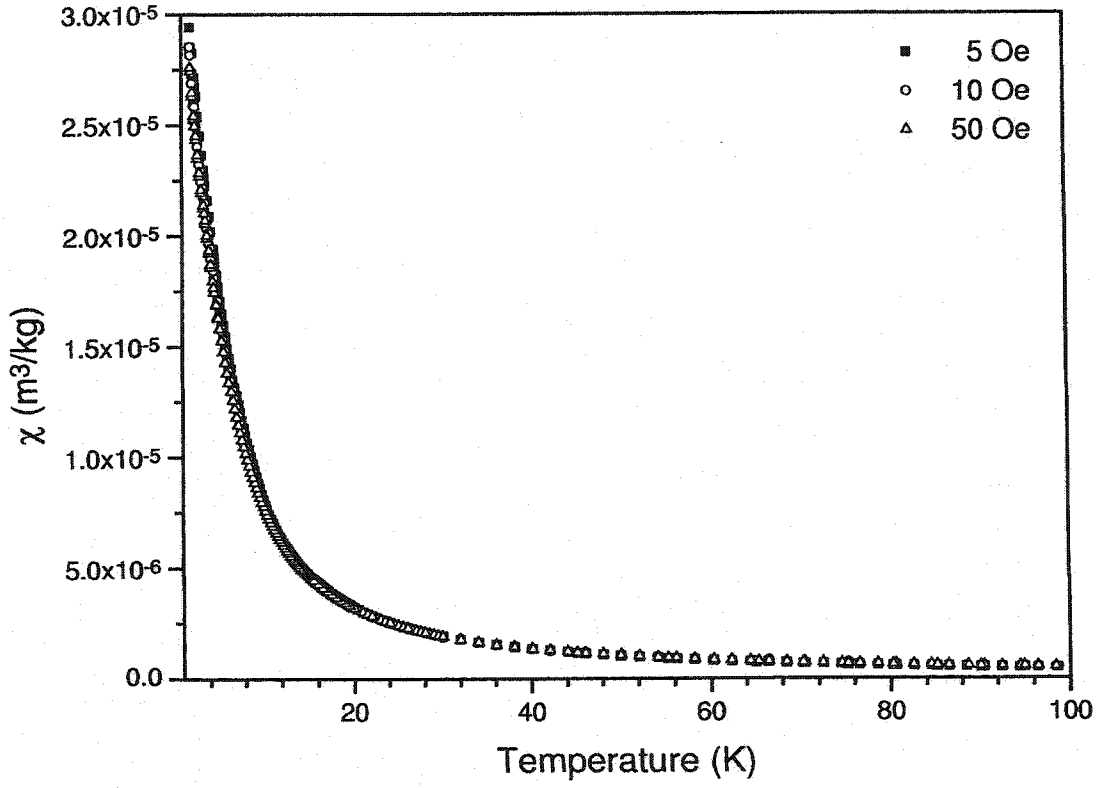

Figure 5.1: Low temperature dc susceptibility data for stage-1 $CoBr_2$-GIC with various applied in-plane fields.

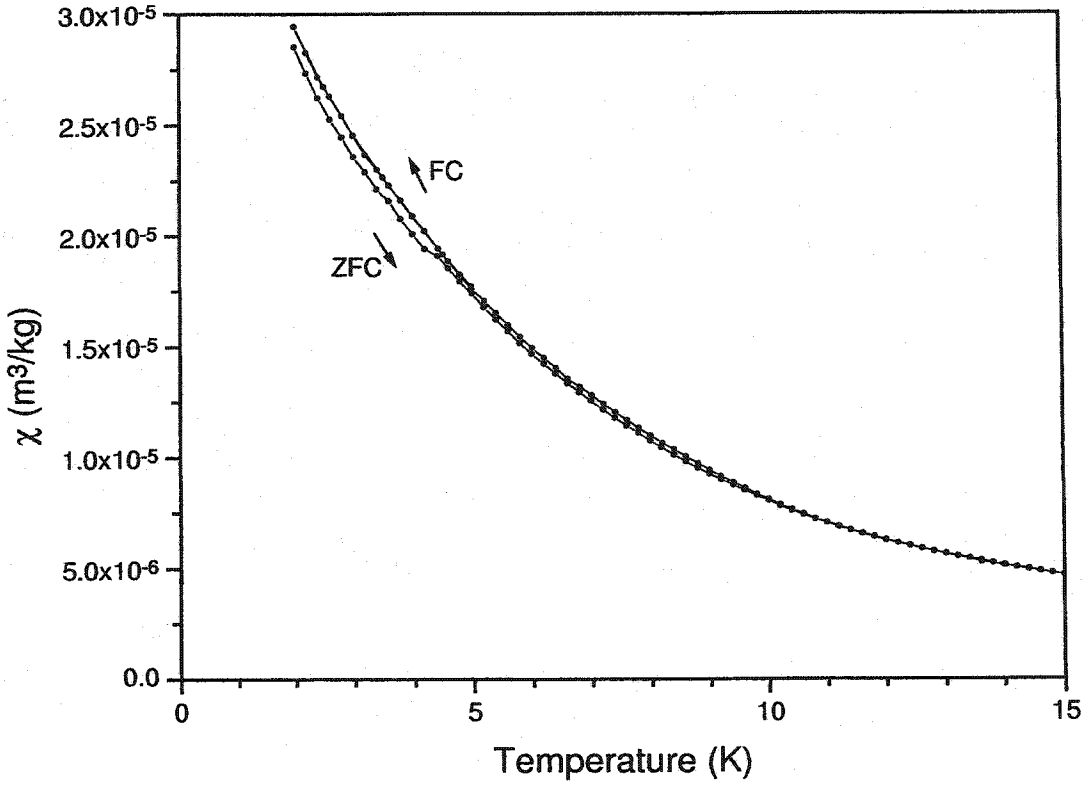

Figure 5.2: Low temperature dc susceptibility data for stage-1 $CoBr_2$-GIC showing ZFC and FC data. H = 20 Oe in-plane.

Figure 5.3 shows the dc magnetic susceptibility of stage-1 $CoBr_2$-GIC in the high temperature region for applied fields both in-plane and along the c-axis. The c-axis measurement appears to be flattening out near room temperature.

The magnetization *vs* field for stage-1 $CoBr_2$-GIC for in-plane and c-axis measurements at T=2 K are shown in figure 5.4. The in-plane magnetization does not saturate to a constant value, but rather to a smaller, constant slope. The positive slope

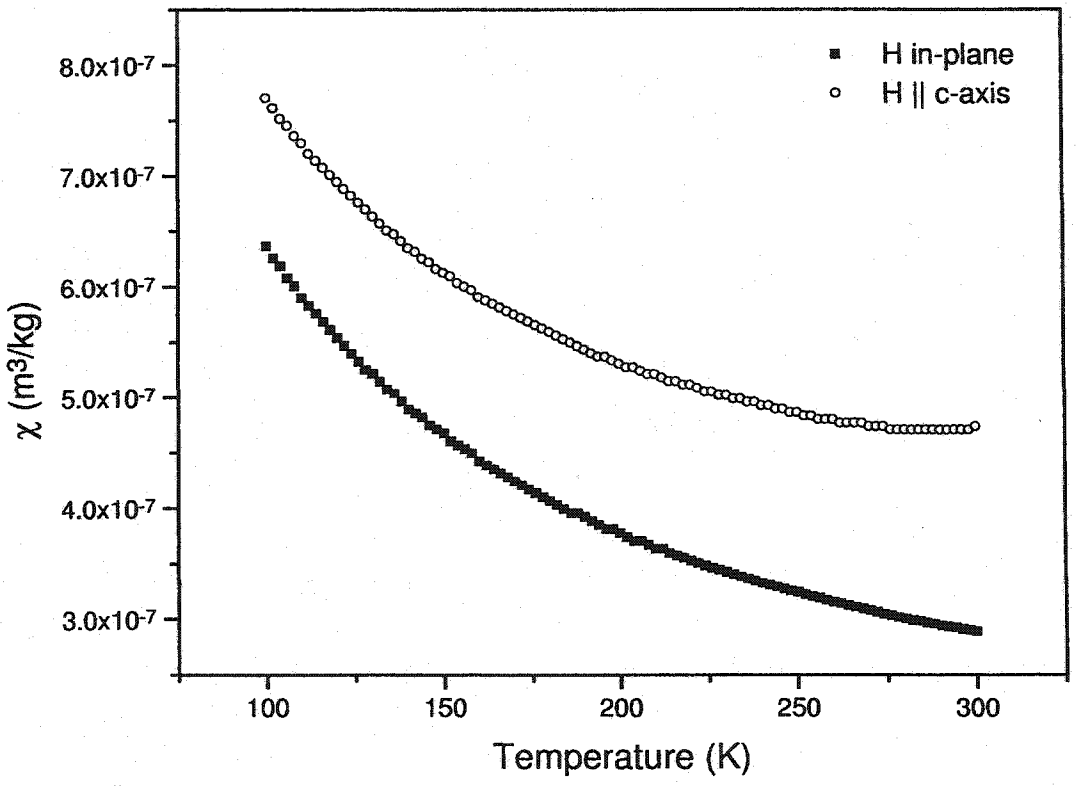

Figure 5.3: High-temperature dc susceptibility data for stage-1 $CoBr_2$-GIC. The in-plane field is 100 Oe and the c-axis field is 200 Oe.

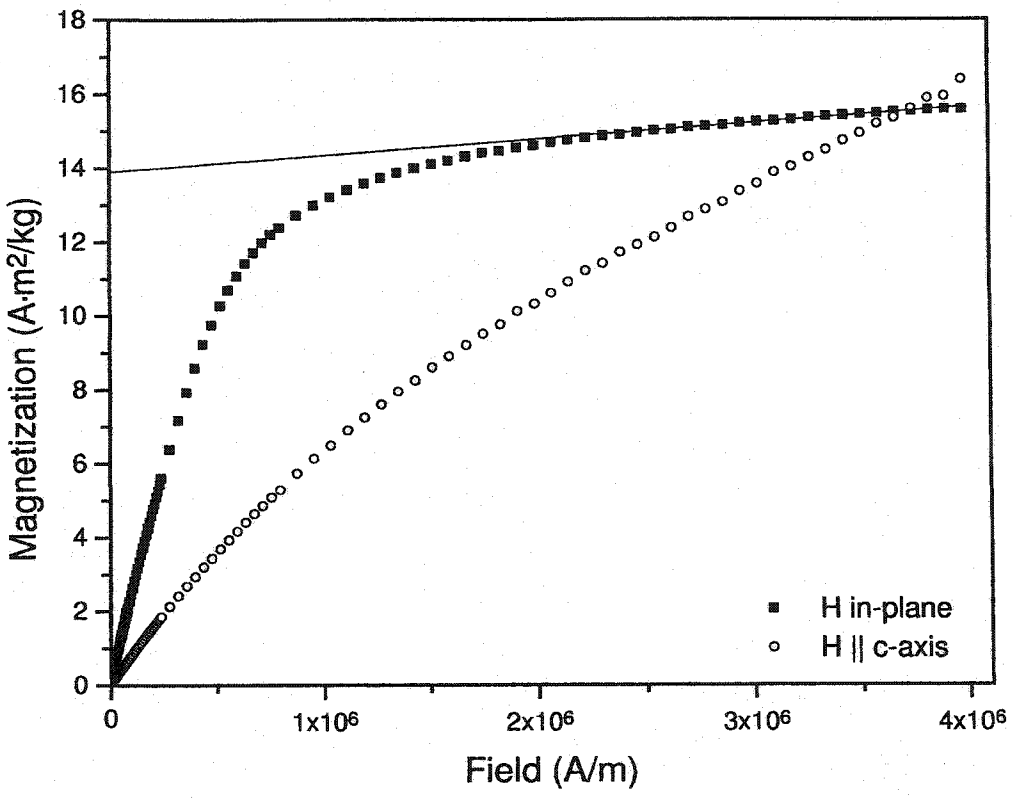

Figure 5.4: Magnetization *vs* applied field for stage-1 $CoBr_2$-GIC at T = 2 K. The line is a fit to the high-field region.

at high field for the in-plane measurement is common to the chloride-GICs[63, 66, 81] and has been attributed to a van Vleck "temperature-independent" paramagnetism. The saturation magnetization is considered to be the point where the high-field linear region is extrapolated back to H=0. There is no saturation of the c-axis measurement at these fields.

A comparison between the in-plane and c-axis ac susceptibilities is given in figure 5.5. In both cases, there is no transition down to 2 K, confirming the dc results.

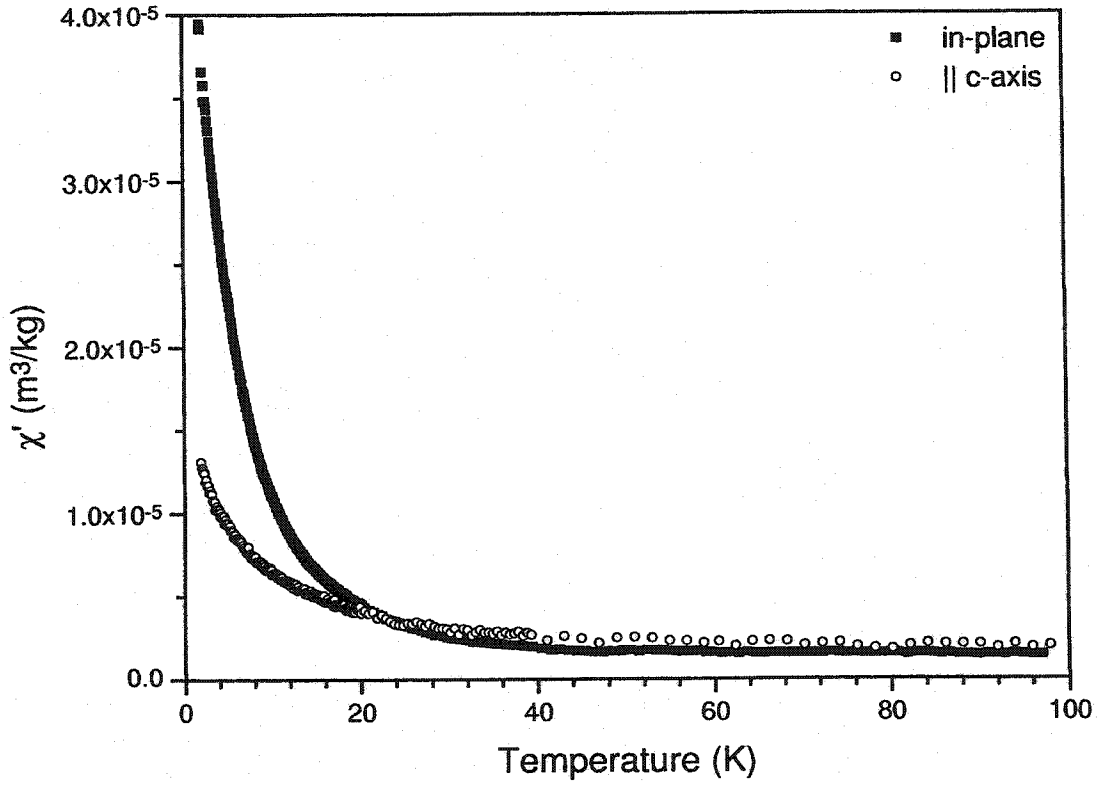

Figure 5.5: Comparison of in-plane and c-axis ac susceptibilities of stage-1 $CoBr_2$-GIC.

The c-axis susceptibility is much smaller at low temperatures, which is confirmed by the smaller initial slope in the magnetization curve for the c-axis measurement in figure 5.4.

The low temperature in-plane dc susceptibility for stage-2 $CoBr_2$-GIC at various applied fields is presented in figure 5.6. As in the stage-1 compound, there is no transition and no dependence on applied field. The scatter in the 10 Oe data points is caused by the low magnetic signal of this sample in such a small field.

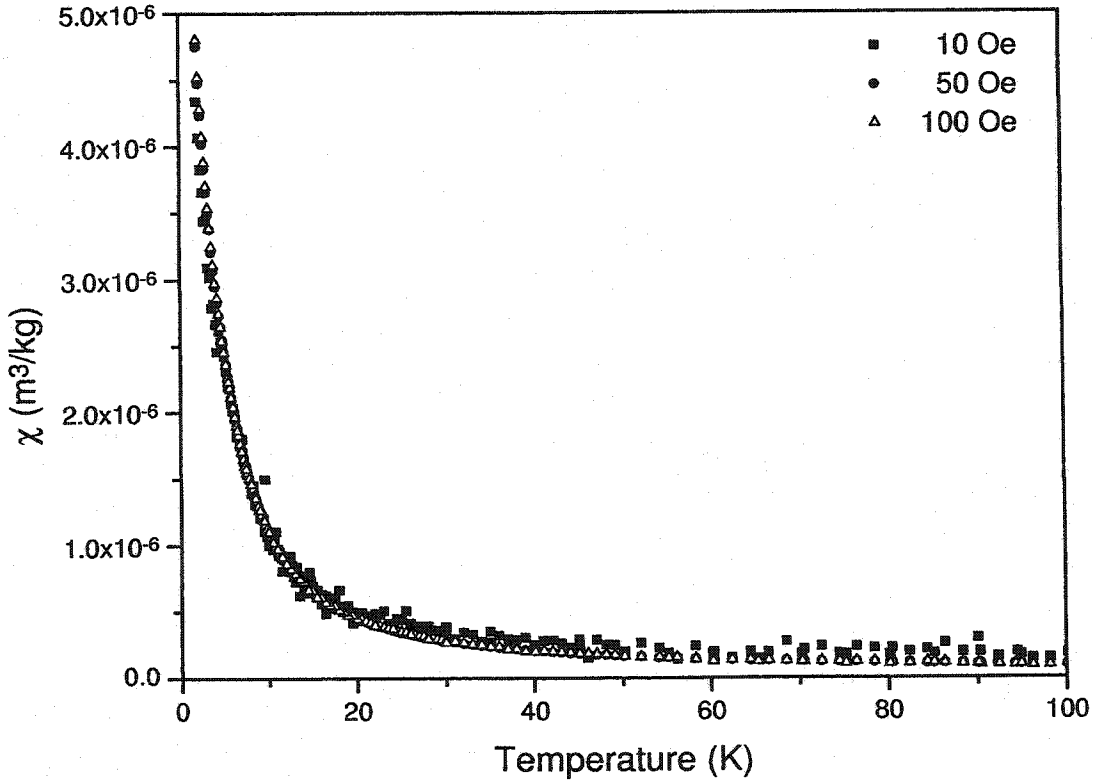

Figure 5.6: Low temperature in-plane dc susceptibility data for stage-2 $CoBr_2$-GIC with applied fields of 10, 50 and 100 Oe.

The c-axis susceptibility for stage-2 $CoBr_2$-GIC is shown in figure 5.7 for applied fields of 50, 100 and 200 Oe. A field-dependent step is seen near 30 K. This is clearly too high to be a magnetic transition since the Néel temperature of the pristine material is 19 K. Also, this feature is not seen in the in-plane susceptibility. The step is reversible, indicating that this is a real feature of the material. The effect of increasing the applied field is to reduce the temperature at which the step occurs. Doubling the field decreases the temperature by approximately 1.5 K. This may be

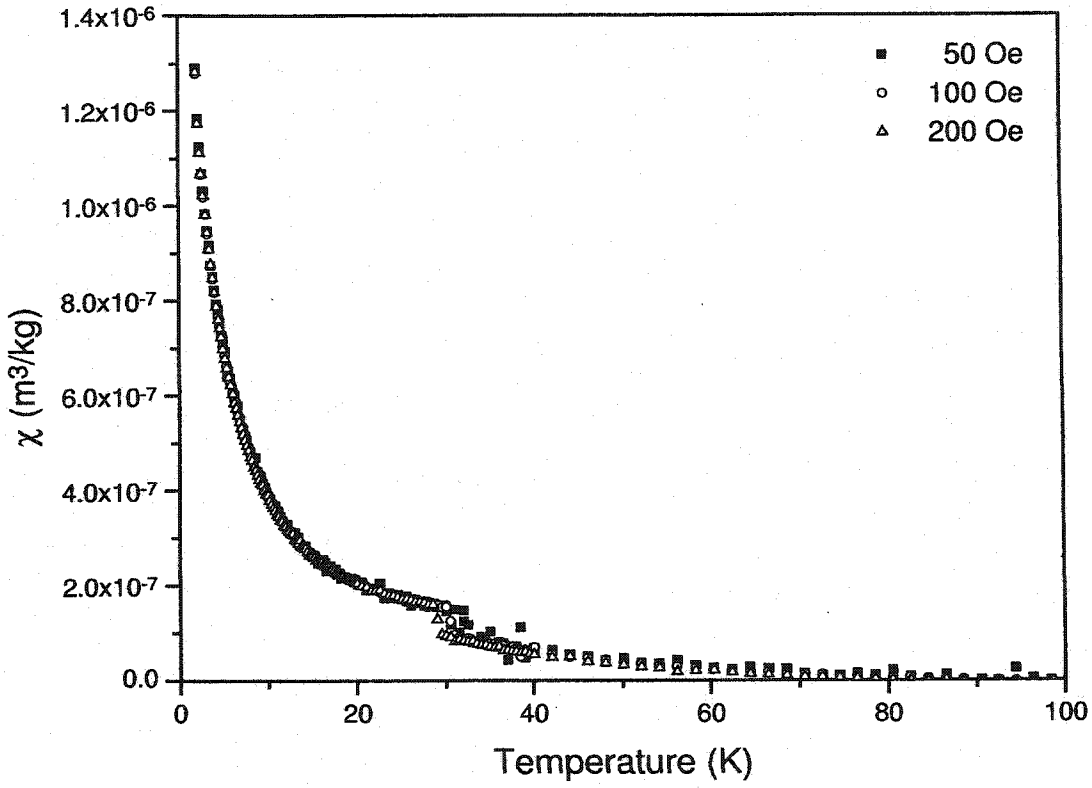

Figure 5.7: Low temperature c-axis dc susceptibility data for stage-2 $CoBr_2$-GIC.

associated with the energy required to cant the magnetic moments out of the plane.

Figure 5.8 shows the high temperature in-plane dc susceptibility for stage-2 $CoBr_2$. Oscillations in the signal appear as the temperature is increased. This seems to be a systematic artifact as these oscillations are seen in other low magnetic signal samples.

The in-plane magnetization curve for stage-2 $CoBr_2$-GIC is shown in figure 5.9. The magnetization does not completely saturate, but maintains a small susceptibility

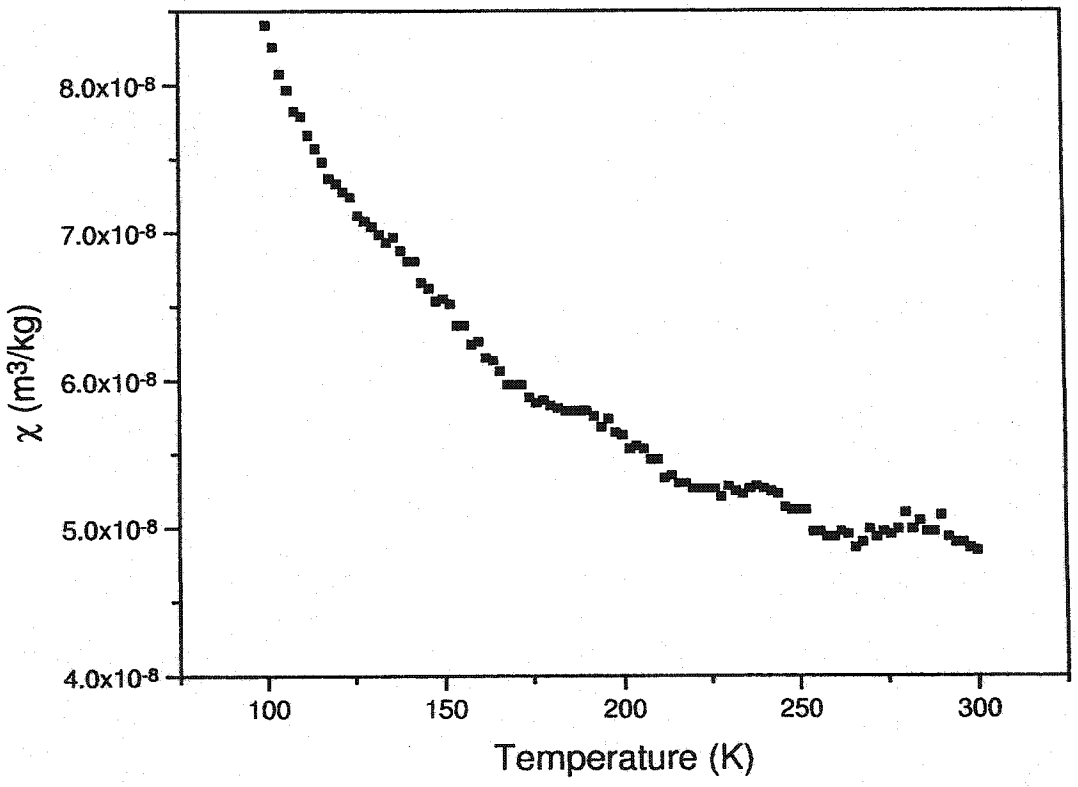

Figure 5.8: High temperature in-plane dc susceptibility data for stage-2 $CoBr_2$-GIC.

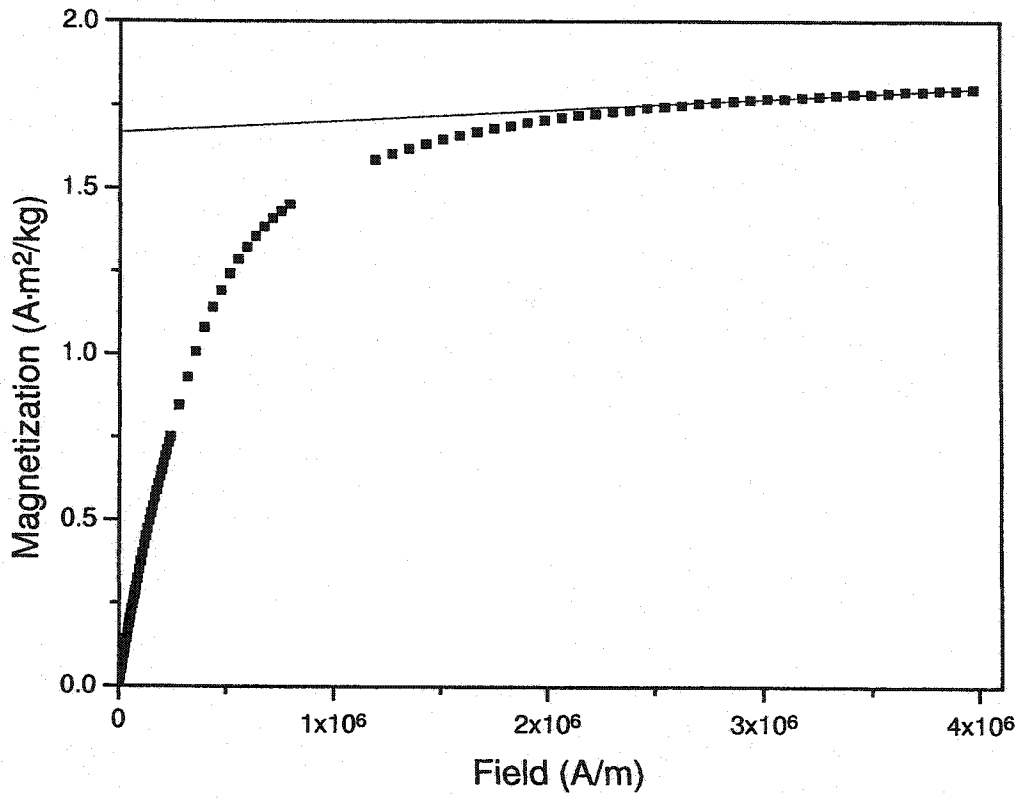

Figure 5.9: In-plane magnetization curve for stage-2 $CoBr_2$-GIC at T=2 K. The line is a fit to the high-field region.

at high fields, as did the first stage compound. While the saturation magnetization, as determined by extrapolation from the high field region, and high field susceptibility have decreased by an order of magnitude, the saturation field remains essentially unchanged between the two stages.

The ac susceptibility curves for stage-2 $CoBr_2$, both in-plane and c-axis, are shown in figure 5.10. There is too much scatter in the c-axis data to see any features. The in-plane data are much less noisy, but also has no features on the curve, indicat-

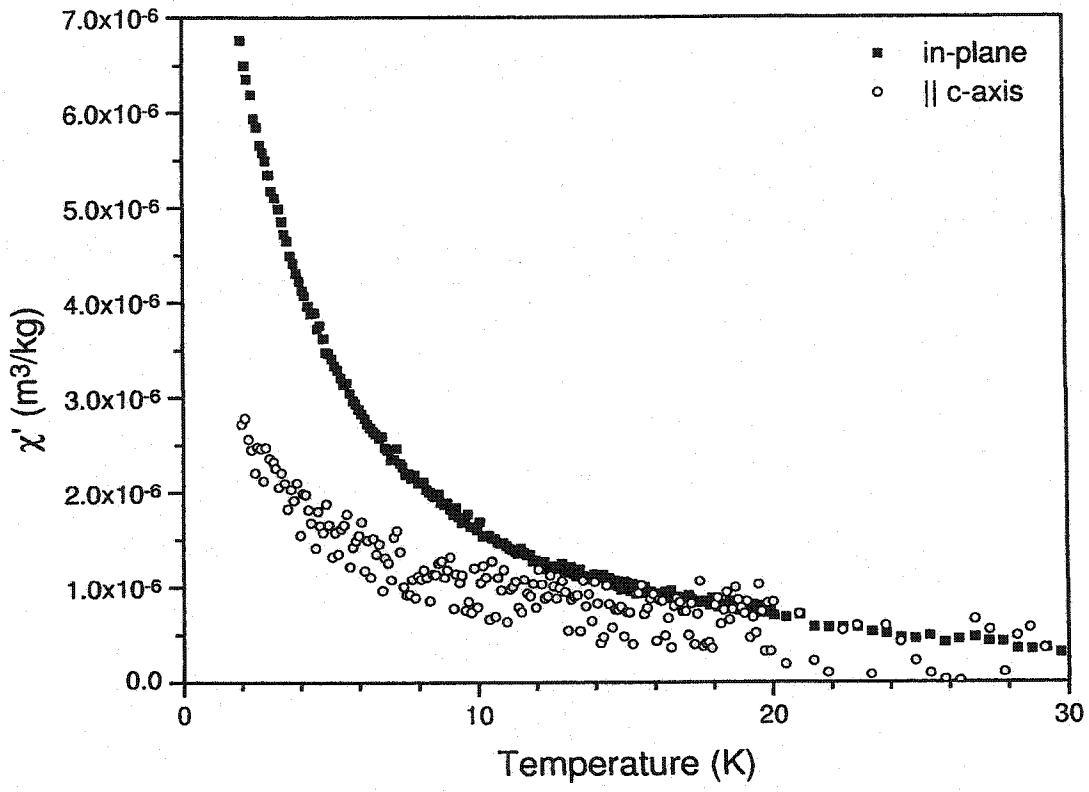

Figure 5.10: Comparison of in-plane and c-axis ac susceptibilities of stage-2 $CoBr_2$-GIC.

ing that the sample undergoes no magnetic phase transitions down to 2 K. There is a significant difference in the magnitude of the two curves, indicating anisotropy as seen in the stage-1 sample.

Neutron scattering experiments were performed on a single crystal sample of stage-3 $CoBr_2$-GIC. The experiments were performed at the C5 facilities at AECL Chalk River Laboratories. The lowest temperature that was achievable was 5 K, but temperature stability problems constrained the work to above 5.5 K. Data from runs

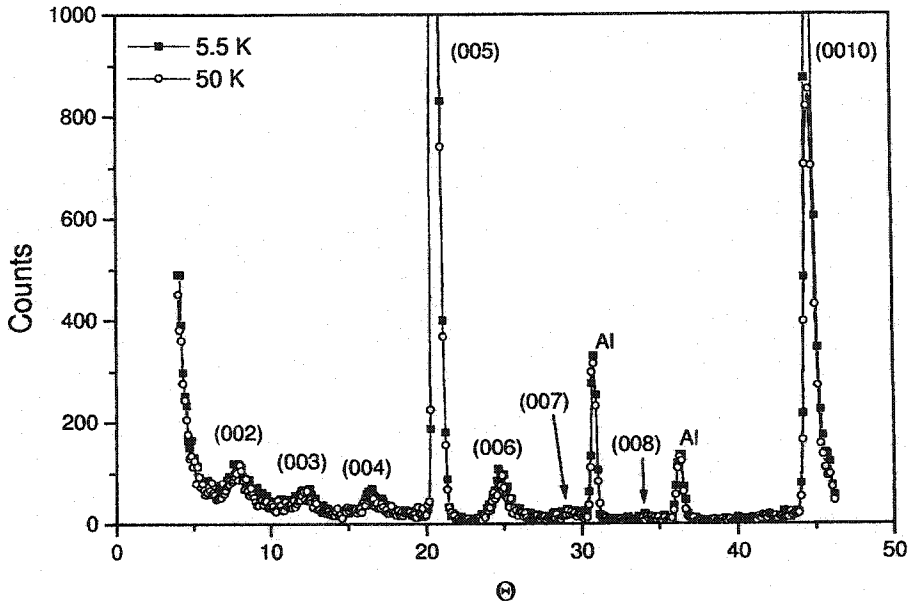

Figure 5.11: Neutron diffraction pattern for single-crystal stage-3 $CoBr_2$-GIC sample at T=50 K and T=5.5 K.

at 50 K and at 5.5 K are shown in figure 5.11. The pattern is clearly that of the stage-3 compound, with a pattern similar to that of the x-ray diffraction. For the same reasons as explained in the x-ray analysis, the largest and sharpest peaks are the (005) and (0010) diffraction lines. The peaks attributed to aluminum are due to scattering from the sample holder.

By subtracting the 50 K data from the 5.5 K data, as shown in figure 5.12, we can examine any changes in the structure caused by decreasing the temperature. The only peaks visible are the atomic Bragg peaks, no magnetic Bragg peaks are present. Magnetic Bragg peaks are caused by the scattering of neutrons from the magnetic

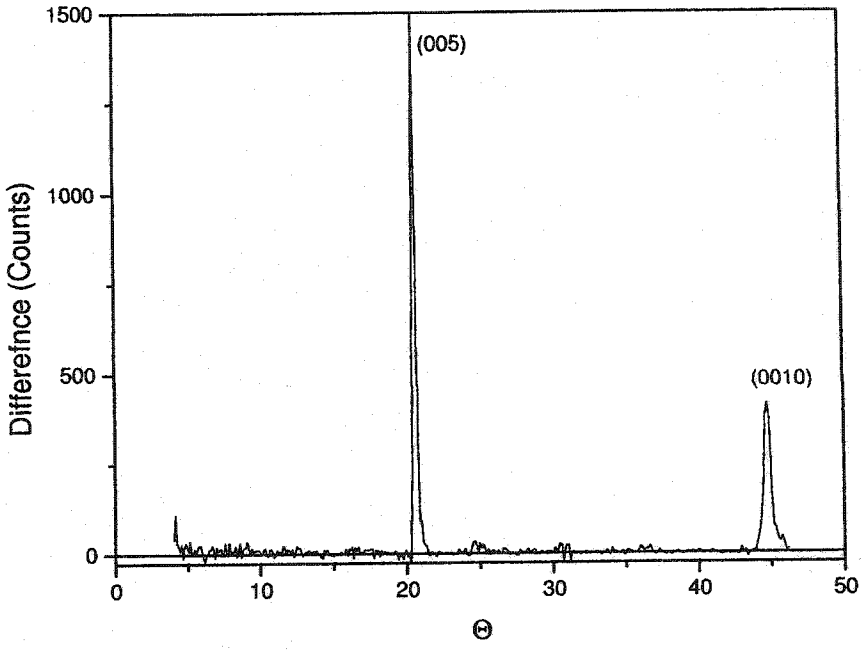

Figure 5.12: Difference between neutron scattering from stage-3 $CoBr_2$-GIC at 50 K and 5.5 K

lattice, defined by the ordering of the magnetic moments. Their absence indicates a lack of magnetic ordering. Also, from examining the background level, there is no change in the diffuse paramagnetic scattering. In a paramagnetic state, magnetic moments are randomly oriented and so must scatter neutrons in random directions. If there were any increased ordering, the paramagnetic scattering would decrease and the background in subtracting the high temperature data would be negative. The background seen here is zero.

5.2 $FeBr_2$

The low-temperature dc susceptibility of stage-2 $FeBr_2$-GIC is shown in figure 5.13 for an in-plane applied field of 2 Oe. There are several features in this plot that are worth noting. There are steps in the susceptibility at T = 14.5 and 8.5 K. These indicate an increase in the magnetic ordering of the sample. Also there is a difference between the ZFC (lower) and FC (upper) data beginning at 14.5 K. This shows that there is an irreversible effect in the ordering. Finally, at 3.2 K, there is a peak in the ZFC data while there is merely a decrease in slope of the FC data. This shows another type of ordering in the sample, accompanied by a larger irreversibility. The nature of the ordering, however, cannot be discerned from just this data.

The step in the ZFC data at 4.4 K is caused by heating the system through the crossover temperature. When the system is heated through the boiling point of helium, the liquid helium inside the cooling annulus must be boiled off. This can take several minutes, during which time the magnetic field is still applied. For samples with relaxation effects, whose magnetization changes with time in a constant field, this results in a sudden change in the magnetization measured, as is the case in figure 5.13.

By varying the applied field, as shown in figure 5.14, several changes occur. With increased field, the separation between the ZFC and FC data below 14.5 K decreases. With an applied field of 100 Oe, there is no longer a difference between the ZFC and FC above the 3 K peak and the steps at 8.5 and 14.5 K disappear. The

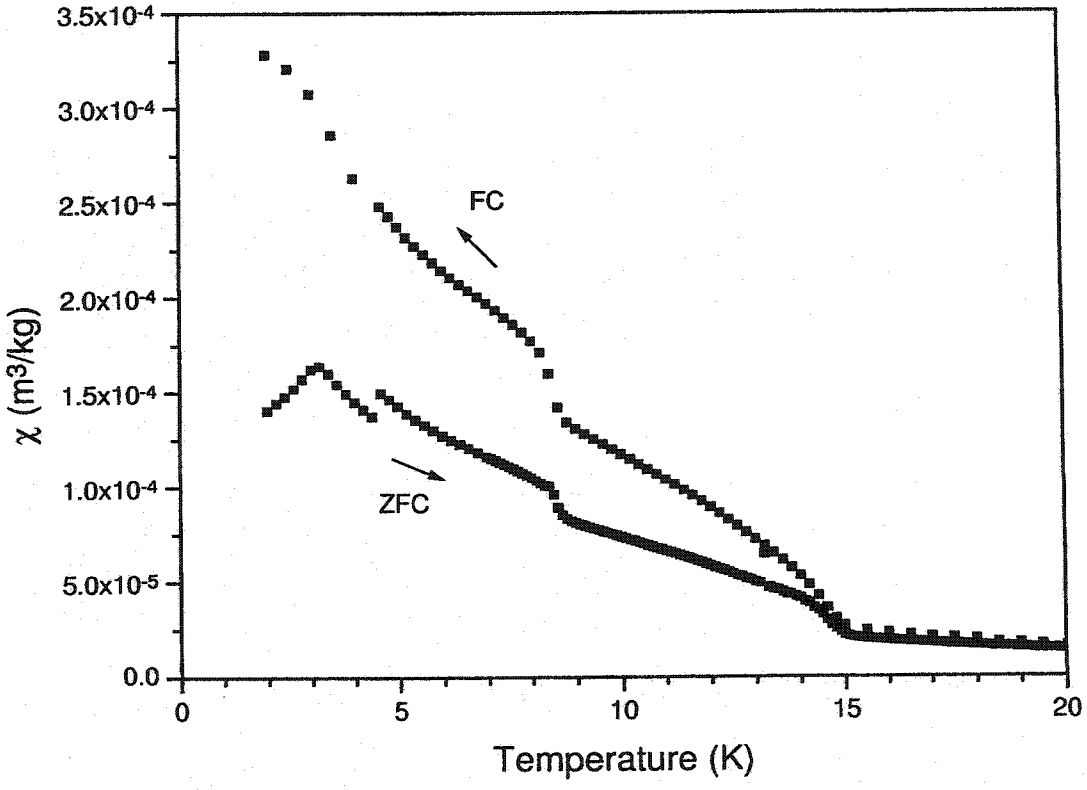

Figure 5.13: Low temperature dc susceptibility of stage-2 $FeBr_2$-GIC showing ZFC and FC data. H = 2 Oe. The step at 4.4 K is systematic.

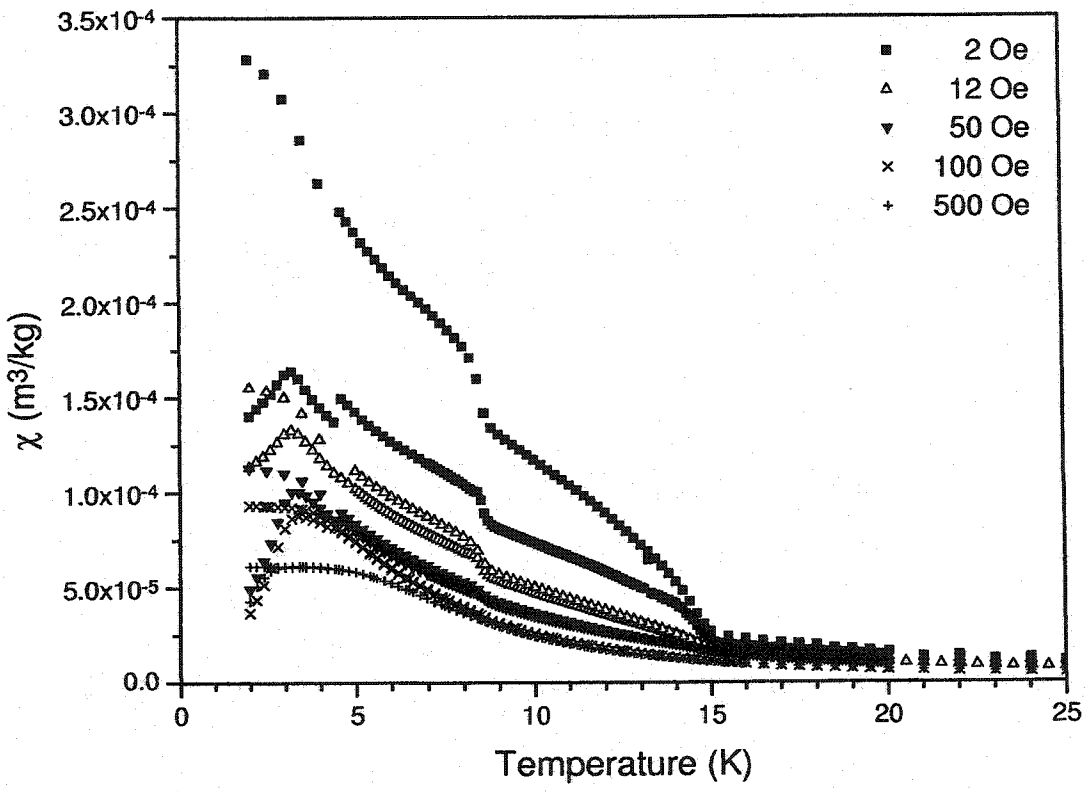

Figure 5.14: Low temperature dc susceptibility of stage-2 $FeBr_2$-GIC at various applied in-plane fields. ZFC and FC data are shown.

FC data below 3 K have less temperature dependence with increasing field and, again with 100 Oe applied field, the FC susceptibility below 3 K is flat. The size of the 3 K peak is also decreased with an increase in applied field.

Figure 5.15 shows the low temperature c-axis dc susceptibility for the stage-2 $FeBr_2$-GIC, for both FC and ZFC measurements. The magnitude of the susceptibility is smaller than that of the in-plane susceptibility, as shown by the scale. At 10 Oe, the peak at 3 K and the shoulders at 8.5 K and 14.5 K are all present as is the

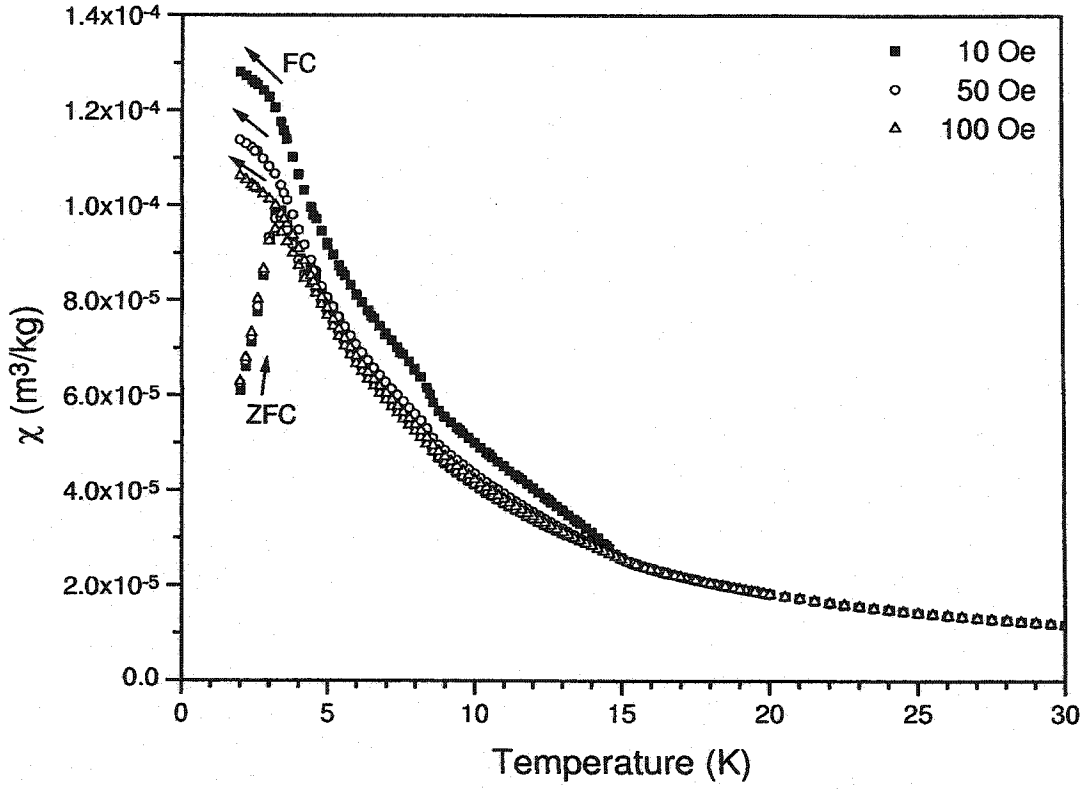

Figure 5.15: Low temperature dc susceptibility of stage-2 $FeBr_2$-GIC at various fields applied along the c-axis. ZFC and FC data are shown.

remnant magnetization, shown by the difference between the ZFC and FC data. The ZFC measurements show very little dependence on applied field.

The in-plane and c-axis magnetization curves for the stage-2 $FeBr_2$-GIC are shown in figure 5.16. There are several interesting features to note. First, in the in-plane measurement, there is a strong high-field susceptibility, $\frac{dM}{dH}$, above the saturation field, shown by the positive slope at high field. Second, there is a change in slope at lower field ($\sim 7\times10^4$ A/m). This is more clearly seen in the inset in figure

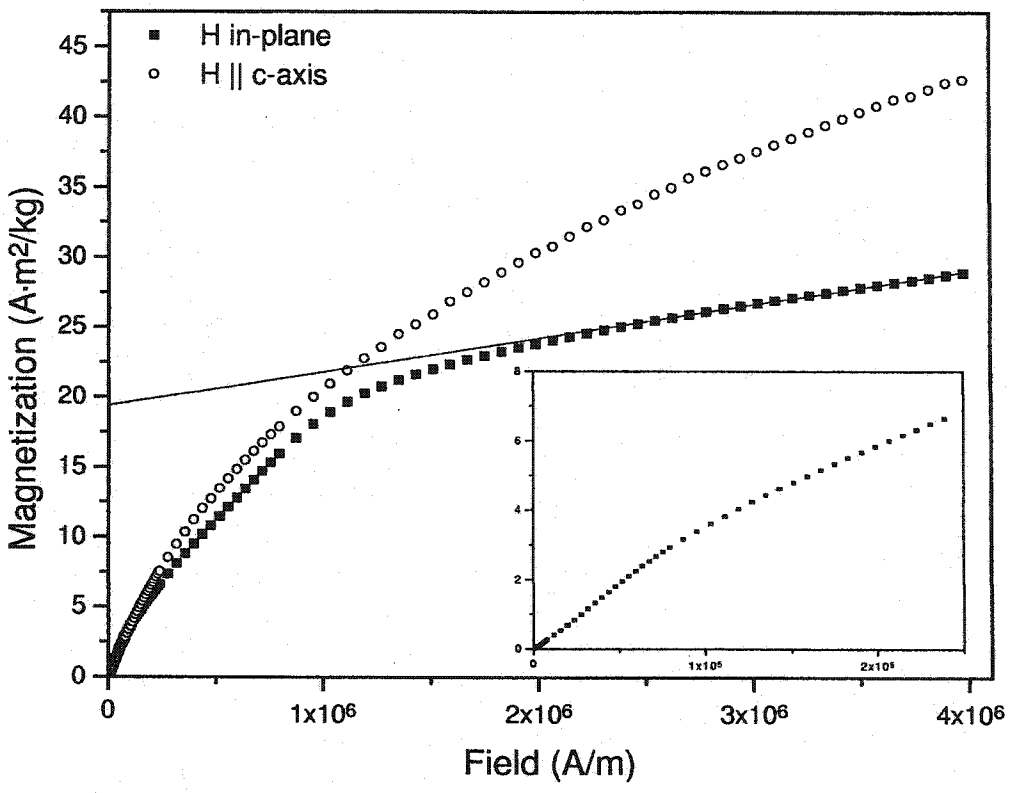

Figure 5.16: Magnetization curves for stage-2 $FeBr_2$-GIC at T=2 K.

5.16. This change represents a decrease in dc susceptibility with increasing field. Finally, there is an increase in dc susceptibility at still lower field ($\sim 3 \times 10^4$ A/m).

The c-axis measurement, on the other hand, does not have any of these features. The c-axis dc susceptibility decreases continuously up to high fields. There is no obvious saturation point for the c-axis measurement.

The ac susceptibility, shown in figure 5.17, also has several features, corresponding to those seen in the dc data. The dispersion, χ' has a peak at 4.5 K with

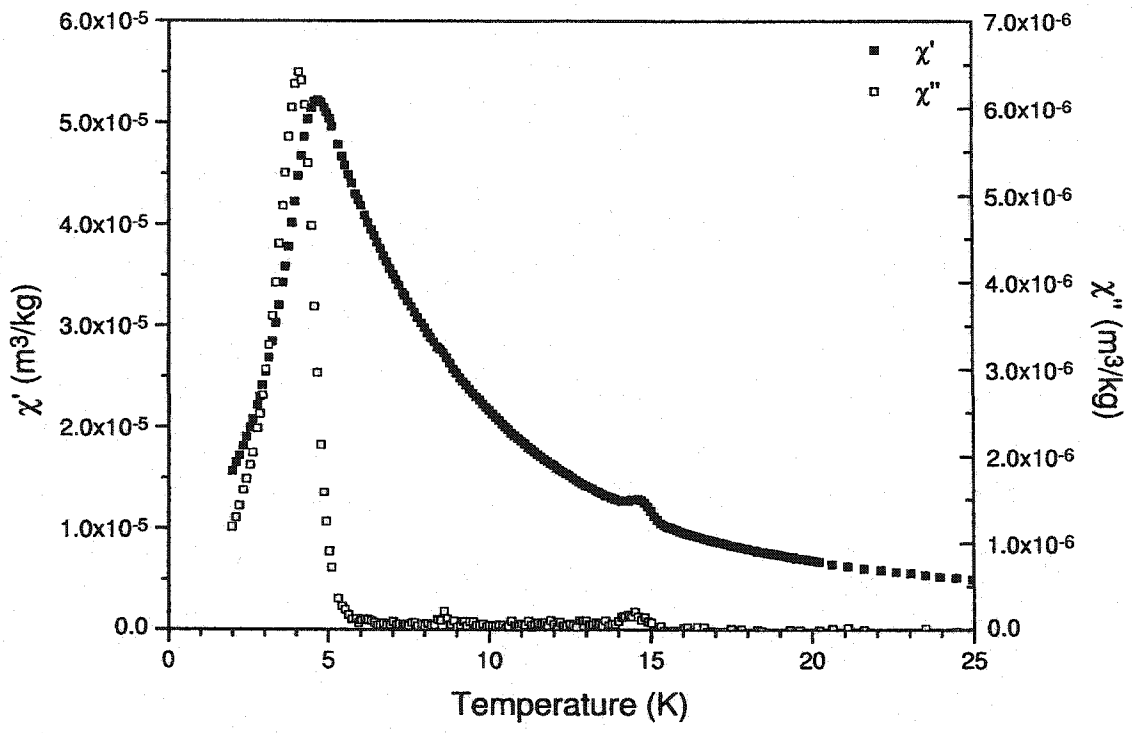

Figure 5.17: In-plane ac susceptibility data for stage-2 $FeBr_2$-GIC.

shoulders at 8.5 K and 14.5 K. The absorption, χ'' has peaks at 14.5 K, 8.5 K and 4 K. The temperatures of the two higher peaks correspond exactly to the peaks in χ'. The low temperature peak in χ'' is slightly lower in temperature than the matching peak in χ', but χ'' begins to increase sharply near the peak in χ'.

The frequency dependence of χ' is shown in figure 5.18. With increasing frequency, the lowest temperature peak moves to higher temperature and decreases in magnitude. There is no discernible effect of frequency on the other two steps.

The c-axis ac susceptibility is shown in figure 5.19 in comparison to the in-

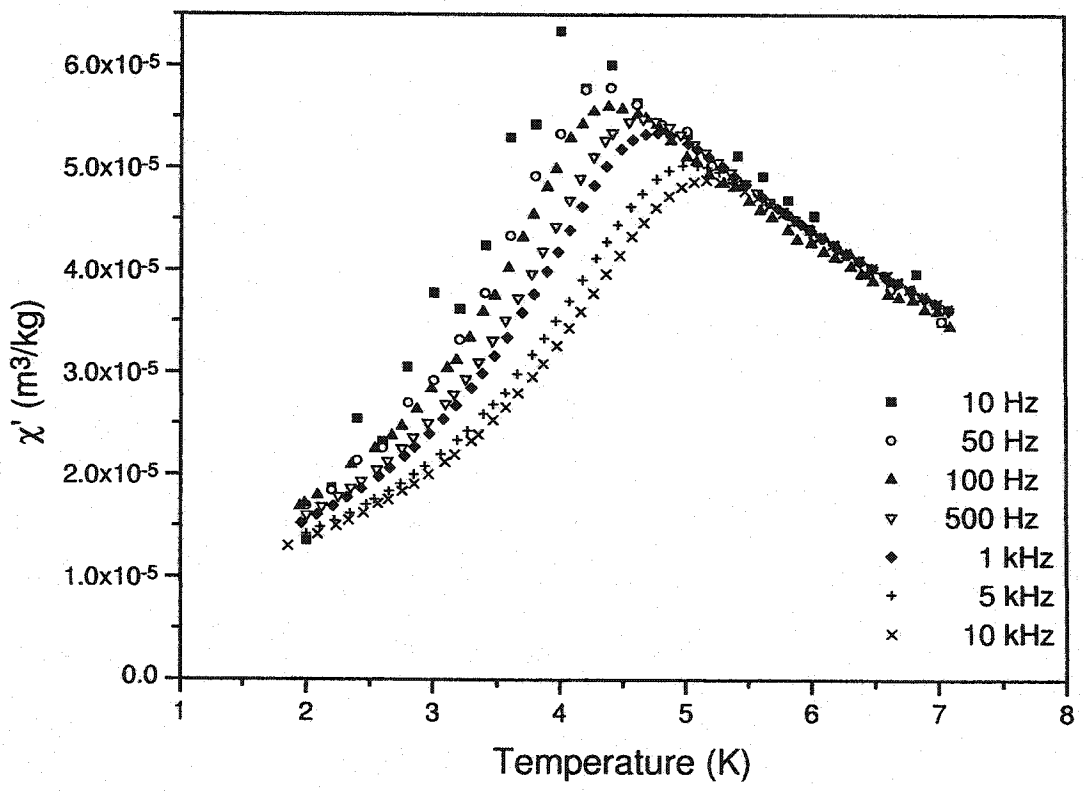

Figure 5.18: Frequency dependence of in-plane ac susceptibility of stage-2 $FeBr_2$-GIC.

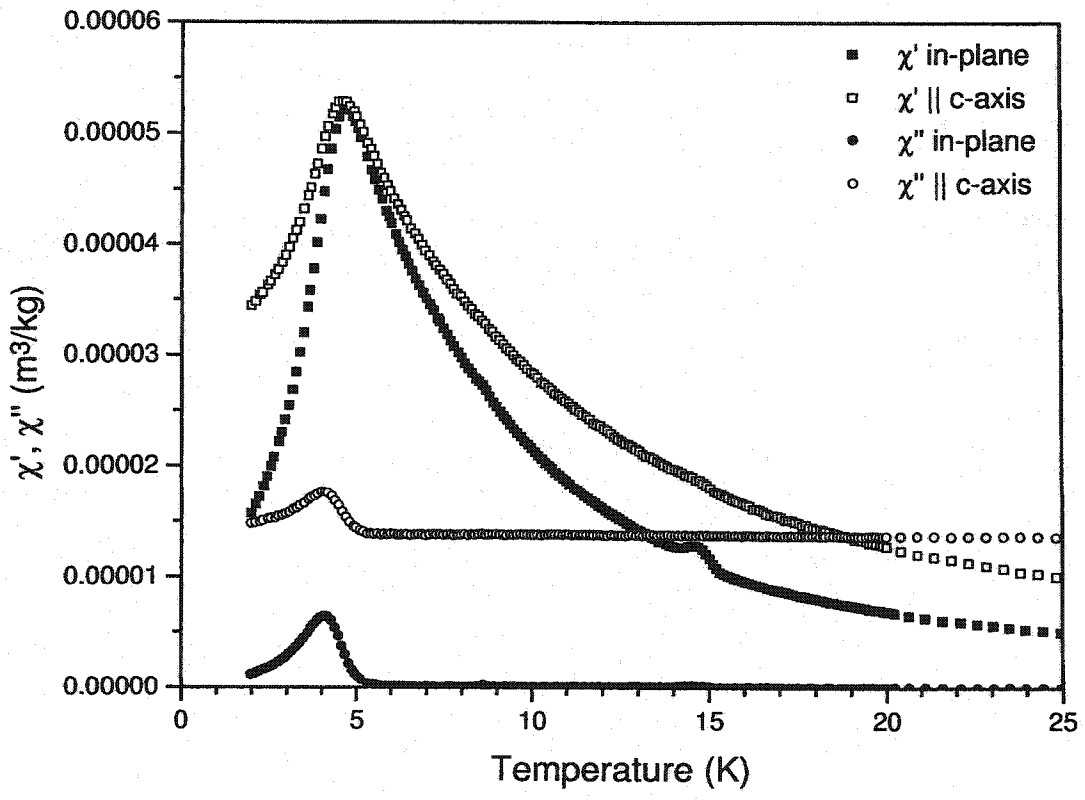

Figure 5.19: Comparison of in-plane and c-axis ac susceptibilities of stage-2 $FeBr_2$-GIC.

plane susceptibility. Although both the in-plane and c-axis dispersions have the same peak magnitude, the in-plane peak is much sharper. There is a positive offset in the c-axis absorption. This indicates a temperature-independent absorption mechanism induced by the change in orientation. One possibility is that this is caused by eddy currents induced within the sample by the oscillating magnetic field.

Specific heat measurements for stage-2 $FeBr_2$-GIC are shown in figure 5.20, plotted in the standard form of C/T *vs* T^2. There is a peak at 8.5 K, which matches

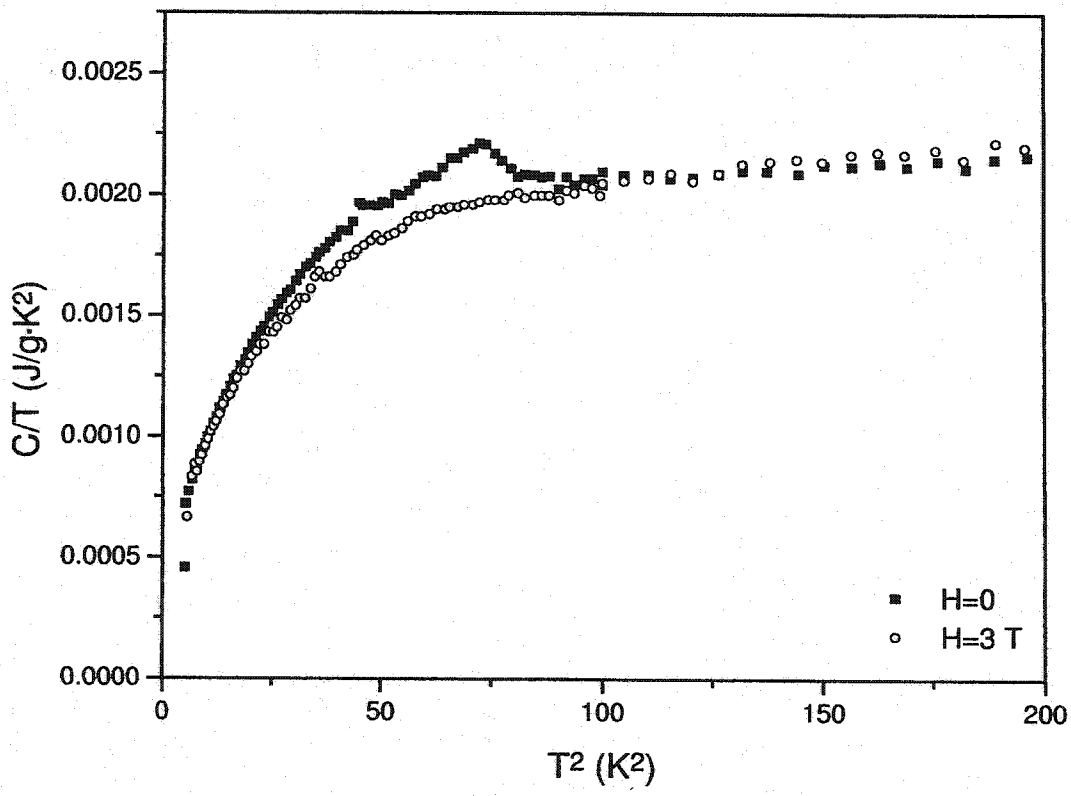

Figure 5.20: Specific heat of stage-2 $FeBr_2$-GIC divided by T plotted against T^2. The peak at 8.5 K corresponds to the shoulder in both the ac and dc susceptibilities. Data for both zero and 3 T applied field are shown.

the peak at 8.5 K in both ac and dc susceptibility measurements. No features are seen at either the lower or higher temperatures at which features appear in the susceptibility data. With the application of a magnetic field, the peak size decreases and is completely gone at 3 T.

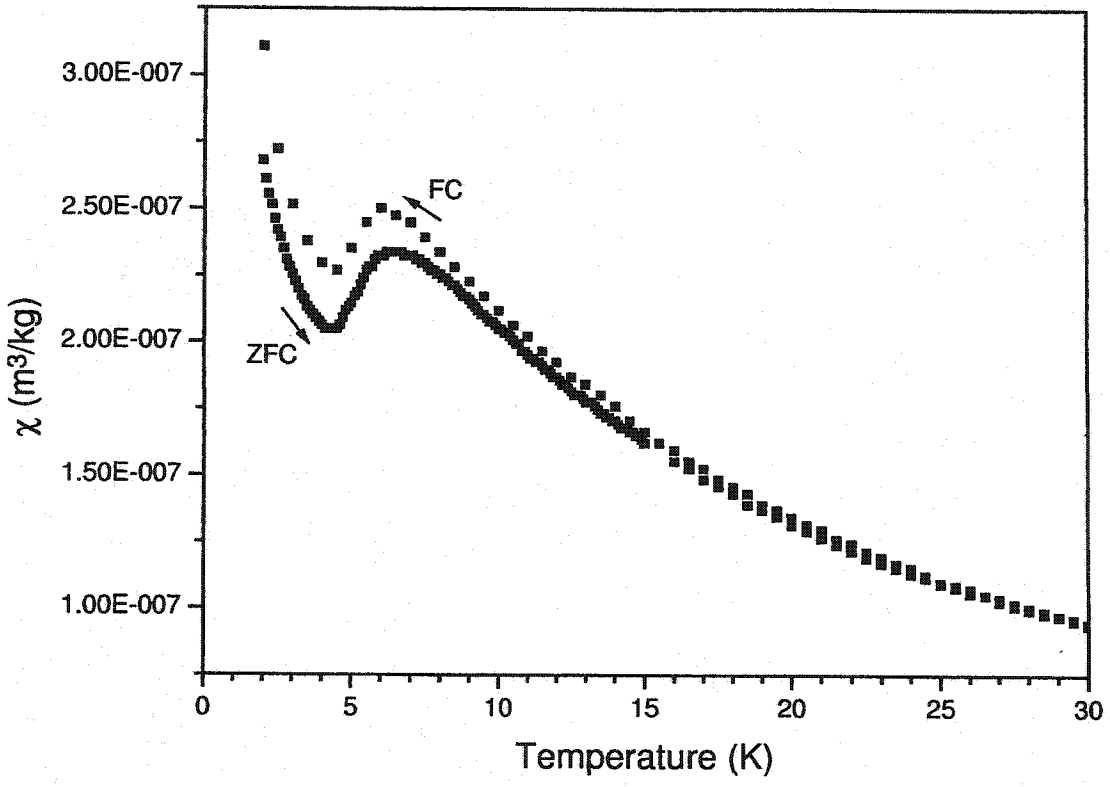

Figure 5.21: Low temperature dc susceptibility data for stage-2 $NiBr_2$-GIC showing ZFC and FC data. H=20 Oe in-plane.

5.3 $NiBr_2$

Figure 5.21 shows the low temperature dc susceptibility for stage-2 $NiBr_2$-GIC. Both the ZFC and FC data are given for an applied in-plane field of 20 Oe. There is a peak at 7 K and a local minimum at 5 K, below which the susceptibility increases again. There is a small difference between the ZFC and FC data, but both have the extrema at the same temperatures.

Figure 5.22 shows the effect of applied field on the low temperature suscepti-

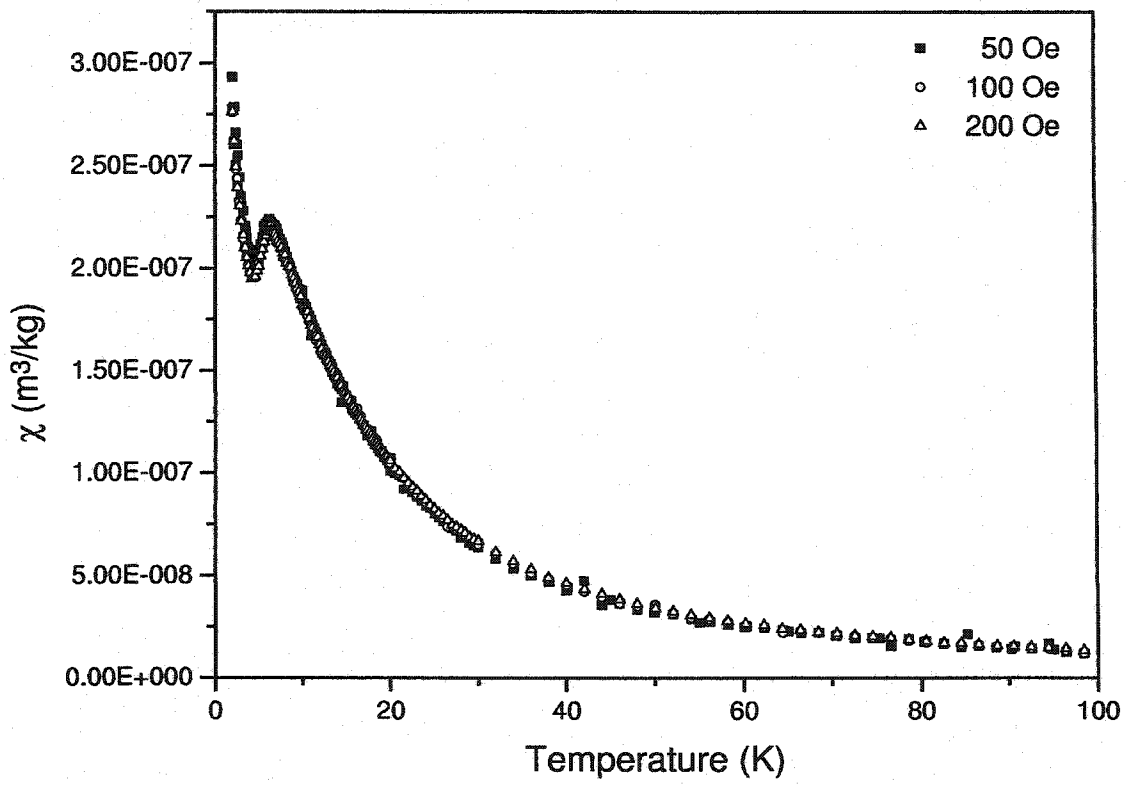

Figure 5.22: Low temperature dc susceptibility data for stage-2 $NiBr_2$-GIC at various applied in-plane fields.

bility. Clearly, there is little dependence on field except that the difference between the ZFC and FC data diminishes with increasing field.

The high temperature dc susceptibility is shown in figure 5.23. The oscillations at higher temperature are systematic and appear only because of the extremely small signal from the sample.

The magnetization curve for a stage-2 $NiBr_2$-GIC is shown in figure 5.24. A

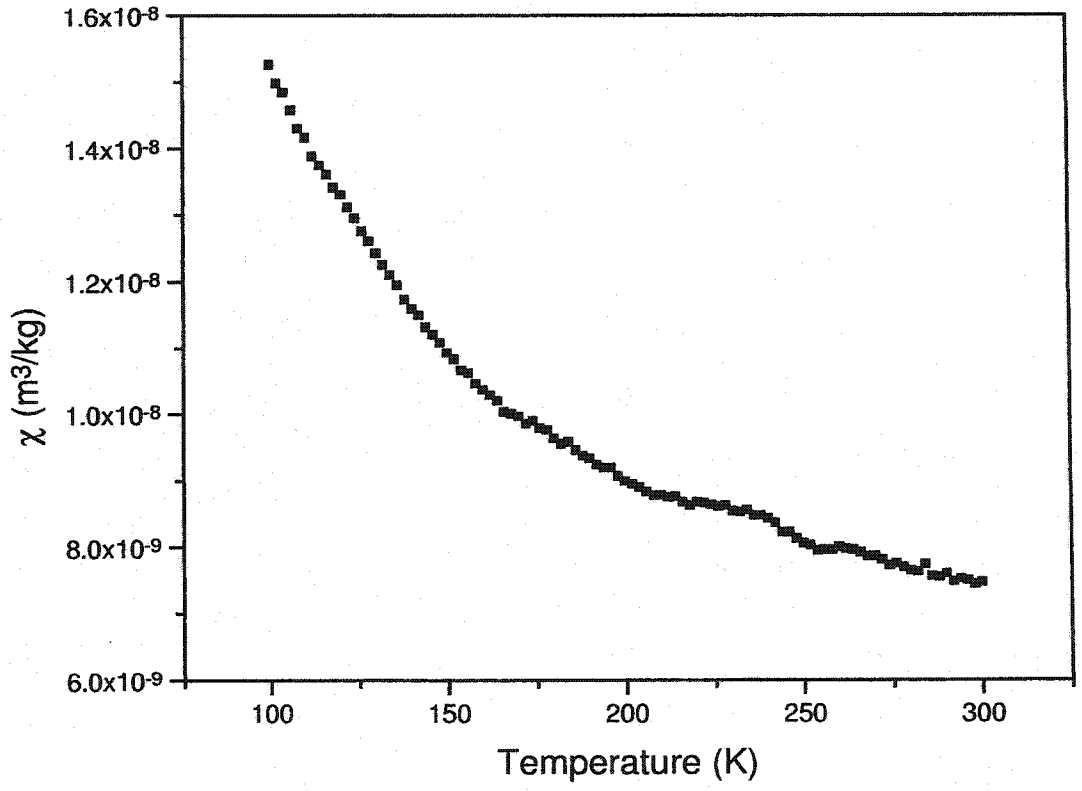

Figure 5.23: High temperature dc susceptibility data for stage-2 $NiBr_2$-GIC.

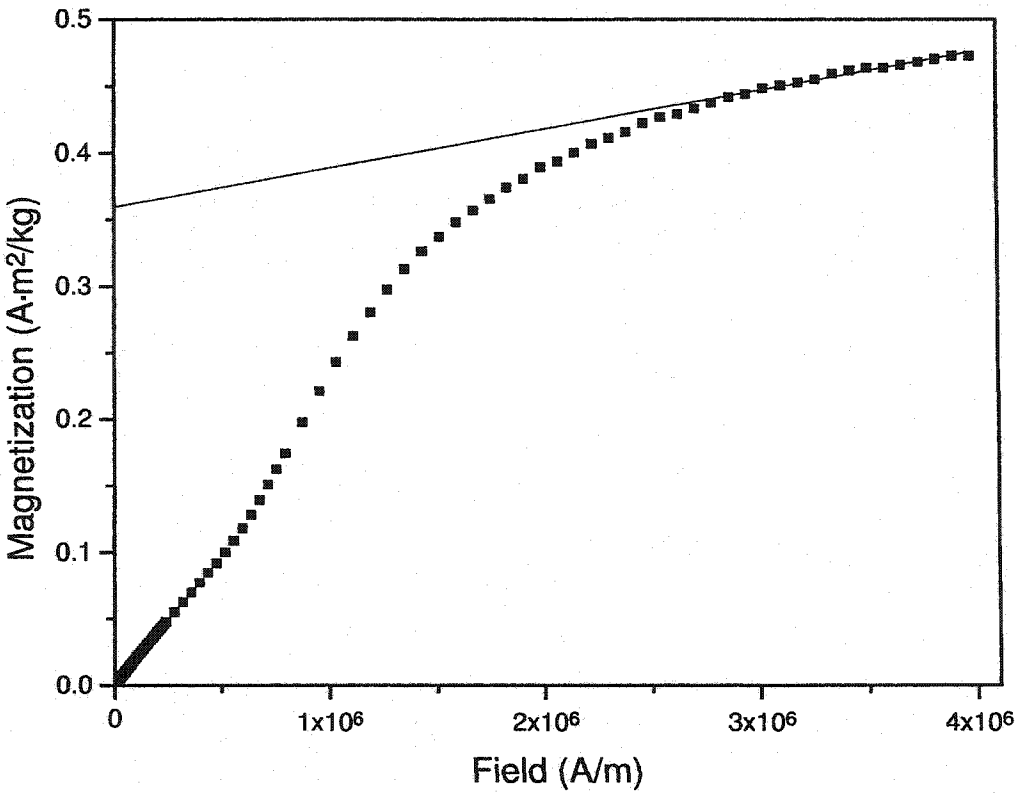

Figure 5.24: In-plane magnetization curve for stage-2 $NiBr_2$-GIC at T=2 K.

gradual increase in susceptibility (slope) occurs near $H=6\times10^5$ A/m. This is qualitatively similar to the metamagnetic transition seen in the pristine compound, and may indicate that there is ordering occurring in the compound. In a paramagnetic state, as in the case of $CoBr_2$-GIC, the slope of the magnetization curve should not increase, but rather remain constant until saturation begins, where the slope decreases.

The ac susceptibility for the stage-2 compound is shown in figure 5.25. No features are present, but there is considerable scatter in the data which could mask

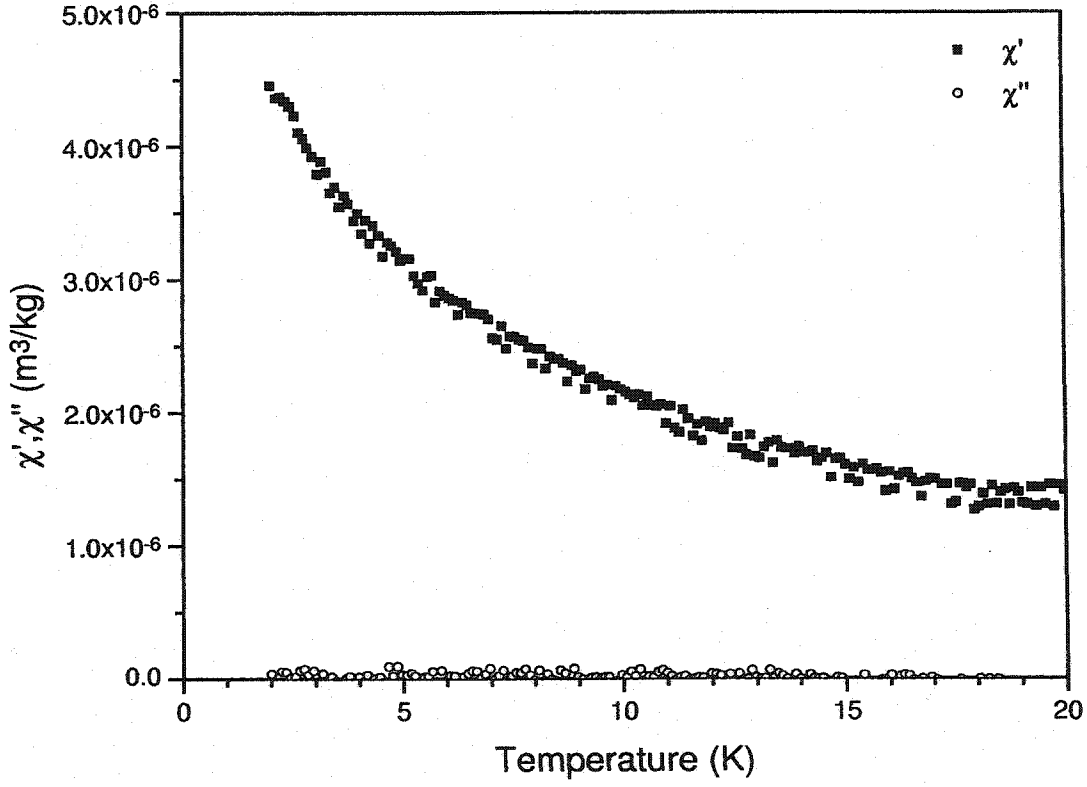

Figure 5.25: In-plane ac susceptibility data for stage-2 $NiBr_2$-GIC.

a small feature.

Figure 5.26 shows the low temperature dc susceptibility data for a stage-3 $NiBr_2$-GIC. A peak occurs near 7 K and a local minimum at 3 K. With an increase in applied field, the peak decreases in magnitude and the region below the minimum flattens out. This is qualitatively similar to the stage-2 compound, except that the peak is much broader. This sample was, unfortunately, damaged after this measurement and no suitable replacement could be prepared.

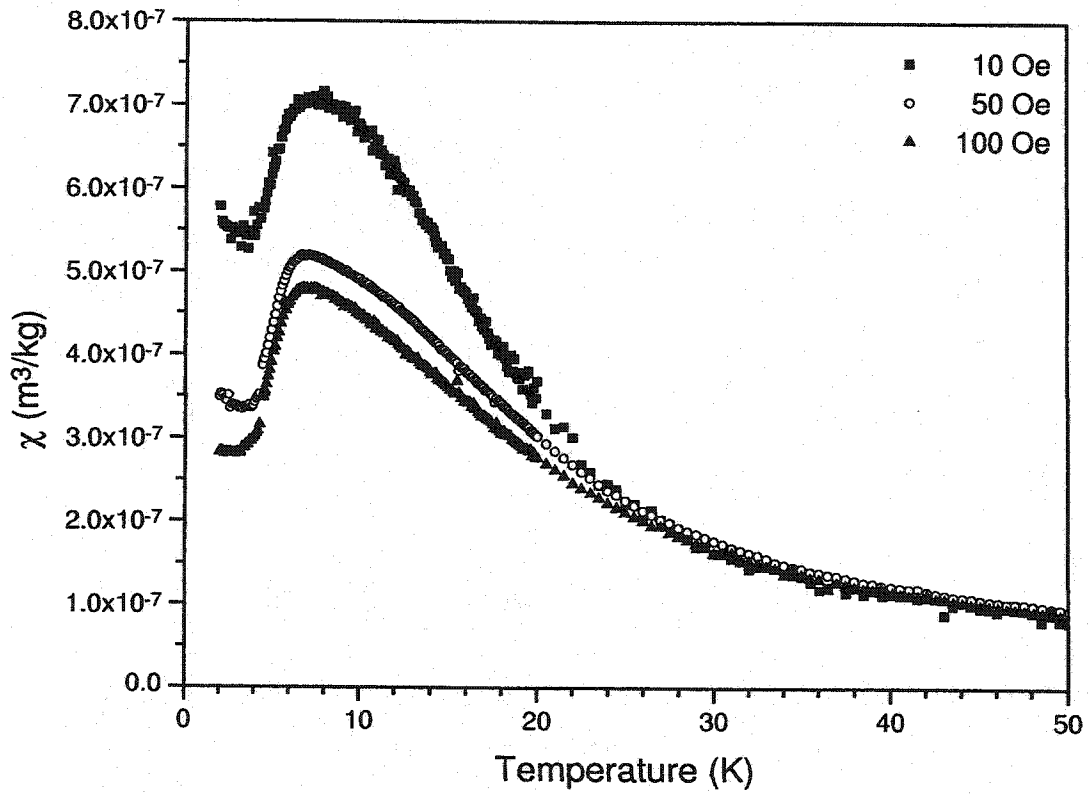

Figure 5.26: Low temperature dc susceptibility data for stage-3 $NiBr_2$-GIC at various applied in-plane fields.

The low temperature dc susceptibility for a stage-5 $NiBr_2$-GIC is shown in figure 5.27. Both the ZFC and FC data are shown. A peak is seen in the ZFC data, but the FC magnetization continues to increase below this temperature. This remnant magnetization is much more pronounced than that seen in the second stage compound.

The magnetization of the stage-5 compound is shown in figure 5.28 as a function of field. The magnetization reaches a maximum near H=1.5×10^6 A/m, then

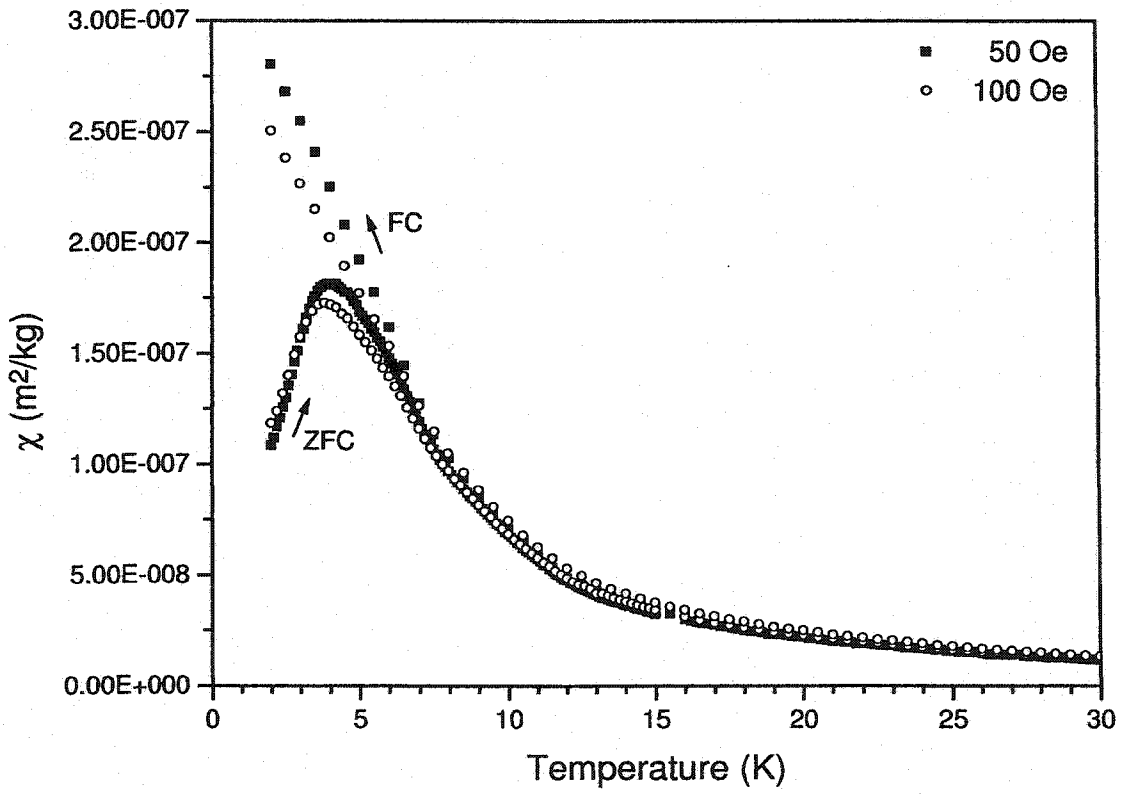

Figure 5.27: Low temperature dc susceptibility data for stage-5 $NiBr_2$-GIC. Fields are applied in-plane. ZFC and FC data are shown.

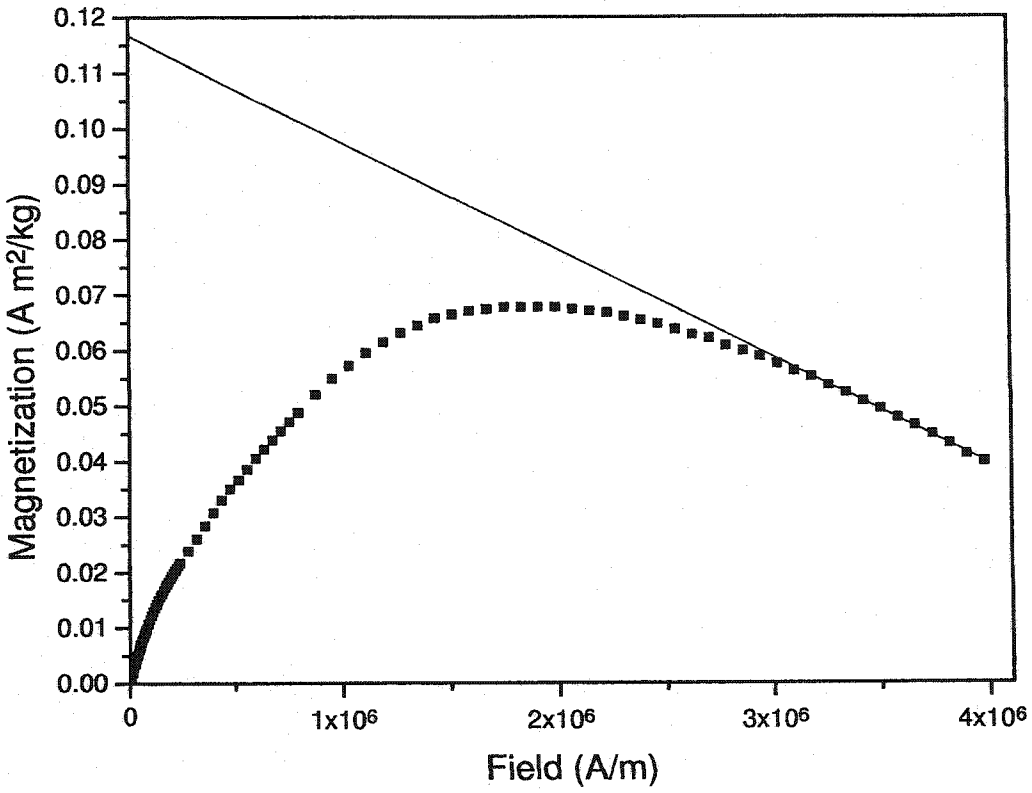

Figure 5.28: Magnetization as a function of applied field for stage-5 $NiBr_2$-GIC.

begins to decrease with increasing field. This indicates strong diamagnetism in the sample above the saturation field.

The ac susceptibility measurement for a stage-5 $NiBr_2$-GIC, shown in figure 5.29, has no peaks. There is some scatter in the data, but a smooth trend is evident. The imaginary part appears to have a negative slope and becomes negative at 13 K. This clearly indicates that there was a small offset of the phase angle on the lock-in amplifier. It is impossible for the imaginary part to be negative since χ'' is the ab-

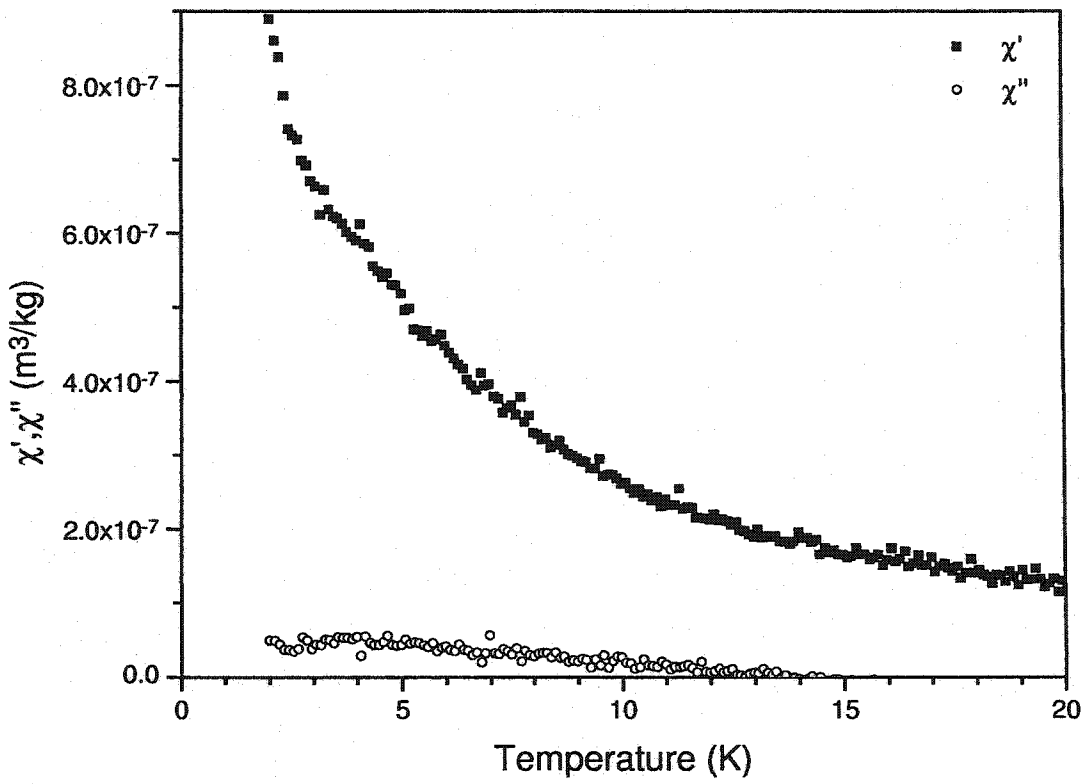

Figure 5.29: In-plane ac susceptibility data for stage-5 $NiBr_2$-GIC.

sorption and a negative value would, in essence, indicate the creation of energy from the material.

The specific heat measurements in figure 5.30 demonstrate that there is no difference between the zero applied field and high field (3T) data for the stage-5 $NiBr_2$-GIC. This indicates that there is no long-range magnetic ordering occurring in this temperature region. The plot of C_p/T *vs* T is nearly linear, indicating a strong quadratic temperature dependence.

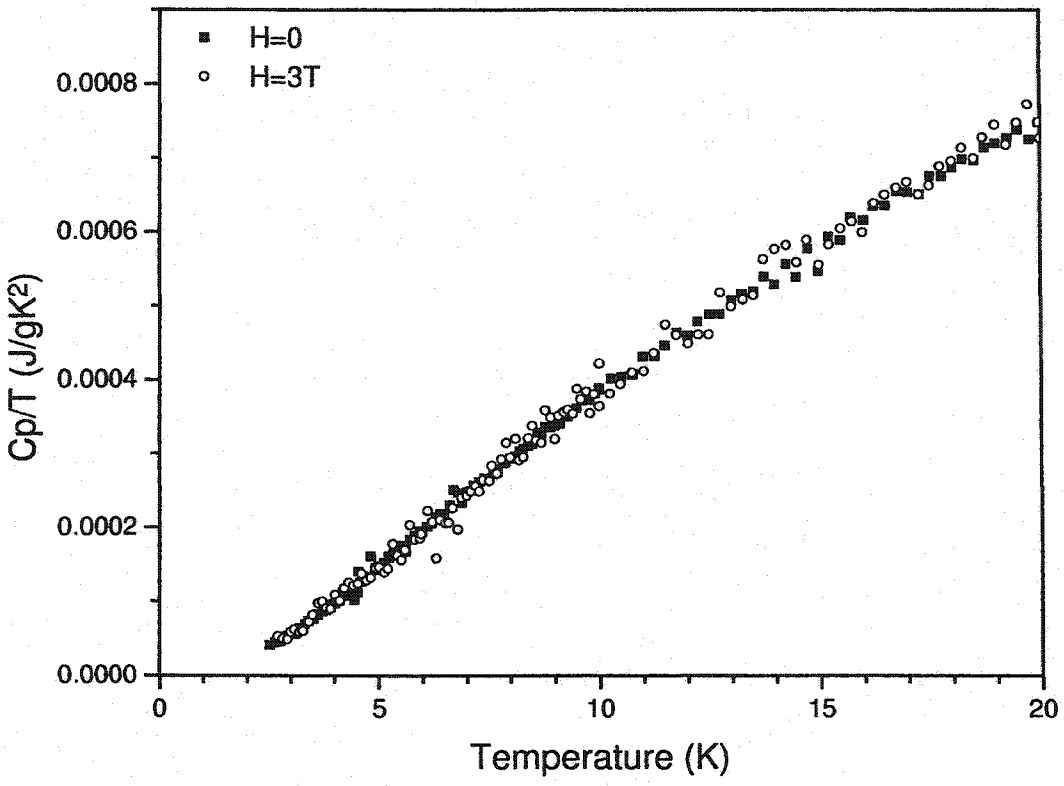

Figure 5.30: The ratio of specific heat over temperature of stage-5 $NiBr_2$-GIC plotted against temperature. Data are shown for applied fields of zero and 3 T.

Chapter 6
Analysis and Discussion

6.1 Simulation of Compounds

In 1963, Lines[82, 83] modeled the transition temperature of $CoCl_2$ and $NiCl_2$ by using a Green's function approach. This method was used because molecular field theory (MFT) had proven to be unsatisfactory for these compounds for several reasons. First, there is no dependence on anisotropy in the MFT result, $k_B T_N = 2(J+J')S(S+1)$. Secondly, the transition temperatures found from the MFT result were significantly larger than the actual Néel temperatures of the materials. Finally, and most importantly for our considerations, MFT predicts a linear drop of T_N with decreasing inter-plane interaction, with a finite result for $J' = 0$. Clearly, this is in error: if the inter-plane interaction is eliminated, there is no three-dimensional coupling of the magnetic atoms. Without these three-dimensional interactions, there can be no three-dimensional ordering, thus T_N must go to zero.

Lines' model made improvements in all of these areas. The calculated Néel temperature was significantly reduced compared to the MFT results and went to zero very quickly for low values of J'. The results also had a dependence, however small,

on the anisotropy of the system. When the results were compared to the actual compounds, it was found that the Néel temperatures were still overestimated, but that they were much closer than the MFT results. Lines' model will be used to get an estimate of the upper limit on the Néel temperature that might be expected in the bromide-GICs.

6.1.1 Lines' Model

The model is a Green's function approach whereby the correlations between neighbouring spins within the same plane and on different planes are calculated. The average value of S_z is calculated and the Néel temperature is determined by the point at which that average goes to zero. The calculation involves a lattice sum including nearest neighbour interactions only. The lattice being considered is that of the pristine chlorides, but this serves as a good approximation to the lattice for $CoBr_2$ and is the same as the lattice for $NiBr_2$. As an approximation, it is assumed that this will also describe the magnetic lattice of the GICs.

The exchange Hamiltonian used in the model is

$$\mathcal{H} = \sum_{nn}[-J\mathbf{S_i}\cdot\mathbf{S_j} + D_1 S_{ix}S_{jx}] + \sum_{nnn}[J'\mathbf{S_i}\cdot\mathbf{S_j} - D_2 S_{ix}S_{jx}] \qquad (6.1)$$

where the sums are over nearest and next-nearest neighbour spins, S_i and S_j. The x-axis is chosen to be the c-axis of the hexagonal lattice, the z-axis along the direction of preferred spin orientation and the y-axis completes the orthogonal set. D_1 and D_2

are the anisotropy parameters.

The motion of the functions $\langle\langle S_{gx}; f(S_h)\rangle\rangle$ and $\langle\langle S_{gy}; f(S_h)\rangle\rangle$ is studied. Here, the double angle brackets represent the Fourier Transform of the Green's Function involving the two Heisenberg operators enclosed. S_{gx} and S_{gy} refer to the x and y components of the spin on lattice g at time t and $f(S_h)$ is any of the three spin components S_{hx}, S_{hy} and S_{hz} on lattice h at time t'.

The equations of motion for the Fourier Transforms are

$$E\langle\langle S_{gx}; f(S_h)\rangle\rangle = \frac{\delta_{gh}}{2\pi}\langle F_1\rangle + i\langle\langle(\sum_{nnn}^{j} J' - \sum_{nn}^{j} J)(S_{gz}S_{jy} - S_{gy}S_{jz}); f(S_h)\rangle\rangle$$

and

$$E\langle\langle S_{gy}; f(S_h)\rangle\rangle = \frac{\delta_{gh}}{2\pi}\langle F_2\rangle + i\langle\langle(\sum_{nnn}^{j} J' - \sum_{nn}^{j} J)(S_{gx}S_{jz} - S_{gz}S_{jx}); f(S_h)\rangle\rangle + i\langle\langle(\sum_{nnn}^{j} D_2 - \sum_{nn}^{j} D_1)S_{gz}S_{jx}; f(S_h)\rangle\rangle$$

where $\sum_{nn}^{j}$ means that j should be summed over all nearest neighbours of g and the single angle brackets represent a canonical average. F_1 and F_2 are the commutators

$$F_1 = [S_{gx}, f(S_g)] \quad \text{and} \quad F_2 = [S_{gy}, f(S_g)]$$

These equations are then decoupled. Because, in the antiferromagnetic state, adjacent layers align in alternate directions, the system is split into two sublattices, 'up' and 'down'. This allows for the definition of four separate Green's functions, which are Fourier transformed with respect to the reciprocal lattice and the functions G_{iK} defined as follows:

with **g** and **h** on the same sublattice,

$$\begin{aligned}
\langle\langle S_{gx}; f(S_h)\rangle\rangle &= \frac{2}{N}\sum_K G_{1K} e^{i\mathbf{K}\cdot(\mathbf{g}-\mathbf{h})} \\
G_{1K} &= \sum_{g-h}\langle\langle S_{gx}; f(S_h)\rangle\rangle e^{-i\mathbf{K}\cdot(\mathbf{g}-\mathbf{h})} \qquad (6.2) \\
\langle\langle S_{gy}; f(S_h)\rangle\rangle &= \frac{2}{N}\sum_K G_{3K} e^{i\mathbf{K}\cdot(\mathbf{g}-\mathbf{h})} \\
G_{3K} &= \sum_{g-h}\langle\langle S_{gy}; f(S_h)\rangle\rangle e^{-i\mathbf{K}\cdot(\mathbf{g}-\mathbf{h})} \qquad (6.3)
\end{aligned}$$

and with **g** and **h** on different sublattices,

$$\begin{aligned}
\langle\langle S_{gx}; f(S_h)\rangle\rangle &= \frac{2}{N}\sum_K G_{2K} e^{i\mathbf{K}\cdot(\mathbf{g}-\mathbf{h})} \\
G_{2K} &= \sum_{g-h}\langle\langle S_{gx}; f(S_h)\rangle\rangle e^{-i\mathbf{K}\cdot(\mathbf{g}-\mathbf{h})} \qquad (6.4) \\
\langle\langle S_{gy}; f(S_h)\rangle\rangle &= \frac{2}{N}\sum_K G_{4K} e^{i\mathbf{K}\cdot(\mathbf{g}-\mathbf{h})} \\
G_{4K} &= \sum_{g-h}\langle\langle S_{gy}; f(S_h)\rangle\rangle e^{-i\mathbf{K}\cdot(\mathbf{g}-\mathbf{h})} \qquad (6.5)
\end{aligned}$$

Using the definition of the Kronecker delta function and writing the average value of S_z on an up lattice site as $\bar{S}$ and on a down lattice site as $-\bar{S}$, the equations of motion are rewritten in terms of the G_{iK}.

$$EG_{1K} = (1/2\pi)\langle F_1\rangle + i\bar{S}(\lambda G_{4K} + \mu G_{3K}) \qquad (6.6)$$

$$EG_{2K} = -\bar{S}(\lambda G_{3K} + \mu G_{4K}) \qquad (6.7)$$

$$EG_{3K} = (1/2\pi)\langle F_2\rangle - i\bar{S}[(\lambda - \rho_2)G_{2K} + (\mu + \rho_1)G_{1K}] \qquad (6.8)$$

$$EG_{4K} = i\bar{S}[(\lambda - \rho_2)G_{1K} + (\mu + \rho_1)G_{2K}] \qquad (6.9)$$

where

$$\lambda = \sum_{nnn} J' e^{i\mathbf{K}\cdot\mathbf{l}} \tag{6.10}$$

$$\mu = z_1 J + z_2 J' - \sum_{nn} J e^{i\mathbf{K}\cdot\mathbf{l}} \tag{6.11}$$

$$\rho_1 = \sum_{nn} D_1 e^{i\mathbf{K}\cdot\mathbf{l}} \tag{6.12}$$

$$\rho_2 = \sum_{nnn} D_2 e^{i\mathbf{K}\cdot\mathbf{l}} \tag{6.13}$$

Here, $\mathbf{l}$ is the vector joining the nearest or next nearest neighbours.

This set of equations can be solved for G_{iK} and, using the properties of the Green's function, expressions for the correlation functions involving the various spin operators can be determined. In so doing, it is found that

$$\langle S_x^2 \rangle = (\bar{S}/4)\langle A_1 \coth(E_1/2k_BT) + A_2 \coth(E_2/2k_BT)\rangle_K$$

$$\langle S_y^2 \rangle = (\bar{S}/4)\langle A_1^{-1} \coth(E_1/2k_BT) + A_2^{-1} \coth(E_2/2k_BT)\rangle_K$$

$$\text{and} \quad \langle S_x S_y - S_y S_x \rangle = i\bar{S}$$

where $\langle \cdots \rangle_K$ denotes an average over the N/2 allowed values of $\mathbf{K}$ in the first Brillouin zone. In this notation,

$$A_1^2 = \frac{\mu + \lambda}{\mu - \lambda + \rho_1 + \rho_2}$$

$$A_2^2 = \frac{\mu - \lambda}{\mu + \lambda + \rho_1 - \rho_2}$$

$$E_1^2 = (\bar{S})^2(\mu + \lambda)(\mu - \lambda + \rho_1 + \rho_2)$$

$$E_2^2 = (\bar{S})^2(\mu - \lambda)(\mu + \lambda + \rho_1 - \rho_2)$$

Now, $S_x^2 + S_y^2 + S_z^2 = S(S+1)$, thus

$$\langle S_z^2 \rangle = S(S+1) - (\bar{S}/4)(P+Q)$$

where

$$\begin{aligned} P &= \langle A_1 \coth(E_1/2k_BT) + A_2 \coth(E_2/2k_BT) \rangle_K \\ Q &= \langle A_1^{-1} \coth(E_1/2k_BT) + A_2^{-1} \coth(E_2/2k_BT) \rangle_K \end{aligned}$$

and, in the case of S=1/2, S_z^2=1/4, so

$$\bar{S} = 2/(P+Q) \quad (S = 1/2) \tag{6.14}$$

In a similar fashion, using higher order terms, the relationship for S=1 is

$$\bar{S} = 4(P+Q)/(4 + P^2 + Q^2 + PQ) \quad (S = 1) \tag{6.15}$$

At temperatures very close to but below T_N, $\coth(E_i/2k_BT)$ is replaced by $2k_BT/E_i$ and the expressions for P and Q are changed accordingly. If we then solve for T_N, we find

$$k_BT_N = 1/(U+V) \qquad (S = 1/2) \tag{6.16}$$

$$k_BT_N = 2(U+V)/(U^2 + UV + V^2) \quad (S = 1) \tag{6.17}$$

where

$$\begin{aligned} U &= \bar{S}\langle (A_1/E_1) + (A_2/E_2) \rangle_K \\ &= \langle 1/(\mu - \lambda + \rho_1 + \rho_2) + 1/(\mu + \lambda + \rho_1 - \rho_2) \rangle_K \end{aligned} \tag{6.18}$$

$$\begin{aligned} V &= \bar{S}\langle (1/A_1E_1) + (1/A_2E_2) \rangle_K \\ &= \langle 1/(\mu - \lambda) + 1/(\mu + \lambda) \rangle_K \end{aligned} \tag{6.19}$$

The magnetic lattice considered by Lines was that of $CoCl_2$ (or $NiCl_2$). This is also the lattice structure of $NiBr_2$ and similar to that of $CoBr_2$, so we shall follow the same procedure. The magnetic unit cell, therefore, is rhombohedral. We shall describe it with the lattice vectors $\mathbf{i}$,$\mathbf{j}$ and $\mathbf{k}$, which point from one magnetic atom to its three nearest neighbours in an adjacent plane, and assume that the total volume of the crystal is L^3. Using periodic boundary conditions, the reciprocal lattice vectors are

$$\mathbf{K} = (2\pi/L)(n_1\mathbf{b_1} + n_2\mathbf{b_2} + n_3\mathbf{b_3})$$

where $\mathbf{b_i}$ are the basis vectors of the reciprocal lattice and n_i are integers such that $-L/2 \leq n_i \leq L/2$. Defining $K_i = 2\pi n_i/L$, we find that for nearest neighbours,

$$\sum_{nn} e^{i\mathbf{K}\cdot\mathbf{l}} = e^{i\mathbf{K}\cdot(\mathbf{i}-\mathbf{j})} + e^{i\mathbf{K}\cdot(\mathbf{i}-\mathbf{k})} + e^{i\mathbf{K}\cdot(\mathbf{j}-\mathbf{k})} + e^{i\mathbf{K}\cdot(\mathbf{j}-\mathbf{i})} + e^{i\mathbf{K}\cdot(\mathbf{k}-\mathbf{i})} + e^{i\mathbf{K}\cdot(\mathbf{k}-\mathbf{j})}$$

but

$$\mathbf{K}\cdot(\mathbf{i}-\mathbf{j}) = \frac{2\pi}{L}(n_1 - n_2) = K_1 - K_2$$

and after simplification, we find

$$\sum_{nn} e^{i\mathbf{K}\cdot\mathbf{l}} = 2[\cos(K_1 - K_2) + \cos(K_2 - K_3) + \cos(K_3 - K_1)] \tag{6.20}$$

Similarly, for next nearest neighbours, we find

$$\sum_{nnn} e^{i\mathbf{K}\cdot\mathbf{l}} = 2[\cos(K_1) + \cos(K_2) + \cos(K_3)] \tag{6.21}$$

Defining $c_i = \cos(K_i)$ and $s_i = \sin(K_i)$, and using the symmetry of the lattice, we find

$$U = \left\langle 2 \Big/ \left\{ 6(J+J') - (J-D_1) \left[\left(\sum_i c_i \right)^2 + \left(\sum_i s_i \right)^2 - 3 \right] \right.\right.$$
$$\left.\left. \pm 2(J'-D_2) \left(\sum_i c_i \right) \right\} \right\rangle_K \qquad (6.22)$$

$$V = \left\langle 2 \Big/ \left\{ 6(J+J') - J \left[\left(\sum_i c_i \right)^2 + \left(\sum_i s_i \right)^2 - 3 \right] \right.\right.$$
$$\left.\left. \pm 2J' \left(\sum_i c_i \right) \right\} \right\rangle_K \qquad (6.23)$$

These lattice averages are then computed and used with equations (6.16) and (6.17) to calculate T_N for the compounds considered. Because of the symmetry in the lattice average, either the + or - for the last term in equations (6.22) and (6.23) can be used as long as it is used consistently throughout the average.

6.1.2 Simulation Results

Lines' simulations were repeated with an emphasis on the low inter-plane interaction strength region, which is the region of relevance to this work. In order to verify that the modeling was done correctly, simulations were run with varying lattice size to determine an optimum size. It was found, as shown in figure 6.1, that larger lattices gave results much closer to the original work than did smaller lattices. With processing time as a constraint, lattices of 100 points per side were used. Sizes smaller than 50 points resulted in significantly different results than those found by Lines. The difference between 50 points and 100 points was relatively small and going to larger lattices did not change the results enough to warrant the extra processing time, given

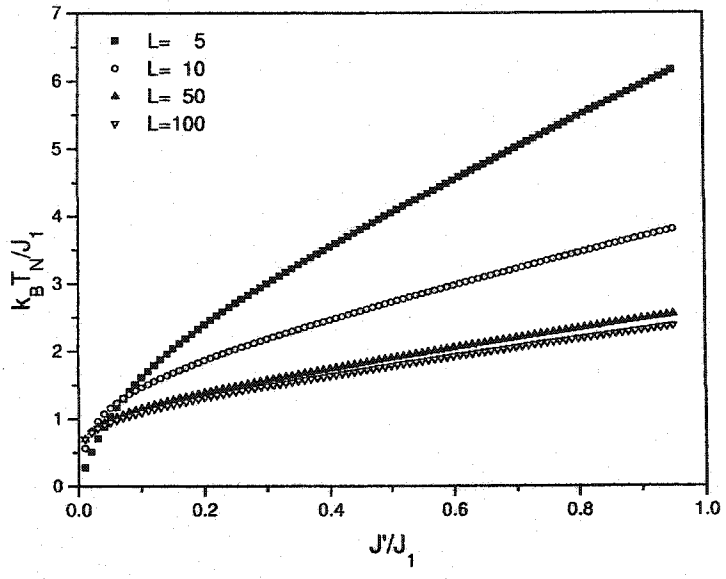

Figure 6.1: Simulations based on Lines' Green's function method varying the lattice size.

that the numbers were only to be used as a guide. In all simulations, the anisotropy terms, D_i, were set to zero since their contribution to T_N was found to be small. If the anisotropies are included, the value for T_N is increased by <15%, which is small for the results here, given that this is only to be used as an estimate of an upper limit.

The results for the simulation are shown in figures 6.2 and 6.3 . The spin-1/2 model can be compared to $CoBr_2$-GIC and the spin-1 to $NiBr_2$-GIC. It should be noted that this model takes into account only nearest neighbour interactions in-plane and between planes. It has been seen that second- and third-near neighbours are important in the determination of the phases of both $CoBr_2$ and $NiBr_2$, but the results should, nonetheless, provide some guidance as to reasonable transition temperatures.

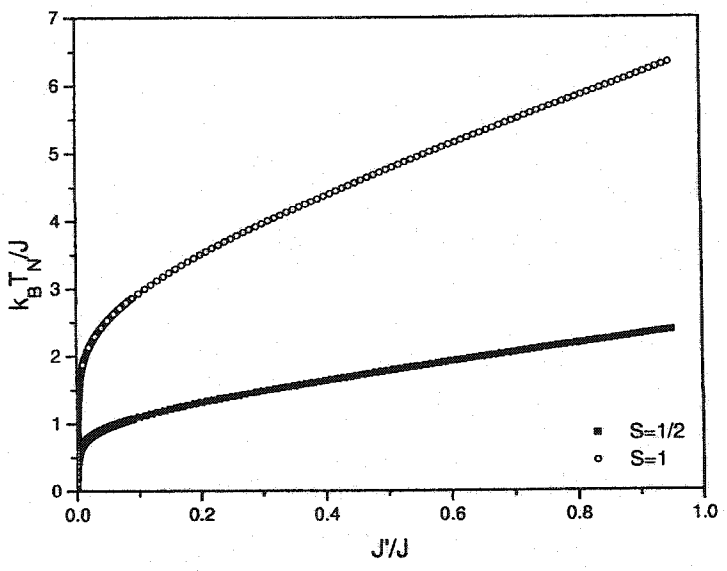

Figure 6.2: Simulations based on Lines' Green's Function method in high interaction ratio region. The S=1/2 curve can be compared to $CoBr_2$ and the S=1 curve to $NiBr_2$.

Figure 6.2 shows the region of high inter-plane interaction relative to in-plane interaction. This is the area of interest for the pristine compounds. $CoBr_2$ has a ratio, J'/J_1=0.483[9] and effective spin-1/2. From figure 6.2, this corresponds to a value of $k_B T_N/J_1$ of 1.8. For $CoBr_2$, J_1/k_B=23.33 K, so T_N=42 K. This is very much an overestimate, since T_N=19 K for $CoBr_2$. Similar analysis for $NiBr_2$, using the S=1 curve gives T_N=51 K, close to, but still higher than, the actual value of 44.6 K.

Figure 6.3 shows the region of low inter-plane interaction, which should more accurately represent the GICs. Estimating the interaction ratio to be $\sim 10^{-4}$, as seen in the chloride-GICs, using the values of J_1 determined for pristine $CoBr_2$ (J_1/k_B=23.3

K[9]) and $NiBr_2$(J_1/k_B=18.1 K[27]) and from figure 6.3 we find $T_N \approx$2 K for $CoBr_2$-GIC and 4 K for $NiBr_2$-GIC. These values are both consistent with our experimental results. If we assume that this model overestimates the Néel temperature, as was the case for the pristine compounds, the transition, if any, should occur below 2 K for $CoBr_2$. The value of T_N=4 K determined for $NiBr_2$ is slightly lower in temperature than the peak in χ_{dc} for the $NiBr_2$-GICs. However, the temperature predicted by this model, T_N, is for three-dimensional antiferromagnetic ordering. The peak in the dc susceptibility is believed to be associated with two-dimensional ordering, which is not studied by these simulations. As in the chloride-GICs, two-dimensional ordering should occur at a higher temperature than three-dimensional ordering, which does not occur at temperatures as low as 2 K.

If, however, the values for J'/J determined from the magnetization curves later in this chapter are used in this analysis, the estimated values of T_N are increased. The values determined for the exchange ratio are of the order 10^{-3}, giving values of T_N estimated from figure 6.3 of 8-14 K for $CoBr_2$-GIC and 18-25 K for $NiBr_2$-GIC. From these estimates, one might expect to see ordering at temperatures higher than presently observed. However, in the case of $CoBr_2$, Lines' model still overestimates T_N by a factor of more than 2. Given that the model does not incorporate interactions other than nearest neighbours or the domain nature of the material, it is perhaps reasonable that three dimensional ordering is not seen down to 2 K. In particular, Lines' model does show that, as the inter-plane interaction is reduced, the ordering

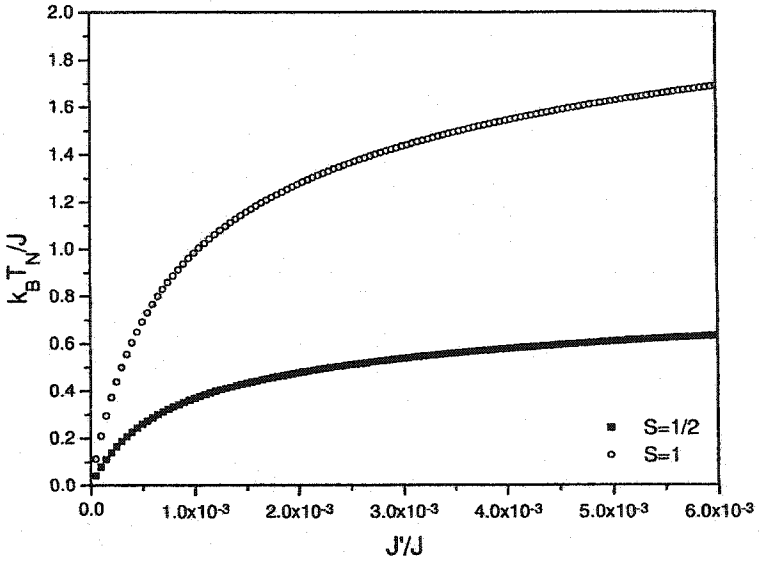

Figure 6.3: Simulations based on Lines' Green's Function method in the low interaction ratio region.

temperature should decrease quickly.

Unfortunately, comparison to $FeBr_2$ is not valid. This model assumes a continuous in-plane symmetry, whereas the iron moments aligned along the c-axis have an Ising symmetry. Some work has been done for $FeCl_2$ using the Bethe-Peierls technique[84], but the results did not give quantitative comparisons for transition temperature as does the Lines method. Monte Carlo simulations would likely give better quantitative results, but such an undertaking is not within the scope of this study. Clearly, the most difficult task is to fully understand the role played by the graphite layers separating the intercalant layers. A full model must also take into

account finite size intercalant domains and interactions among the domains in order to determine whether there is ordering within domains and to observe any glassy phase.

6.2 $CoBr_2$

The high temperature dc susceptibility data for each of the compounds was analyzed by fitting to a Curie-Weiss law, $\chi = \frac{C}{T-\theta_{CW}}$. This is done by plotting $1/\chi$ against temperature and fitting a straight line to the data. From the slope and the intercept, the Curie constant, C, and the Curie-Weiss temperature, θ_{CW}, can be determined. Only the data corresponding to T>100 K is used in these fits. This is because the Curie-Weiss law is, in general, only obeyed for $T \gg |\theta_{CW}|$.

The Curie constant is related to the number of moments in the sample and the effective moment per ion according to equation (1.2), $C = N\mu_0(p_{eff}\mu_B)^2/3k_B$. Because the number of moments in each sample is not known, we shall assume that the effective moment remains unchanged from that of the pristine intercalant, as evidenced by the work with the chloride-GICs, to obtain an estimate for the number of moments contributing to the susceptibility.

The result of such a fit for the stage-1 $CoBr_2$-GIC sample is shown in figure 6.4. Only the high-temperature ($T \geq 100$ K) susceptibility data are used in the fit because

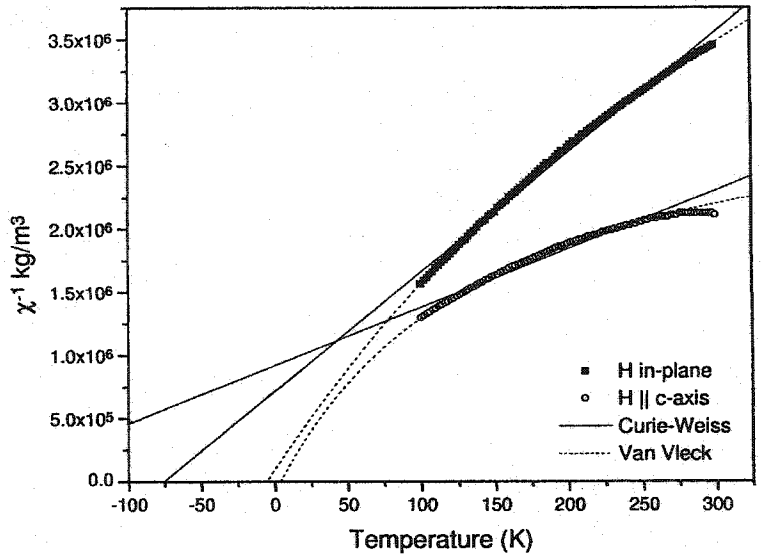

Figure 6.4: Fits to the high temperature dc susceptibility data for stage-1 $CoBr_2$-GIC. The solid line is a standard Curie-Weiss fit to the data and the dashed curve is modified with a temperature-independent term. Both the in-plane and c-axis susceptibilities are shown.

this is the region where the Curie-Weiss law would be expected to fit best. There is a strong deviation from linearity in the in-plane susceptibility. The parameters for the fit were determined to be C=1.057±0.008×10^{-4} K·m^3/kg and θ_{CW}=-75±2 K. The negative value for θ_{CW} indicates that the dominant magnetic interaction in the compound is antiferromagnetic.

The Curie-Weiss fit was modified to include a temperature-independent susceptibility,

$$\chi = \chi_0 + \frac{C}{T - \theta_{CW}} \tag{6.24}$$

where χ_0 is the temperature-independent van Vleck susceptibility. The results are

shown by the dashed lines in figure 6.4. This fits the non-linearity of the data extremely well. The values determined for θ_{CW} and C through this fit have the same interpretation as those in the standard Curie-Weiss fit. The Curie constant from the in-plane data is found to be $5.64 \pm 0.04 \times 10^{-5}$ K·m^3/kg, roughly half of the value determined without the constant term. The number of moments estimated from this value using equation (1.2) is $3.0 \pm 0.1 \times 10^{18}$.

A theoretical maximum packing density of the intercalant in the graphite host compound is determined by comparing the in-plane areas of the unit cells of graphite and intercalant. For the case of $CoBr_2$-GIC, the ratio of the area of one carbon atom to the area of one $CoBr_2$ molecule tells us that the maximum packing density is one $CoBr_2$ molecule for every 3.6 C atoms in a stage-1 compound. For higher stages, this number is simply scaled by the stage index. Given the domain nature of the intercalant layers, the actual packing density must be lower than this theoretical determination. Filling factors of 60 - 80 % of the maximum have been obtained in other metal-halide GICs.

The filling factor for this sample is found to be $\approx$10%. This is determined by finding the mass associated with the number of $CoBr_2$ molecules estimated above. This mass is subtracted from the total mass of the sample, the difference being the mass of graphite, from which the number of carbon atoms is calculated. The ratio of these two numbers is compared to the maximum packing density to determine the

filling factor.

It should be noted that the filling factor above is determined assuming that the number of moments calculated from the Curie constant is equal to the number of Co atoms in the sample and that the effective moment of these atoms is unchanged from that of the pristine material.

From the fit shown in figure 6.4, θ_{CW} is determined to be -5.6±0.5 K. This value is more reasonable than that determined using the standard Curie-Weiss fit in that it should be close to but somewhat more positive than -20 K, the value for pristine $CoBr_2$. Other authors have found that the value of θ_{CW} in the chloride-GICs did not change significantly from that of the pristine form of the intercalant. An increase in the temperature is expected in this case because the antiferromagnetic interactions are weakened relative to those in pristine $CoBr_2$ by the increased separation of the magnetic layers caused by the graphite layer.

The value determined for χ_0 is $1.03\pm0.01 \times 10^{-7}$ m^3/kg. The need for this temperature-independent susceptibility is echoed in the magnetization curve. Rather than saturating to a constant value at high fields, the magnetization maintains a small, constant increase with applied field, indicating a finite susceptibility. This is characteristic of a van Vleck paramagnetism.

This type of paramagnetism has been seen in several of the magnetic metal-

halides and their intercalation compounds[4, 63, 66, 81] and is typically of order 10^{-7} m^3/mol. Using the value determined for χ_0 from the fit above and assuming the number of moments determined from that fit to be correct, a value of 7.8×10^{-8} m^3/mol is found. This is similar to the values obtained for related materials and indicates that this is a likely cause of the deviation from the usual Curie-Weiss law.

The c-axis measurements were also re-analyzed, incorporating the van Vleck term, χ_0 in equation 6.24. The resultant fit gives C=4.53±0.07 $\times$ 10^{-5} K·m^3/kg, θ_{CW}=4±1 K and χ_0=3.02±0.02 $\times$ 10^{-7} m^3/kg. The value for the van Vleck term is three times higher than that determined from the in-plane measurement, although still of the same order. The value for θ_{CW} is much more reasonable than without the van Vleck correction and an anisotropy still exists in the Curie constant, with $C_{\|}/C_{\perp}$=1.25.

The high temperature dc susceptibility of the stage-2 $CoBr_2$-GIC was fit in a similar fashion. The obvious non-linearity of the χ^{-1} plot again indicates that a modified Curie-Weiss fit is required. This fit is show in figure 6.5 and compared to the usual Curie-Weiss fit. By including the van Vleck term, C is found to be 3.9±0.2 $\times$ 10^{-6} K·m^3/kg, θ_{CW}=21±3 K and χ_0=3.40±0.07 $\times$ $10^{-8}$$m^3$/kg.

In increasing the stage index from one to two, changes are expected. The separation between the magnetic layers is increased and, as a result, the strength of

the interaction between these planes is decreased. This should lead to a higher value of θ_{CW} since this reflects, in a way, the type and size of the magnetic interactions in the sample. θ_{CW} increases from -5.6 to 21 K in going from stage 1 to stage 2. The positive value implies that ferromagnetic interactions are now dominant over the antiferromagnetic ones. This is to be expected since the inter-plane interactions should become weaker with increasing stage. The value of C should decrease since the number of moments is decreasing relative to the number of carbon atoms. This change is expected to be near a factor of 2 since the number of graphite planes between intercalant layers is doubled. The actual change in C is a decrease by a factor of almost 15.

The saturation magnetization is determined from the magnetization curve by fitting a line to the linear high-field region and extrapolating back to H=0. If we examine the Brillouin function in equation (1.5), we find that there should be little or no change in the magnetization in the high-field region, where $\mu\mu_0 H/k_B T \gg 1$. Extrapolation back to H=0 therefore yields a reasonable estimate of the zero-temperature saturation field. The positive slope of the high-field region in many of the magnetization curves presented is caused by the temperature-independent van Vleck term. This is because van Vleck paramagnetism does not saturate as does the contribution from conventional paramagnetism. The saturation field, determined to be the field at which the maximum curvature in the magnetization plot occurs, is related to the interaction strength by equation (1.6), $J' = g\mu_B\mu_0 H_{sat}/2z'S$.

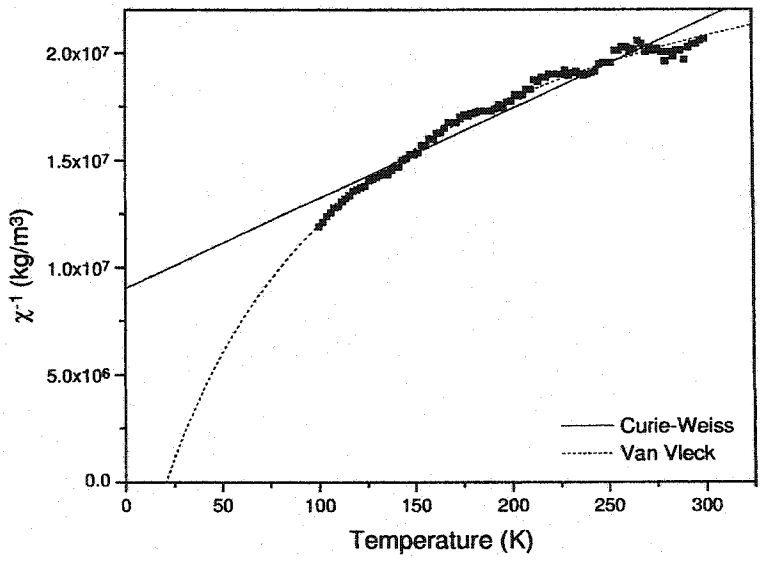

Figure 6.5: Fits to the high temperature dc susceptibility data for stage-2 $CoBr_2$-GIC. The solid line is a standard Curie-Weiss fit to the data and the dashed curve is modified with a temperature-independent term.

The magnetization curve for stage-1 $CoBr_2$-GIC(see figure 5.4) has a saturation magnetization of M_{sat}=13.90±0.03 A·m^2/kg with a saturation field, H_{sat}=6±0.5×10^5 A/m. The positive slope in the high-field region, attributed to van Vleck paramagnetism has a value of 4.38±0.10 × 10^{-7} m^3/kg. From the saturation magnetization, another estimate of the number of moments can be made using equation (1.4), $M_{sat} = N\mu$, and assuming a moment $\mu = 3.0\mu_B$ as in the pristine compound. In this way, the number of moments is calculated as 1.90×10^{18}, lower than the value of 3.0×10^{18} estimated from the susceptibility.

The saturation field is used to estimate the strength of the inter-plane interactions. Using equation (1.6), and again assuming $\mu = 3.0\mu_B$, a value of $J'z'/k_B$=-3.0 K is obtained. If z'=2 is used, this gives a high value of J'/k_B=-1.5K, whereas if the 20 equivalent exchange paths from the pristine compound are considered, this value drops to -0.15 K. This is compared to -11.6 K for pristine $CoBr_2$[9]. If the in-plane interaction remains the same, which is a reasonable assumption based on the work done with the chloride-GICs, then we find a ratio -J'/J$_1$ ≈ 6×10^{-3}. This is high compared to values of 10^{-3} estimated for the stage-1 chloride compounds[59].

The stage-2 $CoBr_2$ sample has a magnetization curve(figure 5.9) which is qualitatively very similar to the stage-1 sample. While the saturation field remains the same, the saturation magnetization is reduced to 1.67±0.01 A·m^2/kg and the van Vleck paramagnetic contribution to 3.4±0.1 × 10^{-8} m^3/kg. The fact that H_{sat} re-

mains the same as in the stage-1 compound implies that the inter-plane interaction is the same strength. This is counter-intuitive given that the planes are separated by an extra layer of graphite. This is also contradictory to the susceptibility data, which show that θ_{CW} increases significantly in stage-2 compared to stage-1, indicating that the inter-plane antiferromagnetic coupling is much weaker.

The magnetization curves for both stages of $CoBr_2$-GIC were also analyzed by fitting to a Brillouin function. The Brillouin function from equation (1.5) was modified to include a constant term representing the van Vleck contribution. The parameters N, μ and χ_0 were all allowed to vary in the fit. The fit to the stage-1 compound, shown in figure 6.6, required that $\mu = 4.37 \pm 0.02 \mu_B$, N=$1.22 \pm 0.01 \times 10^{18}$ and χ_0=$6.2 \pm 0.1 \times 10^{-7}$ m^3/kg. When these are compared to the values obtained from extrapolating the high-field region, it is seen that the number of moments is decreased, but that the magnetic moment is significantly higher than that of pristine $CoBr_2$. Thus, below the saturation field, the material behaves as if it consists of fewer magnetic ions, but with a larger moment per ion. This indicates that the interactions among the Co ions play an important role in determining the approach to saturation. χ_0 is close to, but slightly higher than the value determined from the slope of the high field region. The difference here is simply in the number of points considered in the fit since the current fit considers all data points.

The Brillouin fit to the stage-2 $CoBr_2$ magnetization curve is shown in figure

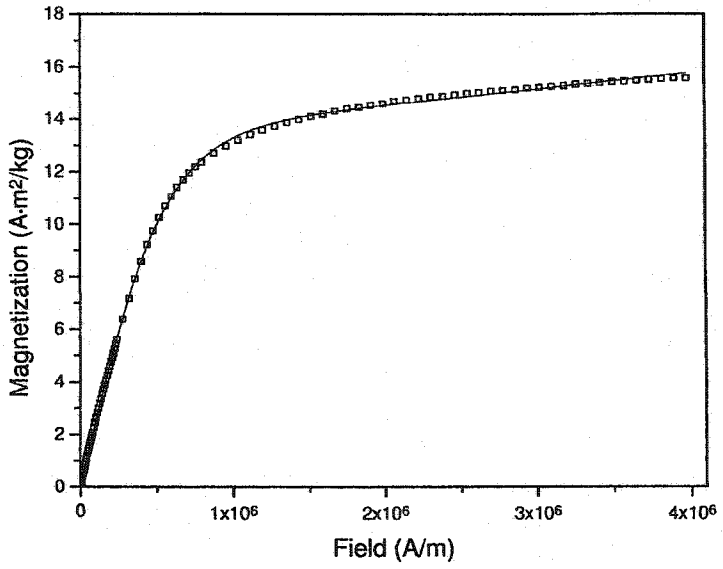

Figure 6.6: Magnetization curve of stage-1 $CoBr_2$-GIC fit to a Brillouin function.

6.7. As in the stage-1 compound, the fit required $\mu = 4.37 \pm 0.07 \mu_B$, with the number of moments reduced to $1.47 \pm 0.02 \times 10^{17}$. χ_0 is $5.2 \pm 0.2 \times 10^{-8}$ m^3/kg, again close to the value determined from the slope.

The ac and dc susceptibilities for $CoBr_2$-GIC show no phase transitions for stages 1 and 2. The lack of features in the susceptibility curves indicates that the materials remain paramagnetic down to 2 K. This is confirmed by the neutron scattering study of the stage-3 compound. There were no magnetic Bragg peaks and no change in the incoherent paramagnetic scattering, both of which indicate that no ordering has taken place. Simulations based on the work of Lines indicate that the antiferromagnetic transition, if it exists, could be at or below 2 K. This is supported

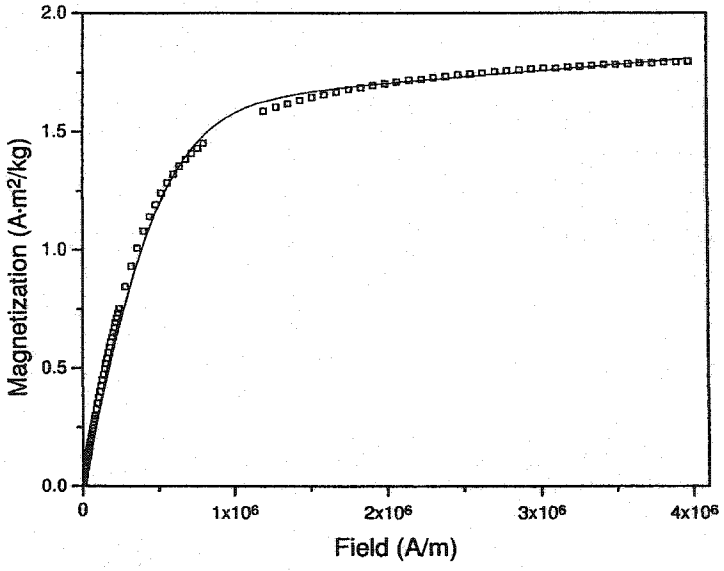

Figure 6.7: Magnetization curve of stage-2 $CoBr_2$-GIC fit to a Brillouin function.

by the small amount of relaxation in the dc susceptibility of the stage-1 compound. Small differences between the ZFC and FC susceptibilities of the chloride-GICs were also seen at temperatures just above T_{cu}, where two-dimensional ordering occurs. The difference could be a precursor to ordering in all of these compounds.

In summary, none of the $CoBr_2$-GICs prepared undergo a magnetic transition at the temperatures studied here. No peaks are seen in the susceptibility measurements and the magnetization curves show no variations in the low-field region which would indicate ordering. Finally, the neutron scattering results indicate that there is no ordering down to 5.5 K in the stage-3 compound.

6.3 $FeBr_2$

Curie-Weiss fitting was performed on the high temperature dc susceptibility of stage-2 $FeBr_2$-GIC as shown in figure 6.8. With the much larger signal from this sample, the standard Curie-Weiss fit appears to be quite good at high temperatures. However, with the addition of the van Vleck term, the fit is improved at temperatures below 100 K. With the van Vleck term, the fit parameters are found to be C=1.35±0.01 × 10^{-4} K·m^3/kg, θ_{CW}=-5.1±0.7 K and χ_0=5.7±0.4 × 10^{-8} m^3/kg. From the value of the Curie constant, and assuming $\mu_{eff} = 5.6\mu_B$ as in the pristine compound, the number of moments is calculated to be 1.73×10^{19}. This would give a C:$FeBr_2$ ratio of 12.5. The maximum packing density calculated for this material is 9.4, giving a filling factor of 75%, which is quite good compared to other metal-halide-GICs.

The magnetization curve for stage-2 $FeBr_2$-GIC is shown in figure 5.16. By extrapolating the high-field linear region back to H=0, M_{sat} is estimated to be 19.39±0.07 A·m^2/kg, with an in-plane saturation field of 1.2±0.1 × 10^6 A/m. From M_{sat} and equation (1.4), we find the number of moments to be $5.5\pm0.1\times10^{18}$, roughly 1/3 the value determined from the Curie-Weiss fit. The slope of the high-field region is 2.41±0.02 × 10^{-6} m^3/kg.

From the saturation field using equation (1.6), we estimate $z'J'/k_B$=-0.75 K. This compares to a value of J'/k_B=-3.7 K for the pristine compound[23]. If J_1/k_B=9.5

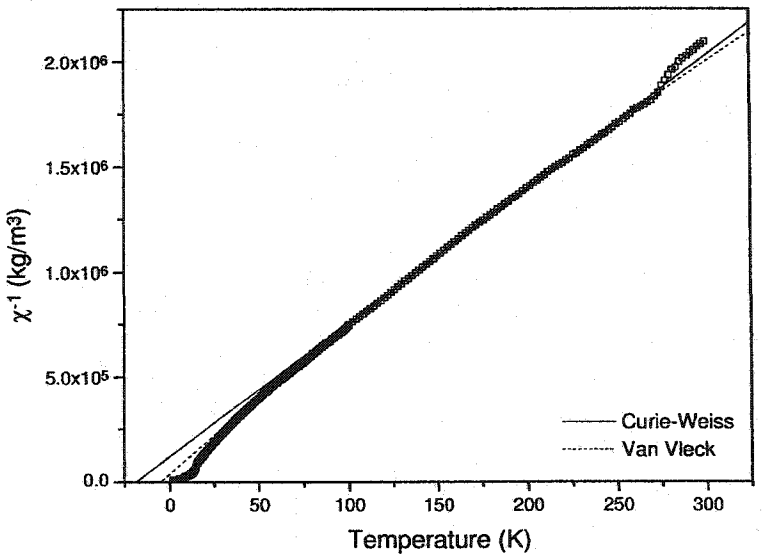

Figure 6.8: Fits to the high temperature dc susceptibility data for stage-2 $CoBr_2$-GIC. The solid line is a standard Curie-Weiss fit to the data and the dashed curve is modified with a temperature-independent term.

K is assumed as in the pristine compound, and $z'=20$, we find $-J'/J_1 \approx 4\times10^{-3}$. This is higher than expected based on the results of the chloride compounds, which have estimated values of $\approx 10^{-4}$[56, 61, 64].

The specific heat of stage-2 $FeBr_2$-GIC, shown in figure 5.20, has a broad peak at 8.5 K, which can be removed by the application of a strong (3T) magnetic field. Since the peak is decreased by an applied field, it is concluded that it indicates magnetic ordering. The temperature matches the peak in the ac susceptibility and the step in the dc susceptibility measurement. Since there is no other peak in the specific heat, the ordering which occurs at higher temperature must be of short range. The temperature region above 10 K is linear, indicating a T^3 dependence in this region. In the low temperature region (<4K), analysis shows that the specific heat is quadratic in temperature, characteristic of a two-dimensional lattice.

The high-field (3 T) specific heat measurement is taken at a field in the linear region of the magnetization curve, indicating that at this field the sample is approximately saturated. This means that there should be no magnetic contribution to the specific heat at this field. The magnetic contribution to the zero-field specific heat can therefore be calculated by subtracting the high-field specific heat from the zero-field specific heat. The plot of this difference is shown in figure 6.9. The solid curve in the figure is a fit to two Gaussian peaks, shown individually by the dashed curves. The Gaussian is used merely as a convenience for estimating the area under the curve and

to illustrate the presence of two peaks in the data.

The sharper of the peaks, at 8.5 K, corresponds to ordering within individual domains at this temperature. Given the small amount of entropy change associated with this peak, it is unlikely that this is complete three-dimensional ordering within the domains, but rather long-range ferromagnetic ordering within the planes of domains, without three-dimensional ordering.

The broad peak, centered at approximately 7 K, is most likely associated with the glassy transition. Typically, specific heat measurements of spin glasses do not have a sharp peak at the freezing temperature, but rather a broad peak at a temperature significantly higher than the freezing temperature.

The change in entropy associated with the magnetic ordering is calculated from

$$\mathcal{S} = \int_0^T \frac{C}{T} \mathrm{d}T \tag{6.25}$$

The change in entropy is $6.8 \pm 0.2 \times 10^{-4}$ J/g·K. Taking the number of moments to be 1.73×10^{19}, as found from the modified Curie-Weiss fit, this represents a change in entropy of only $0.075 \pm .002$ J/mol·K. One would expect a value of $\mathcal{S} = Nk_B \ln(2S + 1) = 13.4$ if the sample were ordered completely during this transition. The theoretical value is also close to the value found by Brade and Yates[20] for pristine $FeBr_2$. The large difference is indicative of a high degree of frustration in the low temperature (T

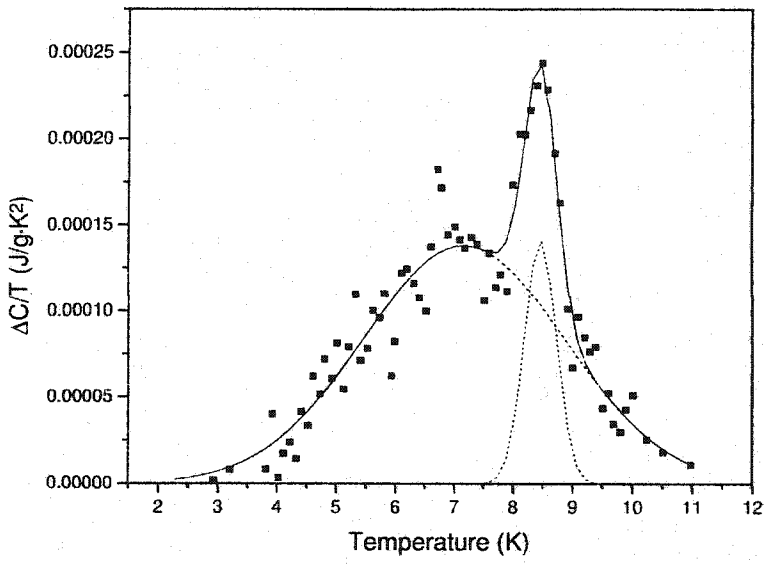

Figure 6.9: Difference between zero field and high-field specific heat measurements near the peak at 8.5 K.

<3 K) state. This is due not only to disorder among domains, but also to incomplete 3D ordering within individual domains.

From the low temperature susceptibility of the stage-2 $FeBr_2$-GIC, a number of transitions are apparent. In the plot of χ_{dc}(figure 5.13), there are three features indicative of three separate transitions. A step at 14.5 K shows an increase in ordering at this point as does the step at 8.5 K. Further, the peak in the ZFC measurement at 3 K shows a third transition. The FC measurement does not have a peak at this lowest temperature, but there is a change in slope here. There is a remanent magnetization which begins to appear slightly above the 14.5 K step in low field measurements and

decreases in magnitude with increasing applied field(figure 5.14). With an applied field of 100 Oe, the remanent field has disappeared above the 3 K peak. Below 3 K, the FC magnetization becomes flat as the field is increased, with the susceptibility decreasing. Furthermore, the steps at the higher temperatures decrease in size and disappear with the application of a 100 Oe field.

While the dc susceptibility data do not, in and of themselves, indicate the exact nature of the transitions, they are suggestive. There is a large remanent field and history dependence at low temperatures. The shape of the susceptibility curves in this region indicates that the transition at 3 K is likely either one to an antiferromagnetic state or to a glassy state. For confirmation, ac susceptibility measurements are examined.

The ac susceptibility also has three features(see figure 5.17), which correspond to the three transitions seen in the dc measurements. In χ', there are a shoulder at 14.5 K, a smaller shoulder at 8.5 K and a large peak at 4.5 K. There are also three peaks in the absorption, χ'', corresponding to the three peaks above. The largest peak is the low temperature one, which begins to rise sharply at the peak in χ', so that it is at a slightly lower temperature. This is consistent with a phase transition in which the relaxation time of the system increases sharply at the transition point.

The frequency dependence of the χ' peak temperature is fit to an Arrhenius

law, equation (1.7) in figure 6.10. The error bars are based on the temperature steps and the amount of noise in the signal. The parameters for the fit are E_a/k_B=133±4 K and f_0=1.46±0.06×10^{15} Hz, both extremely large values, consistent with the behaviour of a glassy phase. Although the fit is not as good, more physically reasonable values are obtained by using a Vogel-Fulcher law, equation (1.8), as in figure 6.11. With the extra parameter and with few data points, there is a large uncertainty in the parameter values. The values for the curve shown are f_0=9±3 × 10^{13} Hz, E_a/K_B=95±1 K and T_0=1 K. By increasing T_0, both f_0 and E_a/k_B decrease further to values closer to experimental conditions, but the fit to the low frequency data points gets worse. The poor fit to low-frequency data is common in spin glasses. Higher frequency experiments are needed to show how well the Vogel-Fulcher law fits. Also, the frequency dependence is smaller than would be expected for a superparamagnetic phase[6] and no frequency dependence would be seen here if this transition was to an antiferromagnetic state. This gives conclusive evidence that the low temperature state in the $FeBr_2$-GIC has a glassy nature.

The magnetic phases of the stage-2 $FeBr_2$-GIC are summarized as follows: At high temperatures, the material is paramagnetic, as evidenced by the high temperature susceptibility fit to the modified Curie-Weiss law. At 14.5 K, as seen from the susceptibility measurements, there is an increase in ordering. The transition is seen as an increase in χ_{dc} when the temperature is decreased through 14.5 K and a small peak in χ_{ac}. This indicates the presence of ferromagnetic ordering. The lack of a

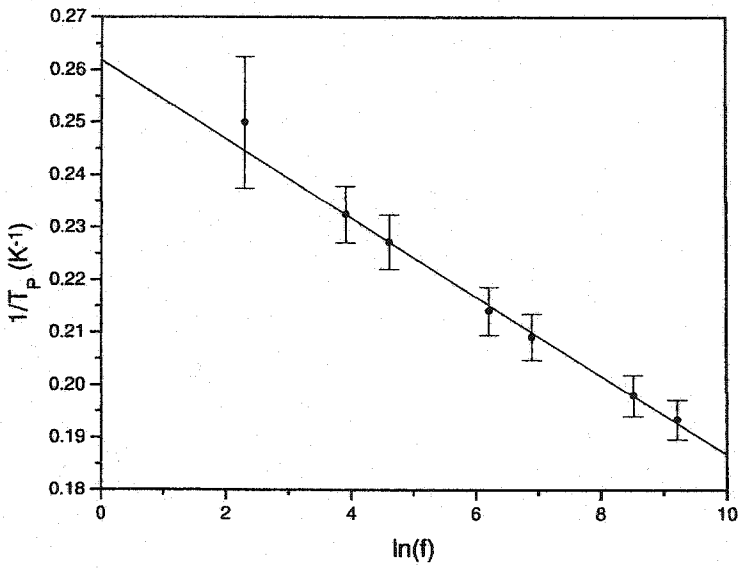

Figure 6.10: Frequency dependence of peak temperature fit to an Arrhenius law.

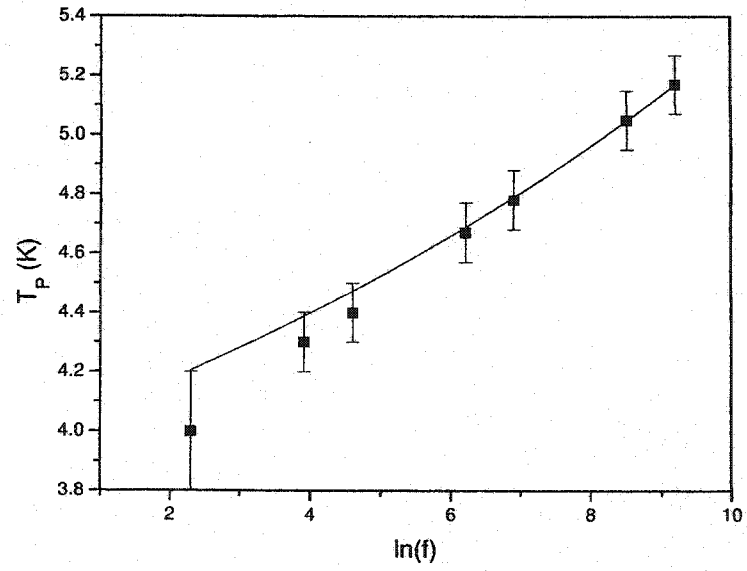

Figure 6.11: Frequency dependence of peak temperature fit to the Vogel-Fulcher law.

peak in the specific heat indicates that the ordering is short-ranged. At 8.5 K, there is further ordering, indicated by peaks in both χ_{dc} and χ_{ac} as well as a sharp peak in the specific heat. The small amount of entropy change associated with the peak in the specific heat indicates that the ordering within domains is not complete. Finally, at 3 K, the material enters a cluster-glass phase. The frequency dependence of the peak in χ', the broad peak in the specific heat and the history dependence of χ_{dc} all point to the glassy nature of this phase.

6.4 $NiBr_2$

Similar analysis to that shown for the other compounds was performed on the nickel compounds. The fits to the high temperature susceptibility of stage-2 $NiBr_2$-GIC are shown in figure 6.12. Once again, the non-linearity of the data indicates that the fitting requires the van Vleck term. With this term, the fit yields C=7.7±0.2 × 10^{-7} K·m^3/kg, θ_{CW}=29±2 K and χ_0= 4.61±0.08 × 10^{-9} m^3/kg. Using equation (1.2), and estimating p_{eff}=3.3 as in $NiCl_2$, a value of N=1.4±0.1 × 10^{17} is obtained from C. The positive value of θ_{CW} once again indicates that the ferromagnetic in-plane interactions are dominant.

By extrapolating the high-field region of the magnetization curve back to H=0, the saturation magnetization of stage-2 $NiBr_2$-GIC is determined to be M_{sat} = 0.359±0.004 A·m^2/kg. The slope of the high-field region is 2.92±0.12 × 10^{-8} m^3/kg.

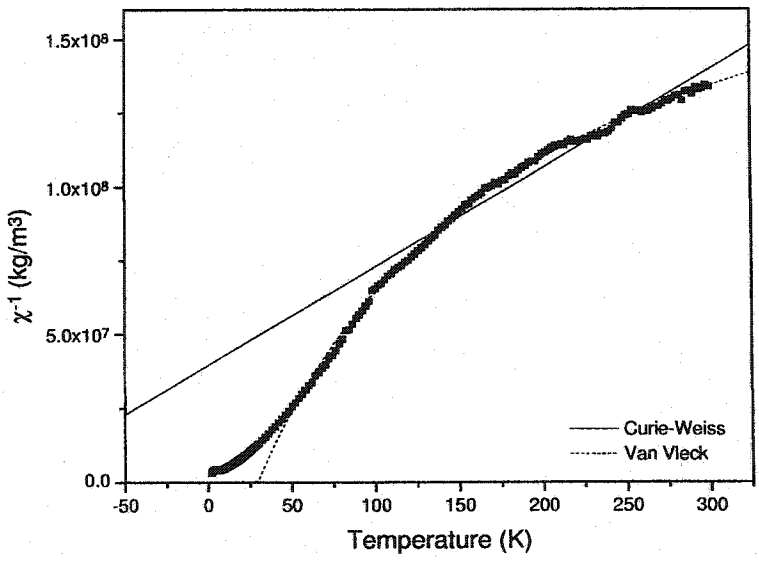

Figure 6.12: Fits to high temperature susceptibility for stage-2 $NiBr_2$-GIC. The solid line is a standard Curie-Weiss fit to the data and the dashed curve is modified with a temperature-independent term.

The saturation field is 1.5×10^6 A/m. Using equation (1.6), and assuming a moment of $\mu = 2\mu_B$, the inter-plane interaction strength is estimated to be $J'Z'/k_B$=-1.3 K or J'/k_B=-.06 K. This gives -$J'/J_1 \approx 3\times10^{-3}$.

The magnetization curve for stage-5 $NiBr_2$-GIC(figure 5.28) has a maximum of M_{sat}=0.117±0.001 A·m^2/kg at H_{sat}=1.5×10^6A/m. Above this field, the magnetization decreases and at high fields has a constant slope of -1.93±0.02 × 10^{-8} m^3/kg. This shows very strong diamagnetic character in the sample. One possible explanation for this is that the layers of graphite which do not come in contact with the intercalant maintain their diamagnetic character. The diamagnetic susceptibility of pure graphite is -6×10^{-6} emu/mol or -6.3×10^{-9} m^3/kg[2, 7], less than half the slope at high field. This means that there must be an additional mechanism for diamagnetism in the sample. As was the case in the $CoBr_2$ compounds, there seems to be no effect of staging on the saturation field and, hence, no effect on the inter-plane interaction. However, the uncertainty in the saturation field for these compounds is large because of the gradual change in curvature over a relatively large field range compared to the Co and Fe compounds.

The specific heat of the stage-5 $NiBr_2$-GIC shows no peaks and no change with applied field. This indicates that there is no long-range magnetic ordering in this material. The specific heat curve fits well to a quadratic curve, which is expected for a two-dimensional lattice such as graphite.

The results for $NiBr_2$-GIC are mixed. While the ac susceptibility has no discernible peaks for the stage-2 and stage-5 compounds, the dc susceptibility has a number of features. In the stage-2 compound, there is a peak at 7 K, below which the susceptibility goes through a minimum and then continues to increase down to 2 K. There is a small difference between the ZFC and FC susceptibilities here, indicating some relaxation and possibly two-dimensional ordering at the peak. Since the susceptibility drops after the peak, it is likely that this ordering would not be ferromagnetic but rather more like the incommensurate phase seen at low temperatures in the pristine compound. This, of course, has not been verified. The simulations based on Lines' work show that an antiferromagnetic transition, if any, could be at or below 4 K, consistent with this picture.

The stage-3 $NiBr_2$-GIC susceptibility is qualitatively similar to that of the stage-2 compound, with a peak followed by a lower-temperature minimum. This is to be expected since they would likely order in a similar fashion.

The dc susceptibility for the stage-5 sample appears to be consistent with superparamagnetism. The strong dependence on field cooling with the field cooled susceptibility continuing to increase well below the peak is a strong indicator. The lack of any feature in the specific heat, together with the quadratic nature of this curve, is also consistent with this. However, with this type of ordering, one would

expect to see a frequency-dependent peak in the ac susceptibility. Given the low magnetic signal from the sample, however, such a peak may have been below the resolution of the equipment. With the increased separation between magnetic layers in this compound, it is likely that the inter-plane interactions are reduced essentially to zero such that each intercalant domain in each layer acts independently of other domains. This is exactly what one expects in a superparamagnet.

6.5 Comparison of the Bromide-GICs

The ordering in the different compounds studied is quite varied. While none of the cobalt compounds ordered in the temperature range studied, there is evidence that there may be ordering at lower temperatures. The nickel compounds ordered to different degrees. The stage-5 compound has only superparamagnetic ordering while the stage-2 and 3 compounds appear to order at least partially in two dimensions, with a strong likelihood of three dimensional ordering below 2 K. Finally, the stage-2 iron compound undergoes a three-stage ordering process, with the lowest temperature phase being a cluster glass.

A summary of the fit parameters determined using the modified Curie-Weiss fit with the van Vleck term (equation 6.24) is given in table 6.1. For better comparison, the values for χ_0 have been converted to molar susceptibilities, using the number of moments determined from the fits. With the exception of the iron compounds, the

Table 6.1: Summary of fitting parameters for Bromide-GICs.

Intercalant	Stage	θ_{CW} (K)	C (K·m^3/kg)	χ_0 (m^3/mol)
$CoBr_2$	1($\perp$c)	-5.6	5.64×10^{-5}	7.8×10^{-8}
	1($\parallel$c)	4	4.53×10^{-5}	1.2×10^{-7}
	2	21	3.9×10^{-6}	3.7×10^{-7}
$FeBr_2$	2	-5.1	1.35×10^{-4}	2.1×10^{-8}
$NiBr_2$	2	29	7.7×10^{-7}	1.0×10^{-7}

values for χ_0 are the same order of magnitude and consistent with the values seen in the pristine materials and the chloride-GICs.

A comparison of the values obtained from fits to the susceptibility and saturation magnetization of the various compounds studied is given in table 6.2. There appears to be a large discrepancy between the fit parameters in some of the compounds, but there is a pattern to this discrepancy. For materials with stronger interactions, as estimated by the amount of ordering observed in the material, the difference between the results from the susceptibility data and the saturation data is large. For example, stage-2 $FeBr_2$-GIC, which shows the most ordering at low temperatures has a very large difference in the parameters, whereas stage-2 $CoBr_2$-GIC, which shows the least ordering of the materials, has virtually no difference. This indicates that the magnetization curves are strongly dependent upon the interactions among the magnetic ions, as shown by the Brillouin fits to the $CoBr_2$ compounds.

Table 6.2: Comparison of fitting parameters for Bromide-GICs obtained from the modified Curie-Weiss and saturation fits.

Material	Stage	χ_0 (m^3/kg)		Number of moments	
		Susceptibility	Saturation	Susceptibility	Saturation
$CoBr_2$	1	1.03×10^{-7}	4.38×10^{-7}	3.0×10^{18}	1.9×10^{18}
	2	3.4×10^{-8}	3.4×10^{-8}	2.1×10^{17}	2.3×10^{17}
$FeBr_2$	2	5.7×10^{-8}	2.41×10^{-6}	1.73×10^{19}	5.5×10^{18}
$NiBr_2$	2	4.61×10^{-9}	2.92×10^{-8}	1.35×10^{17}	9.6×10^{16}

6.6 Comparison to Metal Chloride-GICs

Both $NiCl_2$- and $CoCl_2$-GICs have a two step ordering process in which they order first two-dimensionally and then three-dimensionally, with the three-dimensional ordered phase having properties common to a cluster glass. This does not appear to be the case for the analogous compounds of the bromides, certainly down to 2 K. Although it is possible that ordering does occur at still lower temperatures, and indeed there is evidence to suggest this, the ordering temperatures will be much lower than those of the chloride GICs. This is not an unexpected result since the ordering temperatures of the pristine compounds are lower in the bromides than in the chlorides.

The splitting between ZFC and FC magnetization common to all three of the bromide GICs studied here, is similar to that in the chlorides[48, 55, 67], starting just above the upper transition temperature. This could indicate that there is a similar type of ordering at lower temperatures in the $CoBr_2$-GICs and that this is the ordering in the stages-2 and 3 $NiBr_2$-GIC.

In the chloride GICs, the specific heat has a peak at the upper transition temperature, T_{cu}, which is not seen in the specific heat measurement performed on the stage-5 nickel bromide compound. This is consistent with the ordering in the stage-5 compound being superparamagnetic, in which case there should be no peak in the specific heat. The specific heat results did show a T^2 dependence, characteristic of the two dimensional lattice and the chloride compounds[48, 52].

The $FeBr_2$-GIC has a three step transition, rather than the two step transition in the chloride GICs. The frequency dependence of the low temperature peak in χ' for $FeBr_2$-GIC is very similar to the response of the chloride-GICs[60, 67]. While the low temperature phase in $FeBr_2$-GIC is similar to that of the chloride-GICs, given the glassy behaviour, it is extremely unlikely that the intermediate phase of the bromide is the same as that of the chlorides. This is because $FeBr_2$ behaves very much like an Ising magnet rather than the X-Y behaviour of the nickel and cobalt compounds. Unfortunately, given the lack of work done with $FeCl_2$-GICs, no direct comparison can be made between the two iron compounds.

The van Vleck paramagnetic contribution to the susceptibility is a common feature to all of the bromide-GICs studied here. This was also found in the chloride-GICs through the finite slope of the magnetization curve at high fields. The values found in the present study (table 6.1) are consistent with those found in the chloride-

GICs[66, 81, 63] and the pristine compounds[4].

The ratio of the inter-plane to in-plane exchange constants, J'/J_1, is of the same order of magnitude in the bromide compounds as in the chloride compounds, with the bromides having slightly higher ratios. The bromides are also different in that this ratio remains constant with varying stage of material. In high stages, this is not surprising, but the lower stage materials should be more sensitive to changes in the inter-planar spacing.

Chapter 7
Conclusions

The dibromides of cobalt, iron and nickel have been intercalated directly into HOPG. Stages 1 and 2 of $CoBr_2$-GIC, stages 2,3 and 5 of $NiBr_2$-GIC and stage-2 $FeBr_2$-GIC were all obtained by using a solid diffusion technique. Stage-3 $CoBr_2$-GIC was also prepared based on single crystal natural graphite. The magnetic properties of these materials were studied by measuring the dc magnetization with the Quantum Design MPMS and ac susceptibility and specific heat with the Oxford Instruments MagLab EXA. The single crystal stage-3 $CoBr_2$-GIC was studied by neutron diffraction.

The three materials, although very similar in structure in pristine form, behave very differently once they are intercalated in graphite. In the case of the cobalt bromide intercalation compounds, there are no ordering transitions in any of the stages that were studied down to the lowest temperature available. There is some indication that the first stage compound may order at a slightly lower temperature, but this evidence is inconclusive.

The fact that there is no ordering in the cobalt compounds is supported by the simulations based on Lines' work[82, 83]. This clearly shows that, as the inter-plane interaction strength is decreased relative to the in-plane interactions, the Néel

temperature is reduced drastically. The ratio of these exchange parameters is of the order 10^{-3} - 10^{-4}. Lines' theory shows that the transition temperature in this case is expected to be a few degrees. By comparison with the pristine chlorides, the estimate provided by these simulations is an overestimate, showing that it is reasonable that there is no transition down to 2 K. This model does not take into account the effect of the graphite layers other than to reduce the inter-plane interaction strength.

There are three ordering transitions in the iron bromide compound. The first is from a paramagnetic state to short-range, two-dimensional ordering within individual domains at 14.5 K. The second is to longer range ordering within individual domains at 8.5 K, and the third is to a cluster glass phase at 3 K, where interactions among clusters are frustrated by the combination of ferromagnetic and antiferromagnetic interactions.

The $NiBr_2$-GICs all have a change in ordering based on magnetization measurements, but, from the specific heat, no long-range ordering occurs in the stage-5 compound. In the stage-2 compound, based on both χ_{dc} and magnetization measurements, ordering takes place at 6 K. This is most likely a two-dimensional ordering within individual intercalant domains. The stage-3 data show similar features to the stage-2 compound, indicating similar ordering at 7 K. The ordering in the stage-5 compound at 5 K appears to be superparamagnetic. Simulations also showed that ordering at these low temperatures is reasonable.

The formation of domains during intercalation, as shown by the SEM picture(figure 3.6), is critical to the magnetic properties of these compounds. Without interactions between these domains, there could be no cluster glass phase in the iron bromide compound. This domain structure was also the cause for remanant magnetization observed previously in the chloride-GICs, and it is reasonable to conclude that it is also the cause of the remanants in our data.

There are several experiments that could be performed in order to understand the ordering in these compounds better. For the cobalt bromide compounds, it would be useful to investigate the temperature regime below 2 K in order to see if, in fact, there are transitions at lower temperatures. Small angle neutron diffraction experiments would help to determine the presence and nature of any two-dimensional ordering appearing in the samples, especially in the region where there are remanant magnetizations.

For the iron bromide compounds, neutron scattering would be useful to confirm the nature of the transitions. Unfortunately, the 00ℓ scans usually used to detect antiferromagnetic ordering along the c-axis is not useful, since the magnetic moments are believed to align along the c-axis and an in-plane component is required for non-zero scattering along the c-direction. Once again, small angle diffraction would also help to confirm two-dimensional ordering.

Neutron scattering would also be useful in the case of the nickel bromide compounds to determine conclusively the nature of the transitions. In order to do any in-plane neutron scattering work, samples based on single crystal host material are required. It is, unfortunately, somewhat difficult to obtain single crystal samples of reasonable size for neutron scattering.

In the case of both the nickel and cobalt compounds, larger sample sizes would be very desirable so that magnetic signals could be strong enough too allow for proper Curie-Weiss fits with small applied fields. This would also eliminate the scatter seen in some of the ac susceptibility measurements, allowing for a verification that there are no transitions.

Samples of other stages of the various compounds, in particular the iron bromide GICs, would be useful. In the case of $FeBr_2$, this would serve as a comparison to see if there are any changes in the transition temperatures and whether the glassy phase occurs in all stages.

Electron microscopy could also prove to be a useful tool for characterizing these materials. This study features some SEM work, used to estimate the size of intercalant domains. A higher power, higher resolution machine such as the TEM would allow for more precise determinations of domain size. As well, x-ray emission could be used to determine the composition of the material with greater precision.

The temperature and field dependence of the resistance, both in-plane and c-axis, should also be investigated. Ordering transitions, both magnetic and structural, can be indicated by changes in resistance due to scattering from the magnetic intercalant and from phonons. The angular dependence of the magnetoresistance oscillations in the c-axis resistivity can show two-dimensional localization and weak localization effects could be seen from a logarithmic temperature dependence.

Bibliography

[1] Sōshin Chikazumi. *Physics of Magnetism.* John Wiley & Sons, Inc., New York, 1964.

[2] Allan H. Morrish. *The Physical Principles of Magnetism.* John Wiley & Sons ,Inc., New York, 1965.

[3] L.F. Bates. *Modern Magnetism.* Cambridge University Press, London, 4^{th} edition, 1961.

[4] I.S. Jacobs and P.E. Lawrence. Metamagnetism and exchange in ferrous bromide. *J. Appl. Phys.*, 35:996–997, 1964.

[5] K. Binder and A.P. Young. Spin glasses: Experimental facts, theoretical concepts and open questions. *Rev. Mod. Phys.*, 58:801–976, 1986.

[6] J.A. Mydosh. *Spin Glasses: An Experimental Introduction.* Taylor & Francis, Inc., Washington, DC, 1993.

[7] David R. Lide, editor. *Handbook of Chemistry and Physics.* CRC Press, Inc., Boca Raton, Fl., 73^{rd} edition, 1992-93.

[8] M.K. Wilkinson, J.W. Cable, E.O. Wollan, and W.C. Koehler. Neutron diffraction investigations of the magnetic ordering in $FeBr_2$, $CoBr_2$, $FeCl_2$, and $CoCl_2$. *Phys. Rev.*, 113:497–507, 1959.

[9] Hideki Yoshizawa, Koji Ubukoshi, and Kinshiro Hirakawa. Neutron scattering investigation of the magnetic excitations in $CoBr_2$. *J. Phys. Soc. Japan*, 48:42–49, 1980.

[10] W.J. de Haas and B.H. Schultz. Magnetic properties of some salts of the iron group at low temperatures. *Physica*, 6:481–496, 1939.

[11] Henri Bizette, Claude Terrier, and Belling Tsaï. Susceptibilités magnétiques principales du bromure et de l'iodure cobalteux. *C. R. Acad. Sci., Paris*, 246:250–252, 1958.

[12] Henri Bizette, Claude Terrier, and Belling Tsaï. Susceptibilités magnétiques principales des chlorure, bromure et iodure cobalteux. *J. Physique*, 20:421–423, 1959.

[13] D.J. Lockwood, G. Mischler, I.W. Johnstone, and M.C. Schmidt. Raman scattering from electronic excitations and phonons in paramagnetic and antiferromagnetic $CoBr_2$. *J. Phys. C: Solid State Phys.*, 12:1955–1975, 1979.

[14] G. Mischler, M.C. Schmidt, D.J. Lockwood, and A. Zwick. Magnon Raman scattering in $CoBr_2$. *Solit State Commun.*, 27:1141–1146, 1978.

[15] M.C. Schmidt, C. Escribe-Filippini, and K.R.A. Ziebeck. Investigations of the magnetic and lattice vibrations in $CoBr_2$ using neutron scattering. *J. Physique*, 43:931–938, 1982.

[16] W. Selke and S. Dasgupta. Magnetization anomaly in ising metamagnets. *J. Magn. Magn. Mater.*, 147:L245–L249, 1995.

[17] W. Selke. Anomalies in ising metamagnets. *Z. Phys. B*, 101:145–150, 1996.

[18] H. Aruga Katori, K. Katsumata, and M. Katori. Specific-heat anomaly in the ising antiferromagnet $FeBr_2$ in external magnetic fields. *Phys. Rev. B*, 54:R9620–R9623, 1996.

[19] Henri Bizette, Claude Terrier, and Belling Tsaï. Susceptibilités magnétiques principales du bromure et de l'iodure ferreux. *C. R. Acad. Sci., Paris*, 245:507–509, 1957.

[20] R.M. Brade and B. Yates. The low temperature heat capacities of ferrous bromide and ferrous iodide. *J. Phys. C: Solid State Phys.*, 4:876–883, 1971.

[21] M.C. Lanusse, P. Carrara, A.R. Fert, G. Mischler, and J.P. Redoulès. Étude de la chaleur spécifique du chlorure et du bromure ferreux. *J. Physique*, 33:429–433, 1972.

[22] A.R. Fert, P. Carrara, M.C. Lanusse, G. Mischler, and J.P. Redoulès. Transition de phase métamagnétique du brumure ferreux. *J. Phys. Chem. Solids*, 34:223–230, 1973.

[23] K. Katsumata, H. Aruga Katori, S.M. Shapiro, and G. Shiraine. Neutron-scattering studies of a phase transition in the metamagnet $FeBr_2$ under external magnetic fields. *Phys. Rev. B*, 55:11466–11470, 1997.

[24] C. Vettier, H.L. Alberts, and D. Bloch. Tricritical lines in metamagnets. *Phys. Rev. Lett.*, 31:1414–1417, 1973.

[25] M.M.P. de Azevedo, Ch. Binek, J. Kushauer, W. Kleemann, and D. Bertrand. Transient spin structures at the antiferro-to-paramagnetic phase boundary of $FeBr_2$. *J. Magn. Magn. Mater.*, 140–144:1557–1558, 1995.

[26] O. Petracic, Ch. Binek, W. Kleeman, U. Neuhausen, and H. Lueken. Field-induced transverse spin ordering in $FeBr_2$. *Phys. Rev. B*, 57:R11051–R11053, 1998.

[27] L.P. Régnault, J. Rossat-Mignod, A. Adam, D. Billerey, and C. Terrier. Inelastic neutron scattering invesigation of the magnetic excitations in the helimagnetic state of $NiBr_2$. *J. Physique*, 43:1283–1290, 1982.

[28] Hideki Yoshiyama, Naoshi Suzuki, and Kazuko Motizuki. Helix-antiferro-fan transition in $NiBr_2$ under an in-plane magnetic field. *J. Phys. C: Solid State Phys.*, 17:713–725, 1984.

[29] Ichiro Tsubokawa. The magnetic properties of $NiBr_2$. *J. Phys. Soc. Japan*, 15:2109, 1960.

[30] Yasuo Morimoto and Muneyuki Date. Magnetic resonance in $NiBr_2$ near the critical field. *J. Phys. Soc. Japan*, 29:1090, 1970.

[31] P. Day, A. Dinsdale, E.R. Krausz, and D.J. Robbins. Optical and neutron diffraction study of the magnetic phase diagram of $NiBr_2$. *J. Phys. C: Solid State Phys.*, 9:2481–2490, 1976.

[32] A. Adam, D. Billerey, C. Terrier, R. Mainard, L.P. Régnault, J. Rossat-Mignod, and P. Mériel. Neutron diffraction study of the commensurate and incommensurate magnetic structures of $NiBr_2$. *Solid State Commun.*, 35:1–5, 1980.

[33] A. Adam, D. Billerey, C. Terrier, H. Bartholin, L.P. Regnault, and J. Rossat-Mignod. Hydrostatic pressure effect on the commensurate-incommensurate phase transition of $NiBr_2$. *Phys. Lett.*, 84A:24–27, 1981.

[34] M.A. White and L.A.K. Staveley. A thermodynamic study of the magnetic phase transitions of $NiBr_2$. *J. Phys. C: Solid State Phys.*, 15:L169–L173, 1982.

[35] Koichi Katsumata, Kiyohiro Sugiyama, and Muneyuki Date. Experimental observation of the antiferro-fan transition in $NiBr_2$. *J. Phys. Soc. Japan*, 52:3312–3314, 1983.

[36] C. Starr, F. Bitter, and A.R. Kaufmann. The magnetic properties of the iron group anhydrous chlorides at low temperatures i. experimental. *Phys. Rev.*, 58:977–983, 1940.

[37] D. Moses, J.E. Kardontchik, R. Brener, and H. Shechter. Magnetic phase diagram of antiferromagnetic $CoCl_2$. *J. Phys. C: Solid St. Phys.*, 13:3903–3907, 1980.

[38] I.S. Jacobs and P.E. Lawrence. Metamagnetic phase transitions and hysteresis in $fecl_2$. *Phys. Rev.*, 164:866–878, 1967.

[39] Ch. Binek and W. Kleeman. Domainlike antiferromagnetic correlations of paramagnetic $FeCl_2$: A field-induced griffiths phase? *Phys. Rev. Lett.*, 72:1287–1290, 1994.

[40] R.H. Busey and W.F. Giauque. The heat capacity of anhydrous $NiCl_2$ from 15 to 300°k. the antiferromagnetic anomaly near 52°k. entropy and free energy. *J. Am. Chem. Soc.*, 74:4443–4446, 1952.

[41] Dominique Billerey, Claude Terrier, Robert Mainard, and Pierre Meriel. Structure magnétique de $NiCl_2$ à 4,2 k par diffraction de neutrons. *C. R. Acad. Sci. Paris*, B284:495–498, 1977.

[42] Charles Kittel. *Introduction to Solid State Physics.* John Wiley & Sons, Inc., New York, 6^{th} edition, 1986.

[43] M.S. Dresselhaus and G. Dresselhaus. Intercalation compounds of graphite. *Advances in Physics*, 30:139–326, 1981.

[44] Nicole Daumas and Albert Hérold. Sur les relations entre la notion de stade et les mécanismes réactionnels dans les composés d'insertion du graphite. *C. R. Acad. Sci. Paris*, C268:373–375, 1969.

[45] S. Flandrois, J.M. Masson, J.C. Rouillon, J. Gaultier, and C. Hauw. Intercalation compounds of graphite with nickel chloride: Synthesis, structure and mechanism of intercalation. *Synthetic Metals*, 3:1–13, 1981.

[46] S. Flandrois, A.W. Hewat, C. Hauw, and R.H. Bragg. Neutron diffraction and small-angle scattering studies of graphite-nickel chloride intercalation compounds. *Synthetic Metals*, 7:305–312, 1983.

[47] D.M. Hwang, R. Levi-Setti, G. Crow, Y.L. Wang, N.W. Parker, R. Mittlemen, X.W. Qian, and S.A. Solin. Application of microscopic probes to the study of graphite intercalation compounds. *Synthetic Metals*, 12:73–78, 1985.

[48] M. Matsuura, Y. Murakami, K. Takeda, H. Ikeda, and M. Suzuki. Crystallographic, thermal and magnetic properties of $cocl_2$-graphite intercalation compound - a quasi-two-dimensional system of finite size clusters. *Synthetic Metals*, 12:427–432, 1985.

[49] D.G. Wiesler, M. Suzuki, and H. Zabel. Ordering in quasi-two-dimensional planar ferromagnets: A neutron scattering study of graphite intercalation compounds. *Phys. Rev. B*, 36:7051–7062, 1987.

[50] G.K. Wertheim. Island formation in metal halide intercalation compounds. *Solid State Commun.*, 38:633–635, 1981.

[51] Yu. S. Karimov. Magnetically ordered state of two-dimensional ferromagnets with anisotropy of the "easy-plane" type. *Sov. Phys.-JETP*, 39:547–550, 1974.

[52] Yu. S. Karimov. Phase transitions of a layered ferromagnet with easy plane anisotropy. *Sov. Phys.-JETP*, 41:772–776, 1976.

[53] M. Elahy, C. Nicolini, G. Dresselhaus, and G.O. Zimmerman. Magnetic phases in transition metal chloride intercalation compounds of graphite. *Solid State Commun.*, 41:289–292, 1982.

[54] M. Elahy, M. Shayegan, K.Y. Szeto, and G. Dresselhaus. Magnetic properties of $CoCl_2$-intercalated graphite. *Synthetic Metals*, 8:35–42, 1983.

[55] Masatsugu Suzuki, Hironobu Ikeda, and Yasuo Endoh. Magnetic neutron scattering from second-stage $CoCl_2$-graphite intercalation compound. *Synthetic Metals*, 8:43–51, 1983.

[56] M. Elahy and G. Dresselhaus. $CoCl_2$-intercalated graphite: A quasi-two-dimensional magnetic system. *Phys. Rev. B*, 30:7225–7235, 1984.

[57] J.M. Kosterlitz and D.J. Thouless. Ordering, metastability and phase transitions in two-dimensional systems. *J. Phys. C: Solid State Phys.*, 6:1181–1203, 1973.

[58] Jorge V. José, Leo P. Kadanoff, Scott Kirkpatrick, and David R. Nelson. Renormalization, vortices and symmetry-breaking perturbations in the two-dimensional planar model. *Phys. Rev. B*, 16:1217–1241, 1977.

[59] J.T. Nicholls and G. Dresselhaus. Low-field magnetic properties of $CoCl_2$-graphite intercalation compounds. *J. Phys.:Condens. Matter*, 2:8391–8404, 1990.

[60] Masatsugu Suzuki and Itsuko S. Suzuki. Dynamic spin fluctuations in stage-2 $CoCl_2$ graphite intercalation compound. *Phys. Rev. B*, 58:840–846, 1998.

[61] Masatsugu Suzuki and Hironobu Ikeda. Magnetic phase transition of second-stage $NiCl_2$-graphite intercalation compound in an external magnetic field. *J. Phys. C: Solid State Phys.*, 14:L923–L928, 1981.

[62] Yu. S. Karimov. Investigation of the disordered state of two-dimensional ferromagnetic substances. *Sov. Phys.-JETP*, 38:129–133, 1974.

[63] S. Flandrois, J. Amiell, B. Agricole, E. Stumpp, C. Ehrhardt, and P. Schubert. Magnetic properties of first-stage nickel chloride graphite intercalation compounds. *Synthetic Metals*, 34:531–536, 1989.

[64] J.T. Nicholls and G. Dresselhaus. Magnetic properties of stage-1 $NiCl_2$-GICs. *Synthetic Metals*, 34:519–524, 1989.

[65] J.T. Nicholls, J.S. Speck, and G. Dresselhaus. Magnetic and structural properties of stage-1 $NiCl_2$-graphite intercalation compounds. *Phys. Rev. B*, 39:10047–10055, 1989.

[66] M. El Hafidi, G. Chouteau, and R. Yazami. Magnetic behaviour of a stage-1 $NiCl_2$ graphite intercalation compound. *Synthetic Metals*, 34:525–530, 1989.

[67] Itsuko S. Suzuki and Masatsugu Suzuki. Dynamic spin fluctuations in stage-2 $NiCl_2$ graphite intercalation compound. *J. Phys.: Condens. Matter*, 10:5399–5419, 1998.

[68] Kentaro Ohhashi and Ikuji Tsujikawa. Magnetic properties of $FeCl_2$-graphite compounds. mössbauer effect and magnetic susceptibility studies. *J. Phys. Soc. Japan*, 37:63–70, 1974.

[69] Z.D. Wang, M. Inagaki, and M. Takano. Moessbauer study of iron chloride-graphite intercalation compounds synthesized in molten salt. *Carbon*, 29:423–427, 1991.

[70] Masatsugu Suzuki and Itsuko S. Suzuki. Spin-glass phases in stage-2 $FeCl_3$ graphite intercalation compound. *Phys. Rev. B*, 58:371–384, 1998.

[71] Yu. S. Karimov, A.V. Zvarykina, and Yu. N. Novikov. Two-dimensional ferromagnetism in layered compounds of graphite with iron chlorides. *Sov. Phys.–Solid State*, 13:2388–2391, 1972.

[72] Corinne Balestri, René Vangelisti, Jean Melin, and Albert Herold. Étude exploratoire concernant l'insertion des bromures et des iodures métalliques dans le graphite. *C. R. Acad. Sci. Paris*, 279:279–280, 1974.

[73] H. Stahl. Zur kenntnis des eisen-brom-graphit-systems. *Z. Annorg. Allg. Chem.*, 428:269–276, 1977.

[74] E. Stumpp. The intercalation of metal chlorides and bromides into graphite. *Materials Science and Engineering*, 31:53–59, 1977.

[75] E. Stumpp, P. Schubert, and C. Ehrhardt. Preparation of metal halide graphite intercalation compounds by intercalate exchange. *Synthetic Metals*, 34:73–78, 1989.

[76] Volker Kaiser, Eberhard Stumpp, and Beate Tanneberg. Structural studies on metal bromide graphite intercalation compounds. *Mol. Cryst. Liq. Cryst.*, 244:293–298, 1994.

[77] F. Baron, Flandrois S., C. Hauw, and J. Gaultier. Charge transfer and islands in metal halides-graphite intercalation compounds: New evidence from x-ray diffraction of intercalated $MnCl_2$. *Solid State Commun.*, 42:759–762, 1982.

[78] Quantum Design, Inc., San Diego, CA. *Magnetic Properties Measurement System Hardware Manual.*

[79] Oxford Instruments, Abingdon, England. *MagLab User Guide.*

[80] J.A. Osborn. Demagnetizing factors of the general ellipsoid. *Phys. Rev.*, 67:351–357, 1945.

[81] I. Oguro, M. Suzuki, and H. Yasuoka. The magnetization of some transition metal graphite intercalation compounds. *Synthetic Metals*, 12:449–453, 1985.

[82] M.E. Lines. Antiferromagnetism in a layer structure by Green function techniques. *Phys. Rev.*, 131:540–545, 1963.

[83] M.E. Lines. Magnetic properties of $CoCl_2$ and $NiCl_2$. *Phys. Rev.*, 131:546–555, 1963.

[84] B.R. Heap. Application of the Bethe-Peierls method to a metamagnetic, $FeCl_2$. *Proc. Phys. Soc.*, 80:248–261, 1962.